The Behaviour and Charging Dynamics of Concentrated Electrolytes in Confinement under Potential Control

Astrid Southam



A thesis presented for the degree of
Doctor of Philosophy

Exeter College
Physical and Theoretical Chemistry Laboratory
University of Oxford
United Kingdom
30/07/2022

Abstract

The current understanding of intermolecular and interfacial forces in concentrated electrolytes is limited. Their importance to fields such as medicine, biology, ecology and the energy industry means that the pursuit of better knowledge has a wide-ranging impact on other areas of science and technology. In particular, the ubiquitous nature of batteries and energy-storing devices makes the behaviour of concentrated electrolytes near charged surfaces of special interest.

This thesis presents two novel surface force balance (SFB) methods to measure surface forces across electrolytes confined between charged surfaces, where one or both of the surfaces are under electrochemical control. The first method combines a muscovite mica surface and an ultra-smooth gold surface (gold/mica SFB), and the second uses two ultra-smooth gold surfaces. A large part of this work is concerned with the use of gold to fulfil the triple role of confining surface, working electrode and interferometric mirror. Improvements to surface fabrication methods yielded unique high-resolution ($\sim$ 0.1 nm) force measurements in the gold/mica setups and electrochemical measurements where the gold surfaces were under potential control.

These setups were used to measure force profiles in an ionic liquid (IL), 1-butyl-1-methylpyrrolidinium bis(trifluoromethanesulfonyl)imide (C_4C_1pyrr TFSI), and in a dilute electrolyte, potassium chloride in water (KCl (aq)) at 1.5 mM and 0.6 mM concentrations. In the gold/mica setup, unprecedented resolution was achieved, as evidenced by the presence of molecular layering in the force profiles.

Force measurements reported in this work show that underscreening, a long-range electrostatic force that has been observed in concentrated electrolytes, is independent of surface potential. It was also observed that the magnitude of the force does not scale with that of the applied potential. Potential step methods were used to show that the current decay in IL has three characteristic timescales corresponding to three different charge transport modes.

Declaration

This thesis is submitted for the degree of Doctor of Philosophy in Physical and Theoretical Chemistry at the University of Oxford. No part of this thesis has been accepted or is currently being submitted for any degree, diploma, certificate or other qualification in this University or elsewhere. This thesis is my own work, except where indicated.

Acknowledgements

First and foremost, I would like to thank my supervisor Prof. Susan Perkin for her unwavering support, patience and guidance throughout my time under her wing, despite some challenging hurdles. Her understanding and advice have been instrumental to my development as a scientist, and have helped me overcome my doubts at every step.

Secondly, I owe Dr. Marco Balabajew, Dr. Christian van Engers and Dr. James Hallett endless thanks for their friendship and mentorship. Marco taught me almost everything and guided my first steps in the lab, and Christian entrusted me with pursuing his vision for the triple-gold mirror SFB. James single-handedly salvaged the course of my research – without him, this thesis would look very different. I could never thank you enough James.

Of course, I cannot omit the Perkin group members, who helped and supported me, made me laugh and put up with me in general – in particular: Carla, Hannah, Tim and Catherine. Special thanks to Catherine for taking the time to read my thesis and impart her knowledge on top of all her other duties and research. There were many others who came and went over the years; they all contributed in their own ways, and I am grateful for all of them.

I have often said that without the workshops and the building management, we would be nothing, and I owe many thanks to the many people who helped fix various problems with their incredible skill and endless good humour.

I am especially grateful to Paul Mitchell for his assistance and kindness, Rob Jacobs for base-coating my double-gold lenses and everyone in the electrical and mechanical workshops for their numerous and inestimable contributions to making everything work.

I also received incredible support outside of the PTCL. For supporting me every step of the way through the highs and lows, and for proof-reading my thesis, all credit goes to Ivor – an exceptional, selfless friend for life, I look forward to many more outdoor adventures and teas. For the long talks, walks, climbs and unfaltering support and love, I am forever grateful for and indebted to Emma, Kate and Alkis. Leïla, Victor, merci de m'avoir soutenu tout le long, surtout pendant 2019.

Particularly, I want to thank my parents, Anne, Michael and Didier, for always believing in me and pushing me to challenge myself. Sans votre soutien et vos conseils, je n'y serais jamais parvenu. Eric, merci pour ton humour et tes choix de musique qui m'ont accompagné tout le long. Zoé, my partner in crime, my cheerleader, my sister and sister-at-arms, I would be nowhere without you – thank you so much.

Publications

The following publications and manuscripts relate to the work discussed in this thesis.

Van Engers, C. D., Balabajew, M., Southam, A., & Perkin, S. (2018). “A 3-mirror surface force balance for the investigation of fluids confined to nanoscale films between two ultra-smooth polarizable electrodes”. Review of Scientific Instruments, 89(12), 123901. https://doi.org/10.1063/1.5045485

Contents

1 Introduction **12**

1.1 Background 12

2 Theory **18**

2.1 Introduction 18

2.2 The Capacitor Model 20

2.3 Interaction Forces Between Surfaces: Constant Potential, Constant Charge and Charge Regulation 21

2.3.1 Constant Charge and Constant Potential 21

2.3.2 Charge regulation in the Electrical Double Layer 23

2.4 Mean-field Theory and the Poisson-Boltzmann Equation 25

2.5 Debye-Hückel Theory 27

2.6 The Electric Double-Layer and Gouy-Chapman Theory 28

2.7 Van der Waals Forces 30

2.8 DLVO Theory 31

2.9 Electrostatics at High Ion Concentrations 33

2.10 Structural Forces 37

3 Experimental Techniques : The Surface Force Balance 41

3.1 Introduction 41

3.2 The Classic Surface Force Balance 42

3.2.1 Interferometry: FECO in a Symmetric 3-Layer Interferometer 45

3.2.2 The Geometry of Confined Spaces in SFB 49

3.2.3 A Classic SFB Experiment 50

3.2.4 Measuring Forces 51

3.3 The Asymmetric Gold/Mica Setup 55

3.3.1 Introduction 55

3.3.2 Gold/Mica SFB: Experimental Setup 57

3.3.3 Making the Lenses 63

3.3.4 The Classic Three-Electrode Cell 67

3.3.5 Experimental Setup 71

3.3.6 Summary: Modifications to the Pre-existing Asymmetric Gold-Mica SFB 72

3.4 The Triple Gold Mirror Surface Force Balance 74

3.4.1 Introduction 74

3.4.2 The Triple-Gold Mirror Setup 76

3.4.3 Fabrication of the Lenses 80
3.5 The Three-Electrode SFB Cell 84
3.6 Conclusion 85

4 Results from the Gold/Mica SFB Setup: Underscreening 86

4.1 Introduction 86
4.2 Materials and Methods 87
4.3 Results and Discussion 88
4.3.1 Force Measurements in Ionic Liquid 88
4.3.2 Force Measurements in a Dilute Electrolyte 99
4.3.3 Layering of KCl Ions and Water 108
4.4 Conclusion 109

5 Results from the Gold/Mica SFB Setup: Charging Dynamics 111

5.1 Introduction 111
5.2 Theory 114
5.3 Material and Methods 117
5.4 Results and Discussion 118
5.4.1 Ionic liquid 118
5.4.2 Dilute Electrolyte 131
5.5 Conclusion 139

6 Results from the Au3 SFB Setup: Underscreening **141**

6.1 Au3 SFB: Experimental Results and Discussion 141

6.1.1 Materials and Methods 142

6.1.2 Underscreening 142

6.1.3 Comparing Results From Three SFB Setups 147

6.2 Conclusion 149

7 Conclusion **153**

A Appendix A **158**

A.1 Chapter 6: The Triple Gold Mirror Surface Force Balance 158

A.1.1 Contact-Free Calibration - The Multi-Matrix Method 158

A.1.2 Analysis 160

A.2 Chapter 4: results from the Gold/Mica SFB Setup: Underscreening 162

Chapter 1

Introduction

1.1 Background

The interactions of substances at the interface are essential to countless biological, chemical and physical processes. This makes the exploration and understanding of the forces that govern these interactions an indispensable endeavour, as they affect humans on many levels, from metabolism to industry [1–4]. Understanding the fundamental forces and dynamics at the interface has tremendous value, be it for protective coatings [5], lubricating gels [6, 7] or energy devices [3, 4, 8].

One field of particular importance is that of electrolytes. Energy storage and battery technology rely heavily on the use of electrolytes and excellent understanding of the forces and properties that govern their behaviours [2, 3, 9].

Despite the omnipresence of electrolytes, there is much left to elucidate in our understanding of them. Whilst dilute electrolytes have been relatively well characterised [10–12], the properties of concentrated electrolytes, at the interface, in the bulk and in confined spaces, depart from those predicted by the mean field theory used to describe their dilute counterparts, and remain poorly

understood [13]. Investigating this has been the focus of substantial work in experimental [1, 9, 10, 14], theoretical [15, 16] and computational [17–21] work in recent years, leading to the emergence of new theories and novel interpretations of the forces in concentrated electrolytes [21–24].

In surface force and intermolecular force studies, ionic liquids (ILs) provide a case study where the liquid is composed exclusively of ions, in the absence of solvent. This is the most extreme example of a concentrated electrolyte and thus is very useful for investigating the behaviours of such liquids [1, 25–27]. Ionic liquids are commonly defined as room-temperature molten salts, as they are usually composed exclusively of ions which remain in the liquid state due to a combination of steric effects and charge-delocalisation [4, 6]. As such, they are the most concentrated electrolytes available, as they do not contain any solvent. Due to the weak interactions between the anions and cations, the ionic liquid remains extremely stable [28] while retaining excellent conductivity [29–32]. Ionic liquids can be composed of any combination of anion and cation that fits the steric and charge-delocatisation prerequisites, which leads to a huge variety of tunable ionic liquids [4, 6, 33]. Generally the ions are large organic molecules, but examples of ionic liquids that contain smaller molecules or atomic ions also exist. As a rule, ionic liquids are thermally and chemically stable while being highly conductive, have a low melting point and extremely low volatility, and are soluble with numerous compounds depending on whether they are protic, aprotic or zwitterionic [4, 33]. Their thermal, chemical and electrochemical stability, among other tunable physical and chemical properties, make them extremely attractive for the development and study of energy storage [4, 8, 34], lubrication [6, 35, 36] and green chemistry [37, 38], to name a few.

There are many techniques available to study intermolecular and surface forces. Since the late sixties and seventies, the development and improvement of spectroscopic and probing techniques has seen a surge that has resulted in

more and more precise technologies and better understanding of surfaces and interfaces.

One such advance is the surface force balance (SFB), also known as surface force apparatus (SFA). The SFB was first designed in 1968 by Tabor and Winterton, and it was used to directly measure van der Waals forces between two surfaces in close proximity across air for the first time [39]. From there, improvements and modifications were made to the SFB to broaden its applications and functionalities beyond simple van der Waals forces in air. Israelachvili measured the thickness and refractive index of thin films in the seventies and adapted the SFB to directly investigate forces in liquids [40, 41]. This opened up the use of SFB to a much greater field, and further advances have allowed for the study of a whole wealth of liquids, including dilute and concentrated electrolytes [9, 42]. In more recent decades, the focus of intermolecular and surface force studies has turned towards electrochemistry, bilayers and biological systems, creating a need for modifying the SFB to be able to measure new types of systems and expand the scope of the SFB. Today, the SFB is not only used to measure normal forces [21], but also lateral [9, 43], structural [26, 44] and frictional [43] forces, and several electrochemical setups have been proposed [45–54], which opens the SFB up to electrochemical measurements.

Since the sixties, these SFB measurements have almost all been done using muscovite mica as the solid at the interface. Muscovite mica is a hydrated sheet silicate mineral of aluminium and potassium which has perfect basal cleavage that can yield extremely thin, flexible sheet layers [55]. Due to the atomically smooth surface (0.034 nm RMS roughness) of these layers, which can be cleaved into single crystal facets a few micrometers thick and several cm^2 in area, mica is an ideal surface for SFB [10, 39, 40]. The facets can be coated in metal to create a mirror, and the smoothness of the mica affords excellent interferometric resolution. In SFB, back-silvered mica pieces are glued to two lenses, which are

stacked so they face each other, and light is shined though. The constructive interference exiting the stack is recorded and gives information about the environment between the two lenses.

Although mica presents many advantages such as resolution and smoothness, it is also an insulator, which prevents the control of electrical potential on the surface. Some studies have been done where the mica is doped with a differently-charged substance [56], or where a current is passed across the fluid [57], but it is not possible to reliably measure the current in a dielectric. As a consequence, in recent years efforts have been made to develop a system in which different conducting solids can be used at the surface [45–49, 58] while retaining sufficient optical resolution and smoothness, as required for probing interactions at the molecular level. Controlling potential is important for the investigation of the behaviour of electrolytes at the solid/liquid interface where the surface's potential can change, especially considering the ever-growing use of energy storage devices, membranes, and electrolyte-dependant technologies in daily life and in industry [8, 59].

Several alternative SFB setups have been proposed to achieve potential control. In asymmetric setups, one mica-coated lens is paired with another coated in metal [52, 58]. One of the more popular approaches is to combine one mica lens with a gold one [58], as template-stripped gold can have RMS roughness of as little as 0.2 nm [60]. The results discussed in Ch. 4 and 5 were obtained from experiments in a modified asymmetric gold/mica SFB setup.

Symmetric setups (where both confining surfaces are the same substrate) using conductive materials have also been proposed, with gold remaining the preferred choice. However, other issues arise with such setups, especially in terms of limitations to the types of experiments that can be performed and difficulty analysing the results [47, 53, 61]. Typical problems include loss of resolution due to surface roughness, complex spectra due to additional reflections and

technical difficulties in setting up experiments. Levins and Vanderlick [62] proposed the first fully potential-controlled symmetric system with metal films, and the three-mirror interferometer proposed by van Engers *et al.* in 2018 [45], which was inspired by it, addressed some of the issues with its predecessor. As both surfaces are coated in gold, it features both symmetric polarizability and higher resolution than previous setups of the same nature. This setup was used for the experiments discussed in Ch. 6.

This thesis presents two novel electrochemical SFB setups using gold surfaces, one asymmetric (gold/mica SFB) and one symmetric (Au3 SFB) and the results obtained with these. This is the first time either technique has been set up and implemented in the Perkin group at the Physical and Theoretical Chemistry Laboratory in Oxford, and the latter is an entirely new SFB technique. The gold/mica SFB setup is significantly improved upon; the fabrication method described here produces lenses that offer excellent resolution, allowing structural forces to be measured at electrode surfaces for the first time, both in an ionic liquid and in a dilute electrolyte. The methodology reported in this work is proposed as a new protocol for high-resolution electrochemical gold/mica SFB setups. The symmetric Au3 SFB setup offers potential control of both surfaces and the multi-matrix method is used to obtain surface separation with contact-free calibration, a unique setup that demonstrates that two metal surfaces can be used without significant changes to the SFB.

This thesis also presents results obtained with these setups and seeks to address the influence of surface charge on long-range electrostatic forces observed in ionic liquids, their magnitude and the near-surface behaviour of ions. It seeks to understand the charging dynamics of an ionic liquid confined to a few nm, and compares these results to equivalent measurements in a dilute electrolyte. The force profiles and chronoamperometric data demonstrate the unprecedented high resolution of the gold/mica setup, showing evidence of molecular layering

in an ionic liquid and in dilute KCl (aq). The long-range electrostatic force seen in concentrated electrolytes (termed “underscreening” by Lee *et al.* [22]) in prior mica/mica SFB and AFM measurements was also observed in gold/mica and Au3 SFB, and it was found that varying surface potential does not affect the screening length. Additionally, the magnitude of this force was unaffected by changing surface potential, an unexpected result seen with both techniques. Potential-step methods were used to show that the double-layer formation in a pure ionic liquid has different timescales than in a dilute salt (KCl (aq)), arising from different charge-transport modes.

The principal focus of this work has been instrument-development and it provides protocols and proof-of-concept experiments which will facilitate future studies of electrolyte/electrode interfaces with molecular resolution. The results presented here illustrate the potential of these setups and show some unusual and interesting behaviours of a concentrated electrolyte at a surface under potential control.

Chapter 2

Theory

2.1 Introduction

The study of surface forces is an essential pursuit to understand what governs the behaviour of molecules and particles, particularly in electrolytes. For example, the interplay of hydration, electrostatics and hydrophobic forces govern protein and membrane interactions, and understanding these allows scientists to develop drug and vaccine delivery [63–66]. Similarly, understanding nanoparticle interactions makes it possible to study the toxicity of cosmetics and drugs with metals in nanoscale suspensions [67]. The development of technologies such as supercapacitors and batteries also heavily rely on understanding these forces [68–70].

Motivating and modifying theories from results and pushing pre-existing ones to their limits is fundamentally part of the exploration of surfaces and intermolecular forces, and it goes hand-in-hand with gaining better understanding of the properties of the liquids, solids and interfaces. Recent advances in direct measurement techniques also allow the study of interfaces under potential control [23, 50–54, 58, 71, 72], offering insight into a whole new aspect of surfaces

and interfaces and how they behave in electric fields.

Conductivity is proportional to the charge concentration and limited by viscosity. A very dilute electrolyte has few charge carriers relative to the number of solvent molecules it is dissolved in, which means that it has low viscosity, but also that it has few charge carriers, resulting in low conductivity. On the other extreme, a very concentrated electrolyte has many charge carriers, but high viscosity as the migration of a charge carrier is hindered by the presence of all the ions in close proximity, which means that conductivity will also be lowered. Conductivity is highest when the concentration of charge carriers is maximised and viscosity is minimised.

As a consequence, although dilute electrolytes are well understood, they are not the most suitable choice for electroactive materials. It stands to reason that concentrated electrolytes are the logical choice for electroactive materials and their study [4, 30, 73], and in fact naturally occurring electrolytes such as the ones found in human physiology or ocean water, typically have concentration at or over $\sim$ 0.1 M [74–76]. Unfortunately, from a theoretical point of view, concentrated electrolytes are much less well understood than the dilute kind: they are not well described by mean-field theory and the complex mix of contributing forces means that it has remained difficult to elucidate definitive theories to describe their intermolecular and interfacial behaviour [77].

In addition to the issue of dilute versus concentrated electrolytes, there is the added problem that mean-field theories describe the behaviour of the bulk (or continuum), and do not always apply to liquids confined to spaces at the nanometric scale. This results in observations of anomalous forces that cannot be explained by conventional bulk theory. To understand this on a more fundamental level, one must go back to the theories that underpin current knowledge about these subjects and see why they do not always fully explain the behaviour of concentrated electrolytes. Here some context is provided, outlining the theory

relevant to this work and underlining its limitations.

2.2 The Capacitor Model

We consider a charged plate immersed in an electrolyte, to ensure overall charge neutrality there must be countercharges nearby. The capacitor model describes two equally and oppositely charged planes parallel to each other. The electric fields within and outside of the capacitor is determined by adding the field $\pm\sigma/\varepsilon_0\varepsilon$ from each plate [42]. Within the capacitor plates, the two fields added together gives the overall field $E_{in} = -\sigma/\varepsilon_0\varepsilon$ and outside of the capacitor, one field subtracted from the other results in a net zero $E_out = 0$.

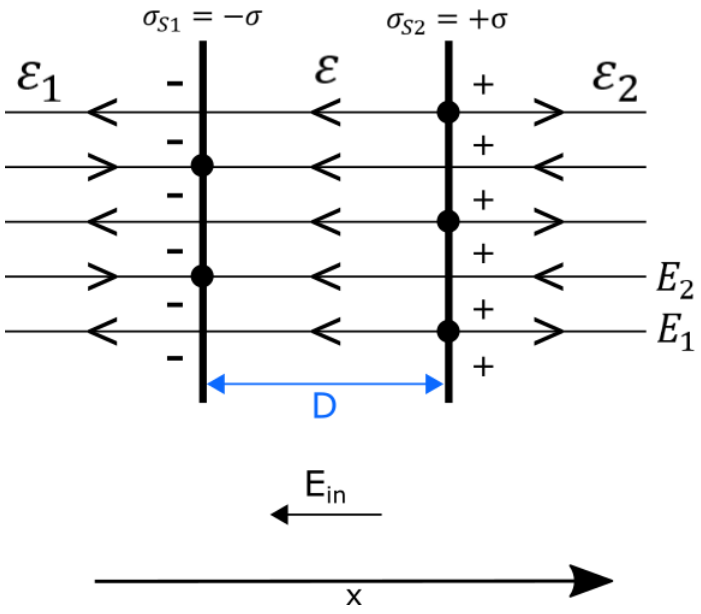


Figure 2.1: *Parallel plate capacitor, where each plate is equally and oppositely charged.The net interaction between the two is attractive, with the field E_{in} flowing from positive to negative. σ_{S1} is the charge of the first plate (here it is equal to $-\sigma$), σ_{S2} is the charge of the second plate (here it is equal to $+\sigma$), ε_1 is the permittivity of the first plate (outside of the capacitor), ε_2 is the permittivity of the second plate (outside of the capacitor),ε is the permittivity of the medium between the parallel plates (within the capacitor), D is the separation between the plates, E_in is the net electric field between the two plates.*

The pressure between the capacitor plates is calculated from the field of one surface acting on the charge of the second plate, where the field is $E_{S1} =$

$-\sigma/2\varepsilon_0\varepsilon$ and the charge is $\sigma_{S2} = +\sigma$. This gives us the force per unit area:

$$F = \sigma_{S2}E_{S1} = \sigma_{S1}E_{S2} = -\sigma^2/2\varepsilon_0\varepsilon \tag{2.1}$$

This equation indicates that the surfaces attract, and that field and pressure are independent of the separation of the plates D. The electric field energy E_∞ of an infinite parallel plate capacitor is $E_\infty = +\sigma^2 D/2\varepsilon_0\varepsilon$ per unit area.

2.3 Interaction Forces Between Surfaces: Constant Potential, Constant Charge and Charge Regulation

2.3.1 Constant Charge and Constant Potential

When discussing conductive and insulating surfaces and the forces between them, it is important to consider the concepts of constant charge and constant potential. There are several methods for modelling these interactions in dilute electrolytes, which we shall summarise here, and their relevance to the work in this thesis will be discussed.

Metallic surfaces where the electrochemical potential is controlled by a potentiostat (*e.g.* an electrode surface) can be considered to have constant potential. A metallic electrode will experience varying surface charge depending on the surrounding medium and any field from a nearby body.

In contrast, insulating (non-electrode) surfaces can in some cases be considered to have constant charge. For example, this might arise from the ionisation of a mineral surface in water (*e.g.* mica in dilute electrolyte).

The force of the interaction between surfaces can be interpreted in terms of their charge and/or potential, and much theoretical and experimental work has been dedicated to this over recent decades [58, 72, 78, 79]. For instance, McCormack, Carnie and Chan showed how the Poisson-Boltzmann equation can be solved using a variety of boundary conditions, including: constant potential on both surfaces (”PP”), constant charge on both surfaces (”CC”) and constant charge on one surface and constant potential on the other (”CP”). This approach was validated experimentally by other groups [58, 72]

McCormack *et al.* [78] presented a general method for qualitatively visualising the variation of force per unit area between parallel plates (using the Derjaguin approximation), as well as that of surface charge and potential with separation. It uses Poisson-Boltzmann theory for two dissimilar parallel plates interacting across a symmetric electrolyte and a graphical method to predict the features of the force per unit area with respect to the separation between the plates.

The surfaces can maintain constant charge, constant potential, or a mix of the two. In this thesis, we discuss two scenarios: one where one surface is at constant potential and the other at constant charge (gold/mica SFB), and one where both surfaces are identical and have constant identical potential (Au3 SFB). This gives rise to the following cases:

- The surfaces have the same sign, where the surface with higher potential has constant charge. This corresponds to the case where mica (constant charge) is negative, gold (constant potential) is equal or more negative.
- The surfaces have the same sign, where the surface with higher potential has constant potential. This corresponds to the case where mica (constant charge) is negative, gold (constant potential) is equal or less negative.
- The surfaces have opposite signs, where the surface with higher potential

has constant potential. This corresponds to the case where mica (constant charge) is negative, gold (constant potential) is positive.

- Both surfaces are at constant potential of the same sign. This corresponds Au3 SFB at positive and negative potentials.

Other cases occur in other systems, but here we detail those relevant to this thesis.

2.3.2 Charge regulation in the Electrical Double Layer

Further to the principles outlined in the prior section, it is important to consider charge regulation, which is another method of characterising charged surfaces interacting across a liquid. We consider diffuse layer that forms at the interface when a surface is immersed in liquid, in particular a dilute electrolyte; the diffuse layer has a characteristic monotonic decay of the counterions away from the surface. Some counterions may adsorb on the surface. The exact composition and charge density of this adsorbed layer are complex problems and difficult to elucidate [80], but it is known that the adsorbed layer affects the charge of the surface as well as the potential of the diffuse layer. When two surfaces with adsorbed ions and a diffuse layer interact, and the surface charge and diffuse layer potential are regulated on approach for a given solution, this is known as charge regulation. It is considered in the framework of DLVO theory, where interactions are dominated by van der Waals forces and EDL forces, which are described by Poisson-Boltzmann theory.

In the previous section, constant charge and constant potential cases were discussed, but in practice, these are not always applicable models to describe the interactions between surfaces with diffuse layers. It is well established that when diffuse layers interact, their profiles are modified by each other and the

surface charge and layer potential are regulated as the surfaces approach each other [79–84]. The equation for the total force between surfaces F_{DLVO} adapted from Carnie and Chan [80, 85] gives a simplified expression which allows for charge regulation at the boundaries for surfaces interacting across a dilute electrolyte where the potential of the diffuse layers is small:

$$\frac{F_{DLVO}}{R} = 2\pi E^{\|} \approx -\frac{A}{6D^2} + 4\pi\varepsilon_0\varepsilon\kappa_D\psi_{eff}^2\frac{e^{-\kappa_D D}}{1+(1-2p)e^{-\kappa_D D}} \tag{2.2}$$

Where R is the radius of curvature of the surfaces (in SFB, this is the radius of curvature of the crossed cylinders), $E^{\|}$ is the interaction free energy per unit area between the surfaces, A is the Hamaker constant, ε_0 is the permittivity of free space, ε is the relative permittivity, ψ_{eff} is the effective surface potential, κ_D^{-1} is the Debye-Hückel screening length and p is a dimensionless charge regulation parameter. p ranges from the constant potential boundary condition $p = 0$ and the constant charge boundary condition $p = 1$.

It should be noted that it has not yet been demonstrated how one surface at constant potential and another charge-regulating insulator surface interact, and many aspects of the constant charge/potential and charge regulation methods remain areas of active research.

Despite this clear analysis of the nature of forces in dilute electrolytes, the situation is expected to be very different for ionic liquids, where none of the basic assumptions of Poisson-Boltzmann theory apply. In particular, the ions in an IL fill the volume of the fluid, so the assumption of point-charges does not hold as Coulomb interactions cannot be treated as perturbations [22]. As a result, the constant charge/potential model and charge regulation model may not be used in ILs. Additionally, it is known that in the near-surface region, an IL can "overscreen" or "crowd" a surface charge [22, 86], resulting in the effective charge felt by the approaching surface being very different from what might be expected given the applied potential or the surface charge of the substrate. Difficulties

arising from this include the interpretation and measurement of surface charge, open circuit potential (OCP) and charge regulatory effects. For example, the classic Gouy-Chapman model for the potential of zero charge (PZC) cannot be applied in ILs due to the “camel” shape of the voltage dependence of the double layer capacitance, the nature of which is still under investigation [87].

2.4 Mean-field Theory and the Poisson-Boltzmann Equation

When discussing a dilute electrolyte in bulk liquid, certain assumptions are made to describe the interaction of the ions in solution: the solvent is treated as a continuum (a mean field), ions are considered as monovalent and taking up no volume and chemical potential is taken to be the same throughout. We consider a dilute electrolyte between two surfaces, where the electric field $E = 0$ at the midplane, and there is overall electroneutrality, *i.e.* there are the same number of positive and negative charges overall.

The Poisson equation describes the net excess charge density at a point x between the surfaces:

$$ze\rho = -\varepsilon_0\varepsilon(d^2\psi/dx^2) \tag{2.3}$$

Where z is the valency, e is the elemental charge, ρ is the number density of ions of valency z at any point between two surfaces, ε_0 is the permittivity of free space, ε is the dielectric constant, ψ is the electrostatic potential and $E = d^2\psi/dx^2$ is the rate of change of the electric field.

The Boltzmann distribution describes the distribution of ions at any point x, assuming that electrochemical potential is the same for every value of x (Nernst

equation):

$$\rho = \rho_0 e^{-ze\psi/k_B T} \tag{2.4}$$

Where ρ_0 is the number density of ions of valency z at the midplane (bulk), where $\psi_0 = 0$, k_B is the Boltzmann constant and T is temperature.

In practice, electrolytes are composed of counterions (opposite charge to the confining surface), co-ions (opposite charge to the counterions) and possibly a solvent (neutral). Poisson-Boltzmann can be extended to account for these different ions i of valences z_i and concentrations c_i, where we assume that the ion concentrations are independent. If we consider $x = 0$ at the surface, $x = \infty$ at large separations, where the liquid is in the bulk state, total number density $\sum_i \rho_{xi}$ and charge density at x as $\sum_i z_i e \rho_{xi}$, the Boltzmann distribution away from the surface can be rewritten as:

$$\rho = F \sum_i z_i c_{i0} e^{-z_i e\psi/k_B T} \tag{2.5}$$

Where F is the Faraday constant, c_0 is the bulk concentration.

By substituting Eq. 2.5 into Eq. 2.3, we obtain the Poisson-Boltzmann equation, which in a non-linear partial differential equation. It can be simplified by using the assumption that at low potentials ($<$ 25 mV), $e\psi/k_B T$ is very small, which means:

$$e^{-e\psi/kT} \approx 1 - e\psi/k_B T \tag{2.6}$$

This is the Debye-Hückel approximation, and it gives us the linear Poisson-Boltzmann equation. For a charged plane, this is:

$$\frac{d^2\psi}{dr^2} = \kappa^2 \psi \tag{2.7}$$

Where κ is the Debye screening length.

2.5 Debye-Hückel Theory

The structure and behaviour of dilute electrolytes near a charged surface are well understood, and can be characterised with Debye-Hückel theory, where an ion is at the centre of a decaying field and the field is spherical. It can also be used to describe the interaction between charged surfaces in an electrolyte. If we recall Eq. 2.7, and take $x = 0$ at the plane, the potential decay depends only on x, the distance away from the plane, which gives us the solution:

$$\psi = \psi_0 e^{-\kappa x} \tag{2.8}$$

The Debye screening length $\kappa^{-1} = \lambda_D$ is a decay length that decreases exponentially with surface separation:

$$\lambda_D = \sqrt{\frac{\varepsilon_0 \varepsilon_r k_B T}{4\pi q^2 c_{ion}}} \equiv \frac{1}{\sqrt{4\pi l_B c_{ion}}} \tag{2.9}$$

where ε_0 is the vacuum permittivity, ε_r is the dielectric constant, k_B is the Boltzmann constant, T is temperature, q^2 is the ion charge, c_{ion} is the ion concentration and l_B is the Bjerrum length. Bjerrum length is defined as the distance between two ions interacting in a medium with dielectric constant ε such that the interaction energy is equal to $k_B T$, the thermal energy unit:

$$l_B = \frac{q^2}{4\pi \varepsilon_r \varepsilon_0 k_B T} \tag{2.10}$$

However, the mean-field Debye-Hückel theory is only valid when ${l_B}^3 c_{ion} << 1$, which means that it is not valid when considering concentrated electrolytes, as it only applies to a system where ion-ion separation is much larger than l_B.

2.6 The Electric Double-Layer and Gouy-Chapman Theory

When a charged surface is immersed in a liquid containing ions, the liquid will respond so as to balance out the surface charge, and a layer of charges of opposite sign (counterions) will form near the surface, so that overall electroneutrality over a certain lengthscale is achieved. The term “double-layer” refers to the conceptual layer of charge on the surface plus the counterion layer in the liquid. If counterions are bound to the surface (even transiently), this is referred to as a Stern (or Helmholz) layer, where counterions are situated within a few Å of the surface. When the counterions are distributed in a more diffuse manner that extends further out from the surface, they form a non-bounded layer that maintains some motion, and this is referred to as a diffuse double-layer. With metals, the surface can be considered such that each counterion in the liquid has an opposite “image charge” on the surface, and the ensemble of image charges can be viewed as a single layer of ions with opposite charge to the layer of counterions maintaining electroneutrality.

Gouy-Chapman theory is a model for the interaction of charged particles in a dilute electrolyte at a metal solid surface, and uses the assumptions that the particles have no volume, do not interact with the surface and that the solvent is a continuum. The Stern layer is a modification to this theory, where a layer of counterions are bound to the oppositely charged surface; the limit of this bound layer is known as the outer Helmholtz plane (OHP), and Gouy-Chapman theory become valid from this point, as represented in Fig. 2.2. The electric potential at the surface decays linearly across the Stern layer, and from the OHP out into the liquid, the potential decays exponentially. Gouy-Chapman theory describes the

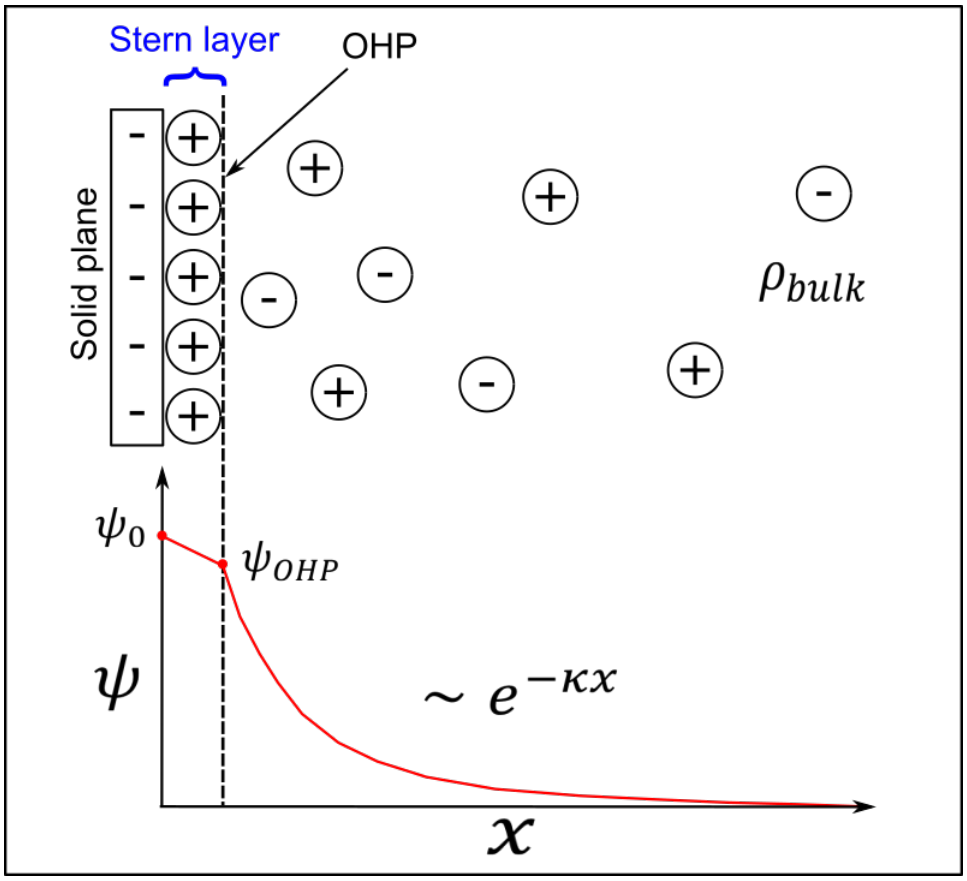


Figure 2.2: *Representation of the decay of the ekectric potential from the surface. The Stern layer is characterised as a layer of ions bound to the oppositely charged surface. The potential decays linearly between the surface and the outer Helmholtz plane (OHP), where mean-field theory becomes valid. The potential decays exponentially away from the OHP, which decays as* $\sim e^{-\kappa x}$*. Figure not to scale.*

potential gradient at any point x away from an isolated surface as follows:

$$\sum_i \rho_{xi} = \sum_i \rho_{\infty i} + \frac{\varepsilon_0 \varepsilon}{2k_B T} \left(\frac{d\psi}{dx}\right)_x^2 \tag{2.11}$$

For a 1:1 electrolyte, this becomes:

$$d\psi/dx = \sqrt{8k_B T \rho_{\infty i}/\varepsilon_0 \varepsilon} sinh(e\psi_x/2k_B T) \tag{2.12}$$

Giving us:

$$\psi_x = \frac{2k_B T}{e} log\left[\frac{1+\gamma e^{-\kappa x}}{1-\gamma e^{-\kappa x}}\right] \approx \frac{4k_B T}{e}\gamma e^{-\kappa x} \tag{2.13}$$

Where

$$\gamma = tanh(e\psi_0/4k_BT) \tag{2.14}$$

Therefore, at high potentials, $\gamma \to 1$, and for low potentials (<25 mV), the equation of ψ_x reduces to:

$$\psi_x = \psi_0 e^{-\kappa x} \tag{2.15}$$

Which is the Debye-Hückel equation.

2.7 Van der Waals Forces

The van der Waals force is composed of three forces acting between atoms and molecules, all of which vary with $1/r^6$, where r is the inter-particle distance. These forces are:

1. Orientation, or the Keesom interaction between permanent dipoles;
2. Induction, or the Debye interaction between dipole-induced dipole;
3. Dispersion, or London force between all atoms or molecules.

The latter force usually dominates the other two in its contribution to the total van der Waals force, except for cases involving small and highly polar molecules. In the context of intermolecular forces, van der Waals interaction is weak and short-ranged, and in solution it is further reduced. For two flat surfaces, the energy of the van der Waals interaction is expressed as:

$$W_{vdW} = -A_H/12\pi D^2 \tag{2.16}$$

and the force is expressed as:

$$F_{vdW} = -dW/dD = -A_H/6\pi D^3 \tag{2.17}$$

Where D is the separation between the surfaces and A_H is the Hamaker constant. The Hamaker constant, which is a coefficient that accounts for the van der Waals interaction between two bodies (ignoring the effect of the medium between them), is defined as:

$$A_H = \pi^2 C \rho_1 \rho_2 \tag{2.18}$$

Where C is the coefficient in the atom-atom pair potential, and ρ_1 and ρ_2 are the number of atoms per unit volume in the two bodies interacting. The magnitude of the Hamaker constant is influenced by the nature and properties of the substrates and reflects the strength of the van der Waals force between them.

In solution, the total van der Waals force between similar particles or molecules is always attractive. However, it is counterbalanced by several other repulsive forces, which includes electrostatic (long-range), structural and steric forces. The force between dissimilar particles can be attractive or repulsive.

2.8 DLVO Theory

DLVO theory was proposed in 1941 by Boris Derjaguin and Lev Landau, and Evert Verwey and Theodoor Overbeek arrived at the same theory independently; the initials of all four were used to name it. It describes qualitatively how particle dispersions aggregate in aqueous media.

DLVO theory predicts that the overall interaction between two particles or surfaces is a sum of two separate interactions, a van der Waals contribution and an electrostatic contribution. Fig. 2.3 shows the interplay of the contributing forces. The nonretarded van der Waals contribution is expressed in Eq. 2.16, and when the two bodies have the same charge, V_{vdW} is always negative (attractive force). The electrostatic component describes the interaction between the EDLs of each surface as an overall normal stress T_{xx}, and for a 1:1 electrolyte can be

broken down into a sum of osmotic stress and Maxwell stress [88]:

$$T_{xx} = 2\rho_0 k_B T \cosh(e\psi/k_B T) - \frac{\epsilon_r \epsilon_0}{2}(\frac{d\psi}{dx})^2 \tag{2.19}$$

Where ρ_0 is bulk concentration k_B is the Boltzmann constant, T is temperature, e is elementary charge, ψ is local potential, ϵ_r is the dielectric constant, ϵ_0 is the permittivity of vacuum and x is the distance variation between the surface, by which ψ varies.

To predict the forces between two charged surfaces across a liquid medium with DLVO theory it is necessary to use the potential distribution $\psi(x)$, so we go back to the Gouy-Chapman model and the Poisson-Boltzmann equation and this gives us:

$$\frac{d^2\psi}{dx^2} = \frac{2e\rho_0}{\varepsilon_r \varepsilon_0} \sinh(\frac{e\psi}{k_B T}) \tag{2.20}$$

The boundary conditions depend on what is being considered, but constant potential and constant charge density are usually used to give respectively a lower and an upper boundary for the force. Depending on the type of system being used experimentally, DLVO predictions may not be completely accurate, or may need to be complemented by other methods [88].

The van der Waals force has an inverse power law dependence on distance, meaning that at small separations it dominates the double-layer repulsion force, which is near-exponential. This means that the net force between same-charge particles or surfaces is attractive even at very close separations, resulting in adhesion at molecular contact. It is at such separations that the behaviour of interfaces diverges from the classic mean-field theories that are used to define media at large separations. In the bulk scenario, where the medium is considered as a continuum, the van der Waals force and double-layer force are well defined.

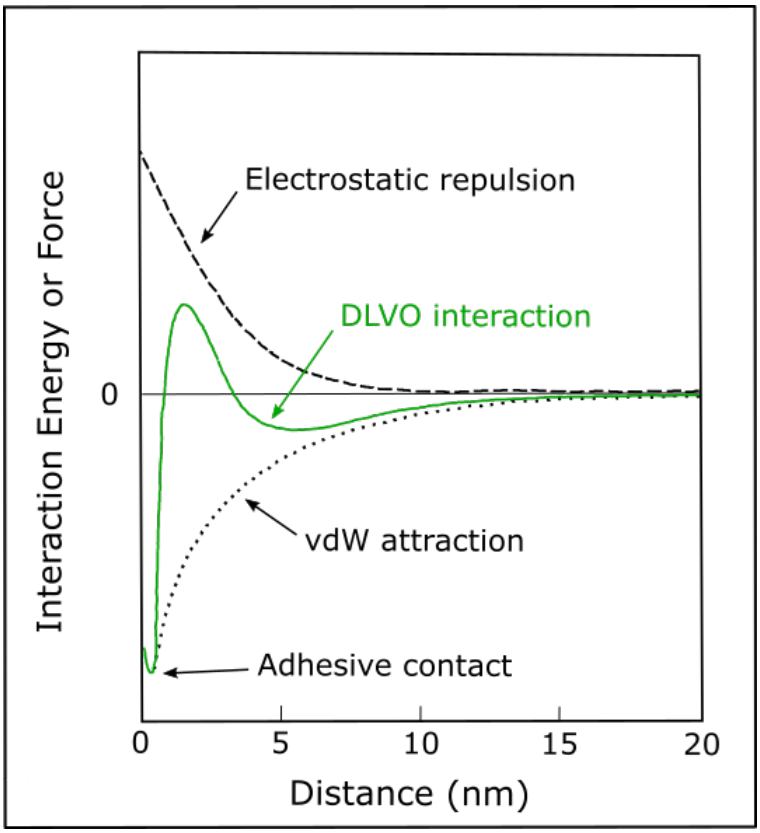


Figure 2.3: *The net DLVO interaction is a function of surface separation between two surfaces in an electrolyte solution [89]. It is made up of attractive van der Waals force and double-layer repulsion; the van der Waals force dominates due to its inverse power law distance dependence, which mean that the overall force is attractive.*

2.9 Electrostatics at High Ion Concentrations

Within the Poisson-Boltzmann equation and DLVO theory described above, electrolytes are treated as a liquid composed of fully dissociated ions of point charge and experiencing a mean electrostatic field. Under this assumption, concentrated electrolytes and ionic liquids, which are composed exclusively of ions, are expected to have Debye screening lengths of the order of 0.01 nm [21, 23], which is less than the diameter of most molecules. This being a physically impossible screening length suggests a significant departure from bulk or continuum theory in these systems, and it has been suggested that no screening length is observed in concentrated electrolytes, or that the screening length is the same as the ion diameter [23, 25]. Currently there is no robust theory that describes

intermolecular and surfaces forces in concentrated electrolytes.

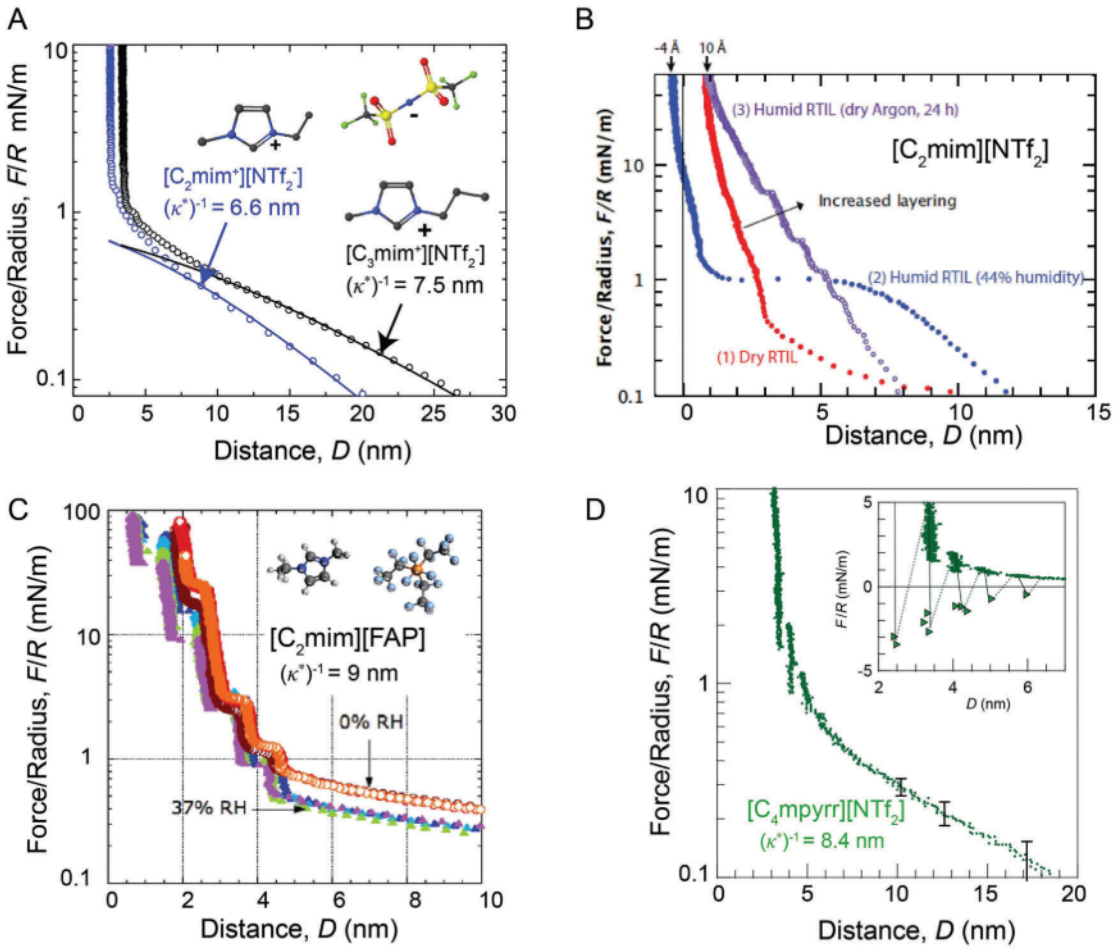


Figure 2.4: *Comparison of force-distance profiles in SFB (SFA) between two mica surfaces across different ionic liquids with varying humidity, measured by various research groups. In all of these measurements, long-range repulsive forces with a characteristic decay length of* $(\kappa^*)^{-1} \sim$ *5–10 nm are observed in dried ILs and ILs exposed to low humidity conditions (RH* $\leq$ *37%). Forces measured across (A) dried [*C_2*mim*$^+$*][*NTf_2^-*] (blue) and dried [*C_2*mim*$^+$*][*FAP^-*] (black) by Gebbie et al. [90], (B) dried (red), humid (blue) and semi-humid (purple) [*C_2*mim*$^+$*][*NTf_2^-*] by Cheng et al. [91], (C) dried (orange, red) and semi-humid (purple, blue, green), [*C_2*mim*$^+$*][*NTf_2^-*] by Espinosa-Marzal et al. [92], and (D) dried [*C_4*mpyrr*$^+$*[*NTf_2^- *by Smith et al. [25]]. Graph from Gebbie, M. A., Smith, A. M., Dobbs, H. A., Lee, A. A., Warr, G. G., Banquy, X., Valtiner, M., Rutland, M. W., Israelachvili, J. N., Perkin, S., & Atkin, R. (2017). Long range electrostatic forces in ionic liquids. Chemical Communications, 53(7), 1214–1224.*

A wide range of theoretical [15, 77, 86, 93, 94], computational [17, 19, 27, 95] and experimental works [1, 9, 21–24, 26, 44, 57, 96, 97] have been dedicated to elucidating what forces are acting in concentrated electrolytes in the

EDL and at longer ranges.

In the past 10 years, significantly longer-ranged screening lengths have been reported and investigated in ionic liquids [22–24]. These have been termed "underscreening", in reference to the observation that the concentrated electrolyte solution does not screen the charged surfaces as much as expected in the Debye-Hückel model, giving rise to significantly longer-ranged decay lengths. As stated in section 2.1.2, in the context of mean-field theory, Debye-Hückel theory is valid when $l_B^3 c_{ion} << 1$. This means that Debye-Hückel is applicable only when ion-ion separation is much greater than the Bjerrum length, which allows for Coulomb interactions between ions to be treated as perturbations. As a consequence, Debye-Hückel theory is only valid in dilute electrolytes.

Fig. 2.4 shows examples of a long-range repulsive force observed in dried, humid and semi-humid ILs as measured with SFBs/SFAs between two mica surfaces by various research groups. These demonstrate that this long-ranged force can be observed experimentally in a repeatable way in a variety of ILs. They have also been measured with AFM [2, 98].

Interestingly, computational and experimental results can be at odds when it comes to long-range forces in concentrated electrolytes [19, 21, 99, 100]. Fig. 2.5 shows various results from experimental and computational studies. Fig. 2.5 (A) is a plot of λ_S/λ_D vs σ/λ_D with computational results from Rotenberg *et al.*. It shows that there is a cross-over from the low-density Debye regime to the high-density regime where λ_S increases with density once a critical density (where $lambda_D$ is similar to ion diameter) is passed. The ratio λ_S/λ_D increases to a power law, which confirms the same result from experimental data, although the rate of increase is found to be slower for the computational results. Fig. 2.5 (B) shows the same type of plot, but with experimentally obtained data. Fig. 2.5 (C) shows results from molecular dynamics (MD) simulations, where the screening lengths obtained computationally do not follow the same regime.

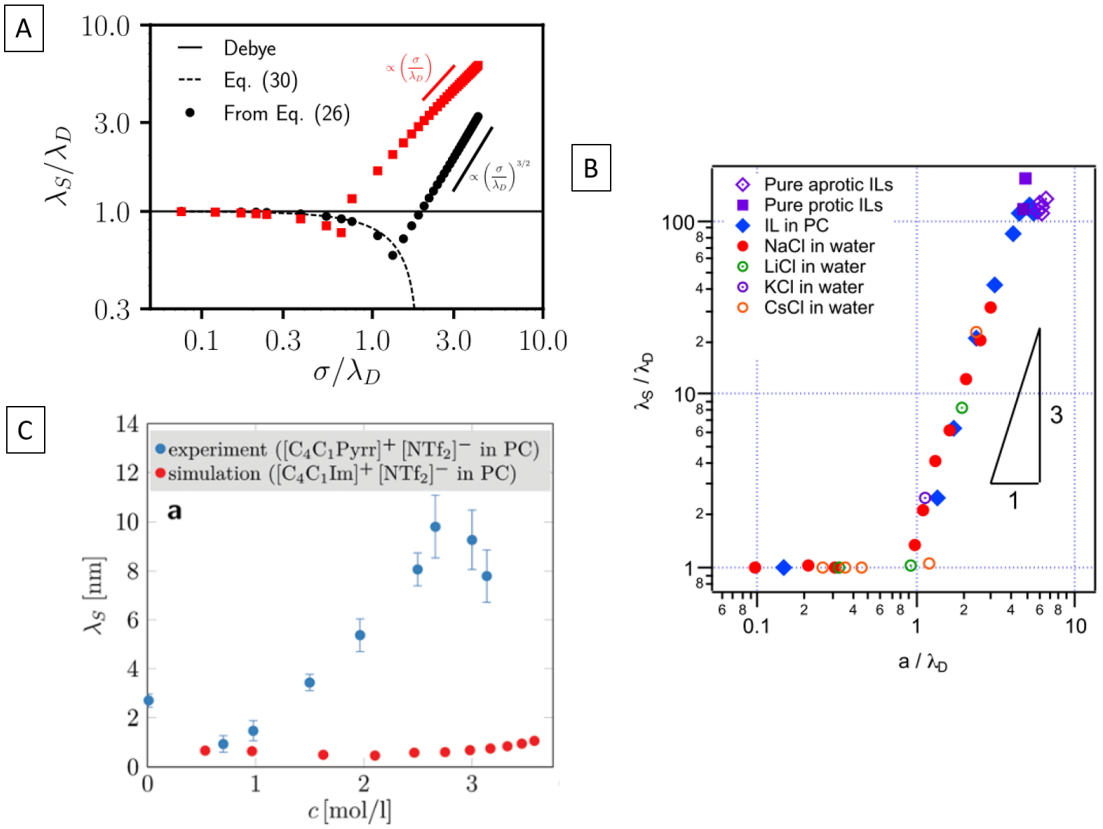


Figure 2.5: *Comparison of computational and experimental results obtained by various research groups. (A) Ratio between the screening length as a function of the ratio between the ion diameter and the Debye screening length for* $l_B/\sigma = 2.3$*. The solid lines correspond to the Debye prediction* $\lambda_S = \lambda_D$*, the dashed lines are the Landau fluctuation theory results (see [101]) using the mean-spherical approximation (MSA) predictions for the thermodynamic quantities* $\chi^{-1}_{\alpha,\beta}$*. The circles correspond to calculations from the complex poles of the structure factor* $S_{ZZ}(k)$ *for the two-component primitive model (ions treated as charged hard spheres, solvent implicit) and the squares for the three-component semi-primitive model (ions treated as charged hard spheres, solvent molecules treated as neutral hard spheres).Graph from Rotenberg, B., Bernard, O., & Hansen, J.-P. (2018). Underscreening in ionic liquids: a first principles analysis. Journal of Physics: Condensed Matter, 30(5), 054005. (B) Experimentally measured screening length,* $lambda_S$*, normalised by* λ_D*, plotted against* a/λ_D *for a range of pure ILs, IL mixed with propylene carbonate (PC) molecular solvent, and various 1:1 inorganic salts in water. Data for LiCl and CsCl are literature values [102]. Graph from Lee, A. A., Perez-Martinez, C. S., Smith, A. M., & Perkin, S. (2017). Scaling Analysis of the Screening Length in Concentrated Electrolytes. Physical Review Letters, 119(2), 026002. (C) Concentration-dependent screening lengths* λ_S *obtained from molecular dynamics (MD) simulations compared to those obtained from experimental SFB measurements. Blue dots are experimentally determined electrostatic screening lengths of* $[C_4C_1pyrr]^+[NTf_2]^-$ *in PC, and red dots are simulation results of* $[C_4C_1im]^+[NTf_6]^-$ *Graph from Zeman, J., Kondrat, S., & Holm, C. (2020). Bulk ionic screening lengths from extremely large-scale molecular dynamics simulations. Chemical Communications, 56(100), 15635–15638.*

In 2017, Lee *et al.* reported an experimental finding in concentrated electrolytes that showed:

$$\frac{\lambda_S}{\lambda_D} \sim \left(\frac{a}{\lambda_D}\right)^3 \tag{2.21}$$

Where λ_S is the screening length observed in concentrated electrolytes. This means that the decay length changes as a function of ion concentration and of Bjerrum length:

$$\lambda_S \sim l_B c_{ion} a^3 \tag{2.22}$$

Where a is the ion diameter, and proposed that underscreening is purely a property of the liquid [22]. While there is little doubt that this effect exists, its origins remain a subject of much debate [21, 22, 103, 104].

This thesis proposes some answers and some questions regarding the effect of surface potential on underscreening and surface forces.

2.10 Structural Forces

When confining a liquid between two surfaces, it can be treated as a continuum as long as the surfaces are far apart. When the surfaces are brought closer together ($<$10 nm), the continuum model breaks down and it becomes necessary to consider the liquid as an ensemble of individual molecules, which may constrain the distribution of charge or density [26, 27, 38, 44, 105]. Since the liquid is no longer considered a continuum but a grouping of molecules, new parameters come into play: molecules are well-defined, with properties such as geometry and polarity that help determine the way in which they pack or move. The confining surfaces also interact with each other and impose order on the liquid, so if one of them is planar, the structure of the molecules will be templated to it and adopt an ordered structure dependent on the properties of the molecules (*e.g.* charge, sterics, flexibility); this introduces structural forces (also known as

solvation forces), which are not predicted in mean-field theory [10].

In the solid crystalline state, molecules have long-ranged order. In the liquid state, they do not completely lose this ordering; instead of having discrete positions in a lattice, the positions of the molecules in the liquid state are defined by a density distribution function. Although molecules can move around in the liquid state, there is still significant restriction of their freedom as they hinder each other and are hindered by the geometry and size of the confining space.

Structural forces define how a liquid will behave when it is confined to the nanometric scale, and this is especially true when the molecules are fairly symmetric and confined between rigid solid surfaces. Structural forces are oscillatory, switching between attraction and repulsion depending on the thickness of the film between the surfaces; periodicity is related to molecular size, whereas oscillations are related to the density function of the liquid [106, 107]. There are many variables depending on the system, but overall the density profile (pair distribution function) $\rho(r)$ oscillates as a function of distance away from a given molecule until it reaches bulk density ρ_0.

In a system where the liquid and the walls do not interact, the structural force can be expressed through the electrostatic double-layer pressure between two charged surfaces across a liquid containing counterions and solvent molecules can be expressed as:

$$P(D) = kT[\rho_S(D) - \rho_S(\infty)] = kT[\rho_m(D) - \rho_m(\infty)] \tag{2.23}$$

Where ρ_S is the density of molecules at each surface and ρ_m is the density of molecules at the midplane. This gives us a decaying oscillatory function, where $\rho_S(D)$ is high when surfaces are close together and becomes smaller as surface separation increases. Surface separation is “in phase” with the molecules packing. When the surfaces are far apart, $\rho_S(D)$ approaches $\rho_S(\infty)$, which means

that the density of molecules at the surfaces is almost that of the density at isolated surfaces, and thus that the structural pressure approaches zero. This corresponds to the disappearance of the oscillation, which has a range of several molecular diameters and a periodicity of about one molecular diameter.

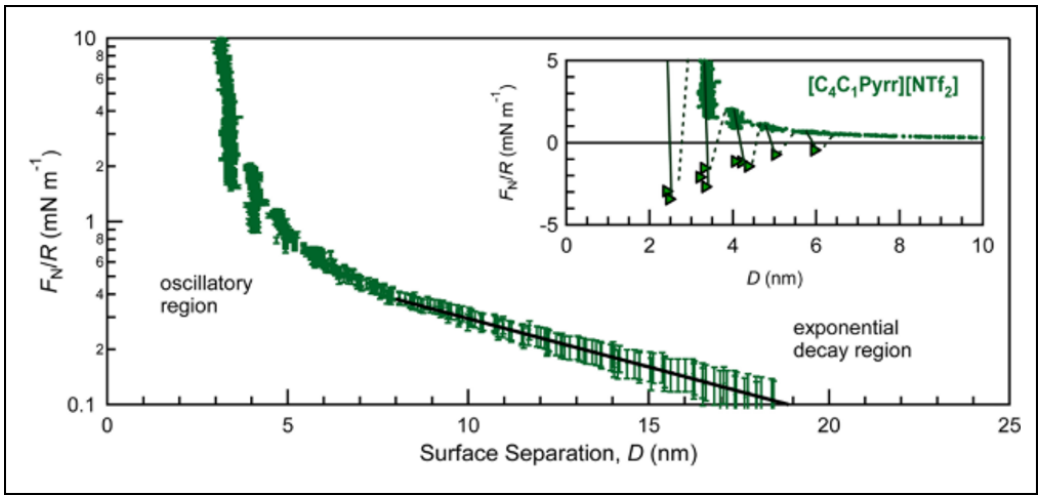


Figure 2.6: *Example of a force profile exhibiting layering caused by structural forces in pure C_4C_1pyrr TFSI. The oscillatory region at approximately 6 – 3 nm shows characteristic steps, evidence of molecular layering. The surfaces "step together" when a maximum in the oscillatory force is reached. The distance between these steps corresponds to the thickness of a bilayer of the ionic liquid. In the 19 – 6 nm region, the force becomes a monotonic exponential decay. The inset shows the oscillatory region in more detail; the triangles show data points corresponding to the retraction of the surfaces from each other. During a retraction, the surfaces "step out" when a minimum in the oscillatory force is reached. Together, the dotted lines and the solid lines show the overall oscillation. From Smith et al. [25].*

Practically, in force measurements this manifests as "jumps" or "steps" in the force profiles when surfaces approach each other at small separations, as seen in Fig. 2.6. When bringing the surfaces together, each step corresponds to a layer of molecules being squeezed out, with the start of the "step" corresponding to an energy maximum in the oscillation; as elaborated above, the closer the confining surface are to contact (i.e. the smaller the confining space), the higher the maximum. On retraction, when moving the surfaces apart, the layers are "pulled" back into the slit at points corresponding to the energy minima. In ionic liquids, these jumps or steps in the force profiles are widely agreed to be alternating bilayers consisting of a cation and an anion layer, so as to preserve overall

electroneutrality [9, 92, 108].

It is possible to describe the force F_N between two classic SFB mica surfaces with radius of curvature R across concentrated electrolytes with an empirical expression [27, 109]:

$$F_N/R = Ae^{-D/\lambda_o}\cos(\omega D + \phi) + Be^{-D/\lambda_S} \tag{2.24}$$

Where D is the distance between the surfaces, A is the magnitude of the oscillation, λ_o is the decay of the oscillatory structural force, $2\pi/\omega$ is the wavelength of the oscillatory structural force, ϕ is the phase shift of the oscillation. Be^{-D/λ_S} is the expression for the long-ranged monotonic decay observed in concentrated electrolytes, where B is the magnitude and is surface-dependent, and λ_S is the decay of the long-ranged force and is a property of the bulk. In force measurements, F_N, R and D are obtained directly, whereas the rest of the parameters are obtained by fitting.

It should be noted that the presence of attractive intermolecular or liquid-solid interactions within the system are not necessary to observe structural forces. The oscillations may be observed in any system where a liquid composed of relatively symmetric molecules is confined between atomically smooth surfaces. Intermolecular forces do contribute to the overall pressure within the slit when they are present (as is the case in real liquids), but oscillations can still be observed. It is equally important to stress that structural forces arise from the disruption of the ordering of molecules close to a hard surface by moving the surfaces closer or further apart, not from the ordering itself. Additionally, the character of the molecules greatly affects the structural force: molecules that are softer (i.e. not the ideal hard shells used in the theory) and/or asymmetric will exhibit fewer oscillations. Sterics, intermolecular forces and liquid-solid interactions, to name but a few, also may affect the character of the oscillations, and as is the case with very asymmetric or soft molecules, oscillations may not be observed at all.

Chapter 3

Experimental Techniques : The Surface Force Balance

3.1 Introduction

This chapter presents the surface force balance (SFB) (also known as the surface force apparatus (SFA)), its operation and how the data collected with it are analysed and interpreted. Here we shall refer to it as the SFB, as this is the name that is used in our research group.

Several types of SFAs and SFBs exist [42], but the ones used for the experiments discussed in this thesis are based on setups proposed by Chai and Klein [60] (for the Asymmetric Gold/Mica SFB) and by van Engers *et al.* [45] (for the Triple Gold Mirror SFB (Au3 SFB)), both of which are described in later sections of this chapter.

The classic SFB setup is presented first, so as to provide context for the gold/mica SFB and Au3 SFB, which are described in detail. Improved fabrication methods are proposed for the gold lenses, consistently yielding ultra-smooth

surfaces that afford better resolution for the electrochemical setups.

3.2 The Classic Surface Force Balance

The surface force balance is an apparatus that can be used to measure the absolute distance between two surfaces, as well as the static and dynamic forces acting between them in the normal and lateral plane. This can be done for a range of distances, from tens of μm down to the diameter of a molecule. Optimally the resolution is of 0.1 nm, which means that the SFB can be used to probe distances and forces down to the scale of a molecule [9, 26, 27, 42, 159].

For these measurements to have sub-nanometric resolution, the surfaces between which the medium is trapped need to be atomically smooth, with a large surface area compared to the confined space [39], conditions fulfilled by single muscovite mica facets cleaved down to a thickness of 2-4 μm and which can have a surface area of several cm^2 [55]. The mica pieces are deposited with the freshly cleaved side down on a basesheet, a larger sheet of freshly cleaved, atomically smooth mica, and silver is evaporated slowly onto it using physical vapour deposition (HHV Auto306 (HVV Ltd.)). This results in pieces of atomically smooth mica being back-silvered, creating a silver mirror with a mica spacer [39, 41, 43].

In the classic setup depicted in Fig. 3.1, two pieces are cut from a single crystal of back-silvered mica and are glued with EPON 1004F epoxy glue (Shell, refractive index n=1.54$\pm$0.03) to two hemicylindrical quartz lenses (radius of curvature = 1 cm), silver side down, mica side up. The bottom lens is mounted into a holder that itself is mounted on leaf springs in a boat (spring constant 141 Nm^{-1}). In some SFB setups, the holder may be mounted directly onto the boat, if there is a need for a near-infinitely stiff spring. The top lens is mounted onto a holder

attached to a piezoelectric tube and lateral leaf springs, which allow for the measurement of lateral forces. A capacitance probe is calibrated to be sensitive to the movement of the lateral leaf springs, where any change in the position of springs will result in a change in distance between the probe and the lens holder. The change in capacitance is measured and is used to measure lateral forces.

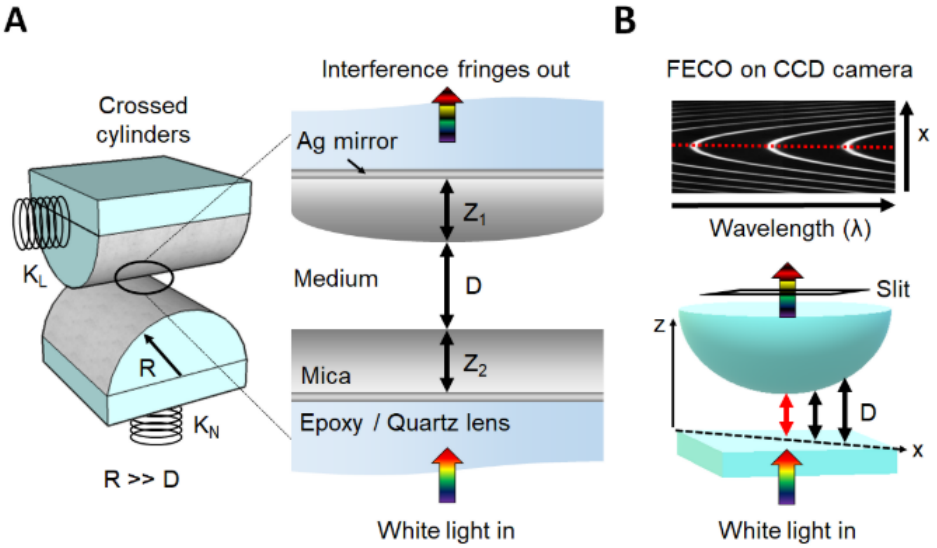


Figure 3.1: *Diagrams illustrating the fundamental principles of the classic SFB setup. (A) Two cylindrical lenses are mounted on springs in a cross-cylindrical geometry, where the radius of curvature of the lenses R is much greater than the distance between the surfaces D. When the springs are deflected, the normal and lateral forces causing the deflection can be measured; the spring constants of the normal and lateral springs are K_N and K_L respectively. The lenses are coated in back-silvered mica by glueing the mica silver-side down with an epoxy that has been refractive index-matched to the lenses. The interferometer is bounded by the silver mirrors, and the mica pieces, taken from a single crystal of even thickness, serve as a spacers Z_1 and Z_2 so that $Z_1 = Z_2$. White light is shined in, and any that interferes constructively across the interferometer $Z = Z_1 + D + Z_2$ emerges as interference fringes. (B) The interference fringes appear as curves, reflecting the shape of the geometry of the lenses, i.e. a sphere on a flat surface. At a given wavelength, only certain specific values of Z have constructive interference, and the light emerges as fringes of equal chromatic order (FECO).*

The lenses are mounted into the chamber of the SFB with their axes crossed (crossed-cylindrical configuration), so that the geometry is equivalent to that of a sphere on a flat plane. The crossed-cylindrical configuration is more

practical than parallel plates [10], which are effectively impossible to align. The Derjaguin approximation allows for the conversion of the force measured between the curved surfaces to the free energy of the interaction between parallel planar surfaces at the point of closest approach (equation 2.25). Distance measurement between the surfaces, accurate to the sub-nanometric scale, is achieved through the use of multiple beam interferometry (MBI).

There are three modes of control for the distance D between the surfaces of the lenses, each with different degrees of precision; two are motors, which move the boat (bottom lens) and the third is the piezoelectric tube, which moves the top lens (see Fig. 3.2). The coarse motor, which moves the upper rod, is accurate to about 1 μm; the fine motor moves the lower rod, which in turn acts on a helical spring that bends a double-cantilever spring, is accurate to about 1 nm. The piezoelectric tube, which expands or contracts by applying a voltage, is accurate down to 0.1 nm. It can move the lens normally or laterally.

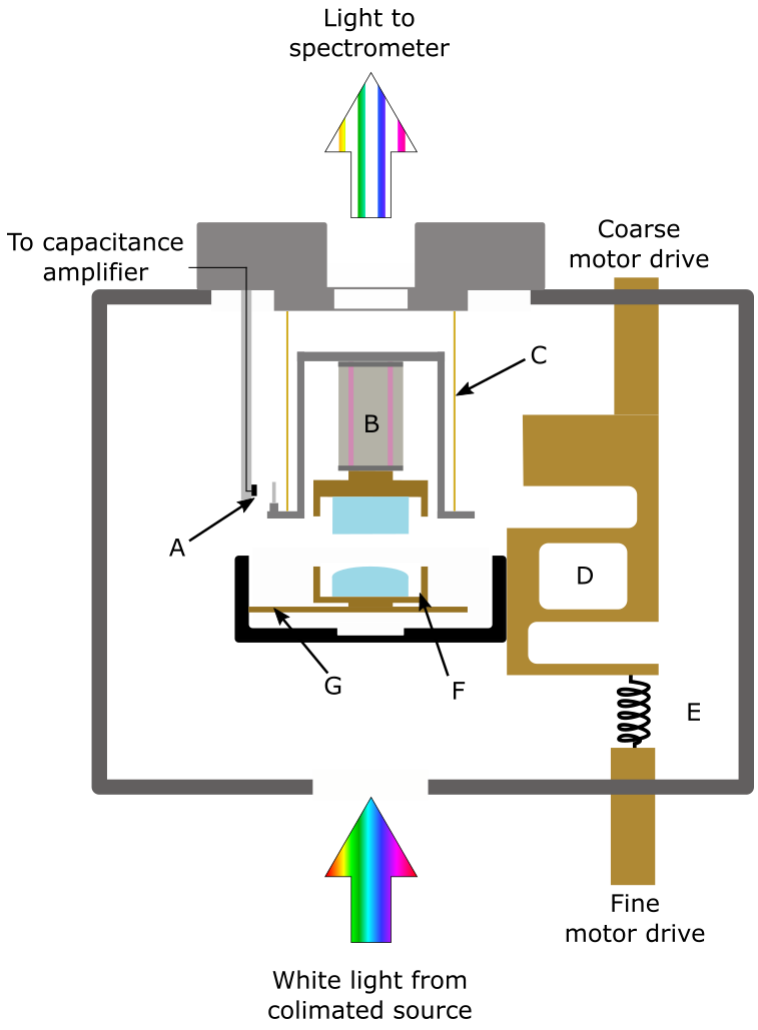


Figure 3.2: *Diagram of the SFB chamber, with (A) the capacitance amplifier, (B) the piezoelectric tube, (C) lateral leaf springs, (D) stiff spring, (E) helical spring, (F) bottom lens cup and (G) normal leaf spring.*

3.2.1 Interferometry: FECO in a Symmetric 3-Layer Interferometer

Multiple beam interferometry is used to measure the thickness and refractive index of a liquid film trapped between semi-transparent smooth mirrors. In classic SFB, muscovite mica is used as an atomically smooth surface and back-silvered to create a mirror, which creates an interferometric stack such that $silver \mid mica \mid liquid \mid mica \mid silver$. When shining white light through the stack, only constructive wavelengths pass through the mirrors to emerge into a spec-

trometer, which splits these into fringes, known as fringes of equal chromatic order (FECO). Visible-range white light is used, which means that the distance between the mirrors needs to be equal to or greater than the diffraction limit of the shortest wavelength of the light, and in turn means that there needs to be a spacer between the mirrors, a role filled by mica in the classic SFB setup. In the setup used for this thesis the FECO were recorded through a camera linked to the spectrometer and analysed separately. By measuring the relative distance between the fringes, it becomes possible to determine the absolute distance D between the two surfaces with sub-nm accuracy.

A line within the plane perpendicular to the normal of the surface is selected by the spectrometer slit, but as the distance D varies constantly, the condition for constructive interference changes as well. D is smallest at the point of closest approach, and increases away from the apex of the sphere on the flat surface (see Fig. 3.1 (B)), which gives us the curved fringes of equal chromatic order (FECO). The surface geometry can be measured directly from the FECO in the interferogram, and R can then be determined from there.

A calibration measurement is performed at the beginning of each experiment to determine the wavelength of the p and $p-1$ fringes (a pair of adjacent fringes) when the surfaces are in adhesive contact in air (i.e. $D = 0$). It is desirable to have both of these fringes in view within the same spectrometer window, as it is easier to determine the wavelength of each from the calibration image, and because it is easier to track the fringes when there are at least two in view at all times. The pixel position of the apex of the fringes are compared to those of the emission lines of mercury, which have known wavelengths, and from that we obtain a calibration for the pixel to wavelength value in the measurement, which is used to determine absolute separation of the surfaces. Here we detail the mathematical background to the interferometry used in classic SFB [40, 110–113].

We consider an interferometer with three layers of thickness Y, T, Y and

refractive indices of μ_1, μ_3, μ_1, where Y corresponds to back-silvered mica and T to an interstitial liquid film. We consider a ray of light of unit amplitude and zero phase issuing from the centre of the stack, where the centre of the stack corresponds to $x = 0$, as shown in Fig. 3.3.

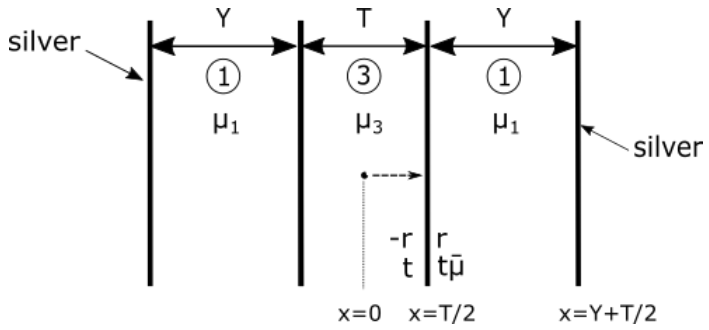


Figure 3.3: *Three layer interferometer, simplified. In this method, the ray of light is considered as originating from the middle of the stack. Diagram reproduced from the original in Israelachvili, J. ,(1973) Thin film studies using multiple-beam interferometry. Journal of Colloid and Interface Science, 44(2), 259–272.*

The coefficients of reflection are r and $-r$ and the coefficients of transmission t and $t\overline{\mu}$, where $\overline{\mu} = \mu_1/\mu_3$. For constructive interference, the sum of all components of the ray returning to $x = 0$ after reflections must have unit amplitude and phase of 0 or π, which is expressed as follows (assuming total internal reflections):

$$-re^{ik\mu_3 T} + t^2\overline{\mu}e^{ik(\mu_3 T+2\mu_1 Y)} + t^2\overline{\mu}re^{ik(\mu_3 T+4\mu_1 Y)} + ... + t^2\overline{\mu}(nr)e^{ik(\mu_3 T+2n\mu_1 Y)} + ... = \pm 1 \tag{3.1}$$

With

$$r = (\mu_1 - \mu_3)/(\mu_1 + \mu_3) = (\overline{\mu} - 1)/(\overline{\mu} + 1)$$

$$t = 2\mu_3/(\mu_1 + \mu_3)$$

$$\overline{\mu} = \mu_1/\mu_3$$

So that $r^2 + t^2\overline{\mu} = 1$

Which give us:

$$e^{ik\mu_3 T}\left[-r+\frac{(1-r^2)e^{2ik\mu_1 Y}}{1-re^{2ik\mu_1 Y}}\right]=\pm 1 \tag{3.2}$$

Which reduces to:

$$(1-re^{2ik\mu_1 Y})=\pm e^{ik\mu_3 T}(r-e^{2ik\mu_1 Y}) \tag{3.3}$$

748 Therefore we obtain fringes in the output light at values of $\lambda(k=2\pi/\lambda)$ that satisfy
749 this equation.

If we add to Y a constant Ψ to account for the phase change upon the reflection at the mirrors, where Ψ is a function of λ, we write the general equation for a three-layer symmetric interferometer:

$$\tan(k\mu_3 T)=\frac{(1-r^2)\sin(2k\mu_1 Y)}{2r-(1+r^2)cos(2k\mu_1 Y)} \tag{3.4}$$

750 Where $r=(\mu_1-\mu_3)/(\mu_1+\mu_3)$

If the two surfaces are in contact, $T=0$ and we have a single-layer interferometer of thickness $2Y$, so the above equation Eq. 3.4 is satisfied by:

$$2k\mu_1 Y=n\pi, n=1,2,3,... \tag{3.5}$$

Where n is the fringe order and the different orders are related by:

$$1/n=(\lambda_{n-1}-\lambda_n)/\lambda_{n-1} \tag{3.6}$$

751 Which means that the 1st fringe ($n=1$) has a wavelength of $\lambda=4\mu_1 Y$
752 and the 2nd fringe ($n=2$) has a wavelength of $\lambda=2\mu_1 Y$.

Eq. 3.4 can be rewritten in terms of wavelength [40]:

$$\tan(k\mu_3 T) = \frac{(1-r^2)\sin(n\pi\Delta\lambda_n/\lambda)}{\pm 2r + (1+r^2)cos(n\pi\Delta\lambda_n/\lambda)} \tag{3.7}$$

The positive sign is for odd n and the negative sign is for even n. This can also be written in terms of μ_1 and μ_3:

$$\tan(k\mu_3 T) = \frac{2\overline{\mu}\sin(n\pi\Delta\lambda_n/\lambda)}{(1+\overline{\mu}^2)\cos(n\pi\Delta\lambda_n/\lambda) \pm (\overline{\mu}^2 - 1)} \tag{3.8}$$

When considering small distances between the mica surfaces, we can use $\sin(n\pi\Delta\lambda_n/\lambda) = n\pi\Delta\lambda_n/\lambda$, $\cos(n\pi\Delta\lambda_n/\lambda) = 1$ and $\tan(k\mu_3 T) = k\mu_3 T$ to obtain the following expressions for odd fringes:

$$T = n\Delta\lambda_n/2\mu_1 \tag{3.9}$$

And for even fringes:

$$T{\mu_3}^2 = n\Delta\lambda_n\mu_1/2 \tag{3.10}$$

This tells us that if $T > 0$ at small separations, the shift of the wavelength of odd fringes will be different to that of the even fringes, as the former have no μ_3 dependency and the latter do.

3.2.2 The Geometry of Confined Spaces in SFB

The first step in understanding the phenomena that are being measured is to determine the geometry of the space being observed. We already know that the SFB uses lenses that are set up in a crossed-cylinder geometry, which can be expressed mathematically by the Derjaguin approximation [10] for two cylinders at a distance D and crossed at an angle θ, with their radii $R_1, R_2 >> D$. This is the

same as the expression for the interaction between a sphere and a flat surface.

$$F(D) = 2\pi\sqrt{R_1 R_2}W(D)/sin\theta \tag{3.11}$$

This expression is valid when R is much larger than D, which is the case in SFB, as R is usually about 1 cm, whereas D is of the order of 0 to a few hundred nm.

The Derjaguin approximation relates force $F(D)$ to interaction free energy $W(D)$, allowing a straightforward comparison between theoretical and experimental data. Indeed, theory tends to determine interactions between surfaces as energies, whereas experimentally it is simpler to measure interactions in terms of forces. Each experiment demands a new set of freshly made lenses, but as the equation is expressed in geometric terms, as long as separate experiments are normalised (i.e. scaled by the relevant geometric terms), one can compare results between them. As such, results are expressed as F/R, where R changes between experiments due to the fabrication process of the lenses.

3.2.3 A Classic SFB Experiment

The lenses are loaded into the SFB chamber with no liquid present between them, and the distance is calibrated by bringing the surfaces into contact in air, giving the fringe position for $D = 0$. Next the liquid is injected between the surfaces. The surfaces can be approached at constant velocity across the liquid, which yields a force profile, and this time the contact position, or the point at which the surfaces come into a single-asperity contact and stop moving, reflects the cumulative thickness of the layers adsorbed on each surface. Subsequent approaches or retractions may be performed at varying rates to observe the interaction between the surfaces, the deformation of the surfaces, the adhesion force between them, etc. Additionally, by using the piezo to induce lateral motion, one can observe frictional forces. Recording and analysing the fringes gives D

the absolute distance between the surfaces at any time.

3.2.4 Measuring Forces

Surface force experiments are a direct measurement of force between surfaces as a function of their separation, $F(D)$. In practice, it is much easier to measure forces between curved surfaces $F(D)_{curved}$ in a crossed cylinder geometry, as aligning parallel flat plates is excessively difficult to achieve experimentally [10]. The Derjaguin approximation allows us to relate $F(D)_{curved}$ to the interaction energy per unit area between parallel plates $W(D)_{flat}$:

$$W(D)_{flat} = F(D)_{curved}/2\pi R \tag{3.12}$$

Where R is the radius of the cylinders, where both cylinder have the same radius. By differentiating this, we obtain the force per unit area (*i.e.* pressure) for parallel plates, from the measured $F(D)_{curved}$:

$$P(D)_{flat} = -dW_{flat}/dD = -(dF_{curved}/dD)/2\pi R \tag{3.13}$$

In practice, one of the lenses (the bottom one) is mounted onto a normal spring with a known spring constant K_N, and this lens is moved at constant velocity towards the second one from a large inter-surface separation, where the change in surface separation is called ΔD. At large separations, in the absence of any forces between the surfaces, surface separation decreases at a linear rate, and the change is termed ΔD_O. When they become close enough for them to interact with each other, which results in a net force, the spring deflects by ΔD_S (measured by MBI), which allows us to calculate $F(D)$ simply through the relation:

$$F = K_N \Delta D_S \tag{3.14}$$

Which gives us:

$$F_f(D_f) = F_i(D_i) + K_N(\Delta D_0 - \Delta D) \tag{3.15}$$

Where F_f and D_f are the final force and distance and F_i and D_i are the initial force and distance between the surfaces. After calibration of the FECO pattern, the absolute distance D between the lenses is known, so for a sphere on a flat surface we can relate energy to force as a function of distance with Equ. 3.2, which can then be used to know the pressure between the two surfaces.

However, when the surfaces have a liquid trapped between them, it is often the case that a substrate adsorbs on the surfaces, and this layer rarely has infinite stiffness itself. This means that under applied force, the adsorbed layer will flex and can be defined by its own stiffness K^* so that $\delta = F/K^*$. The displacements are all related such that:

$$\Delta D_S = \Delta D_0 - \Delta D \pm \delta \tag{3.16}$$

To obtain the full force law, we consider moving the surface together by ΔD_0 from a large separation to a new, smaller one, which will cause the force between the lenses to go from $F = 0$ to a finite (measurable) F. The normal spring will deflect by ΔD_S, and the surface will deform by δ. In this SFB, K is much weaker than δ, so $\Delta D_S >> \delta$ and therefore if we have a measurable force at the new separation, we can express the force as a function of distance:

$$F(D) = K_N \Delta D_S = K_N(\Delta D_0 - \Delta D) \tag{3.17}$$

These different regimes allow us to plot data in the form of “force profiles”, as shown in Fig. 3.4. The region where there is no spring deflection ($\Delta D_S = 0$) is used to calibrate against the speed of approach of the the surfaces (Δz), as $\Delta D = \Delta(\Delta z)$. When the surfaces come into the range where

surface forces cause a deflection of the spring, ΔD_S is non-zero and we can use $F(D) = K_N \Delta D_S$ to plot the characteristic force as a function of distance.

Hydrodynamic forces arise from the velocity and acceleration of the molecules in solution and it is important to account for these. The force profiles shown in this thesis are of total force. In the case of the IL, the speed of the approach (0.5 nms^{-1}) was chosen to eliminate hydrodynamic forces, so there is no hydrodynamic contribution. The same is true for the measurements in KCl (aq). This can be shown by performing force profiles at different approach velocities. When the force profiles all converge, the hydrodynamic forces are no longer present. In the Oxford group, force profiles are presented as total force, and the force balance equation [114] is not automatically used in the analysis process. Additionally, former group member Dr. Romain Lhermerout developed a method to calculate a rough estimate of the minimum velocity for full hydrodynamic forces in a given system by inputting the viscosity and the radius of curvature of the lenses [115]. This confirms that the approach velocity used to measure force profiles in C_4C_1pyrr TFSI is far below the minimum approach velocity where hydrodynamic forces would be observed in this liquid.

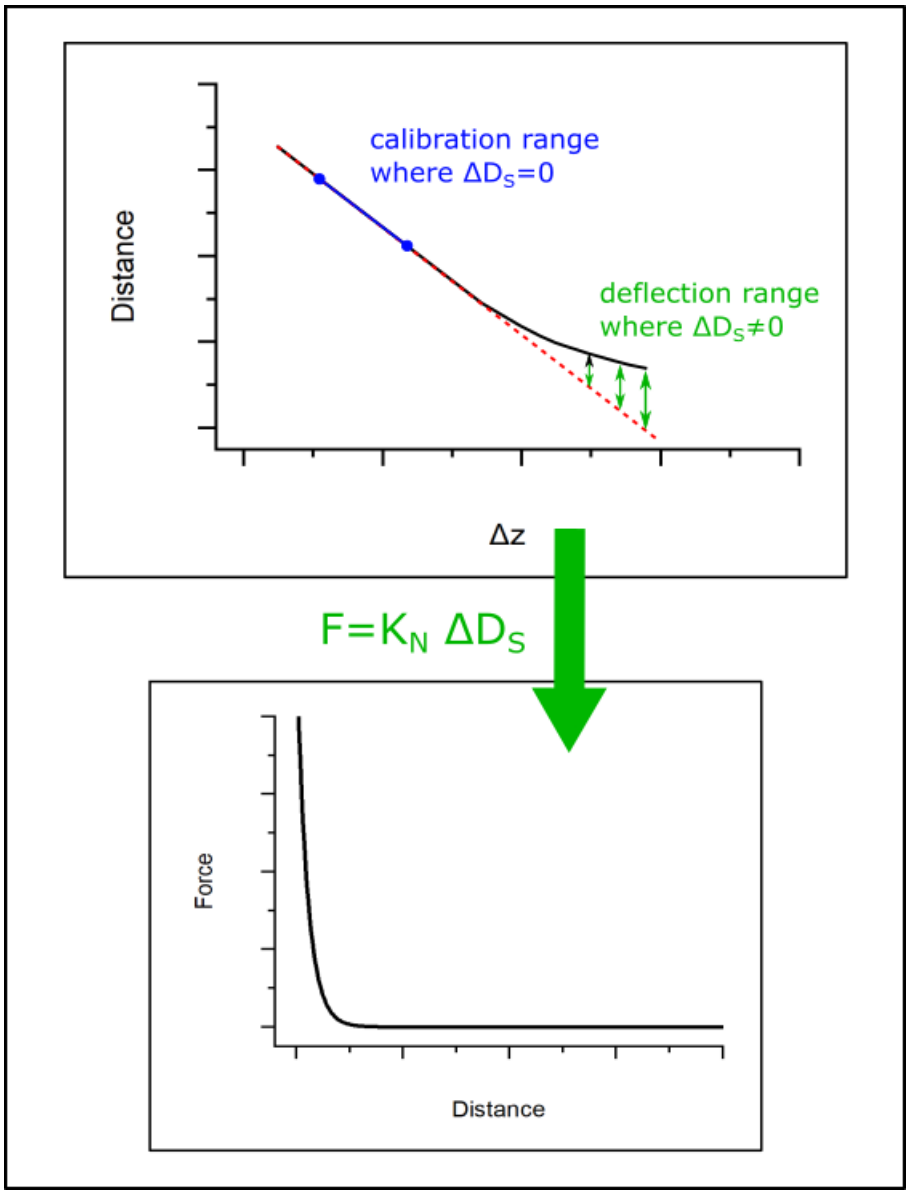


Figure 3.4: *The top plot shows how distance D changes as a function of applied change in the z direction (approaching the surfaces) Δz. When the surfaces are far apart (low Δz), the approach is linear, and the spring with known constant K_N is not deflected, so $\Delta D_S = 0$. This is used as a baseline. When the surfaces come closer together (high Δz), surface forces cause a deflection of the spring, deviating from the baseline. In this region, ΔD_S is non-zero, and using Hooke's law, we can plot force F vs distance D to obtain the profile of this deviation, as shown in the bottom plot.*

3.3 The Asymmetric Gold/Mica Setup

3.3.1 Introduction

Many modifications have been made to the classic SFB setup in order to explore different intermolecular and surface forces. Of particular interest is the ability to control and monitor the current and electrical potential of the surfaces of the lenses. Mica is an insulator, therefore a potential cannot be reliably applied to it and the surface current cannot be reliably monitored; this means that another material has to be used instead.

Ideally, when considering forces between two surfaces, it is preferable to consider two identical materials, as differing surfaces make analysis and interpretation all the more complicated [45]. However, symmetric metal/metal setups have proven extremely challenging to develop, and few have achieved ones that are both experimentally reliable and produce data that are easy to analyse [45–47]. Common problems are resolution and optical complexity, which limit the types of experiments that can be performed, and make the execution of measurements particularly time-consuming and technically difficult, as explored in Ch. 6.

As a result, symmetric metallic surface SFB setups have not entered mainstream use in the field, and for now asymmetric metal/mica setups remain the most pragmatic choice for electrochemical experiments. The complexity of interpreting results between dissimilar surfaces is largely outweighed by optical simplicity, higher resolution, robust surfaces and how much easier it is to perform the experiments overall.

The history of asymmetric gold/mica SFA/SFB setups is summarised here, but it cannot be divorced from that of the symmetric setups, which are described later in this chapter in section 3.4.. It should be noted that there are other asymmetric metal/mica setups using other metals, such as mercury [48]

and platinum [49]. The results reported in Ch. 4 and 5 were measured in a modified asymmetric gold/mica stack, which is described in this section. Some changes were made to this setup to improve optics and resolution, resulting in the distance resolution achieved in this thesis, which were previously unseen for this type of setup.

In 1998, Knarr, Quon and Vanderlick described an asymmetric SFA setup with template-stripped gold surfaces with a roughness of about 0.4 nm. They measured the adhesion between mica and gold, as well as the effect of roughness on adhesion [51].

In 2001, Fréchette and Vanderlick described an asymmetric polycrystalline gold/mica setup where the gold was under potential control and measured forces that changed as a function of applied potential. They used a slow thermal evaporation method to obtain gold surfaces with 0.4 nm average roughness [50, 51]. They proposed that this technique could be used to investigate potential-controlled adhesion in a liquid, roughness in relation to surface forces and potential control, and pointed out that smoother gold surfaces would be desirable.

Valtiner *et al.* proposed an asymmetric electrochemical Surface Force Apparatus (EC–SFA) in 2012 and explored the effects of surface roughness on surface force measurements [52]. They used template-stripped gold to obtain the atomically smooth surfaces. This setup was used in further studies, namely by Gebbie *et al.* in 2013 to show that ionic liquids behave as dilute electrolytes [23] and by Moremans *et al.* in 2016 for wetting of electrolyte on various electrode surfaces, where several SFA setups were used, including the classic mica/mica setup, the gold/mica setup previously described and a graphene/mica setup [53].

In 2015, Tivony *et al.* used a setup based on the Vanderlick *et al.* method and measured confinement-induced charge inversion at the gold surface [54]. They followed up these measurements in 2016 with further exploration of surface

properties of gold in electrolytes at low concentration [71] and in 2017 with modifying surfaces forces through modulating the potential of the gold surface [58]. Tivony *et al.* continued to harness the asymmetric gold/mica setup, characterising the charging dynamics of the SFB slit [72], opening a discussion on how a nanopore charges, how this affects the EDL and how to measure its behaviour. In 2021, they showed how potential control can be used to modulate the interfacial energy dissipation in the slit [116].

The asymmetric gold/mica setup used in this thesis was modelled after the Chai and Klein method for preparing gold surfaces [60] and by the electrochemical setups used by Klein, Tivony *et al.* and Valtiner *et al.* described above. Modifications were made to these techniques based on prior work from our own laboratory when developing Au3 SFB (discussed in the next section) [45]. Approaching the novel asymmetric setup from a much more demanding one meant that certain methods were carried over from Au3 SFB, resulting in improvements in resolution and reproducibility.

3.3.2 Gold/Mica SFB: Experimental Setup

This setup is in many ways similar to the classic SFB stack: distance is measured the same way and all the basic functions of the apparatus, such as measuring normal and lateral forces, are unchanged. The main changes are that one of the surfaces is coated in gold instead of silvered mica, and that the lens is mounted into the SFB slightly differently due to the introduction of an electrochemical cell.

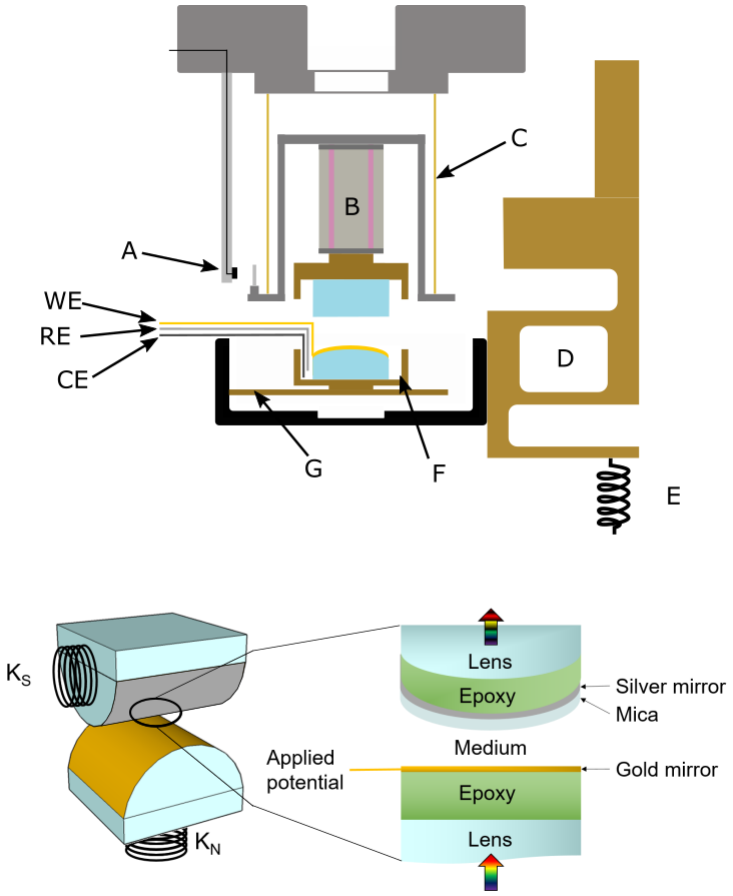


Figure 3.5: *Top: Diagram of the inside of the SFB with the asymmetric electrochemical setup, with (A) the capacitance probe, (B) the piezoelectric tube, (C) the lateral leaf springs, (D) the stiff spring, (E) the helical spring, (F) the electrochemical cup, (G) the normal leaf spring, (WE) the gold working electrode and wire, (RE) the silver pseudo-reference electrode and (CE) the platinum counter-electrode. Bottom: Diagram of the asymmetric gold/mica setup, where the bottom lens is coated in template-stripped gold (42 nm) on template-stripped EPON epoxy glue and the upper lens is coated in back-silvered mica (silver 45 nm). The gold surface serves simultaneously as a semi-transparent mirror, the lower confining surface and the working electrode of the electrochemical cell.*

Fig. 3.5 depicts the gold/mica setup. The interferometer is bounded by one gold and one silver mirror. The bottom lens is template-stripped gold 42 nm thick, while the top one is back-silvered mica, with the silver 45 nm thick. The fabrication of these is detailed below. The gold lens is mounted into a Teflon electrochemical cup, which is mounted onto the leaf springs of the boat. The gold lens is also the working electrode of the three-electrode electrochemical

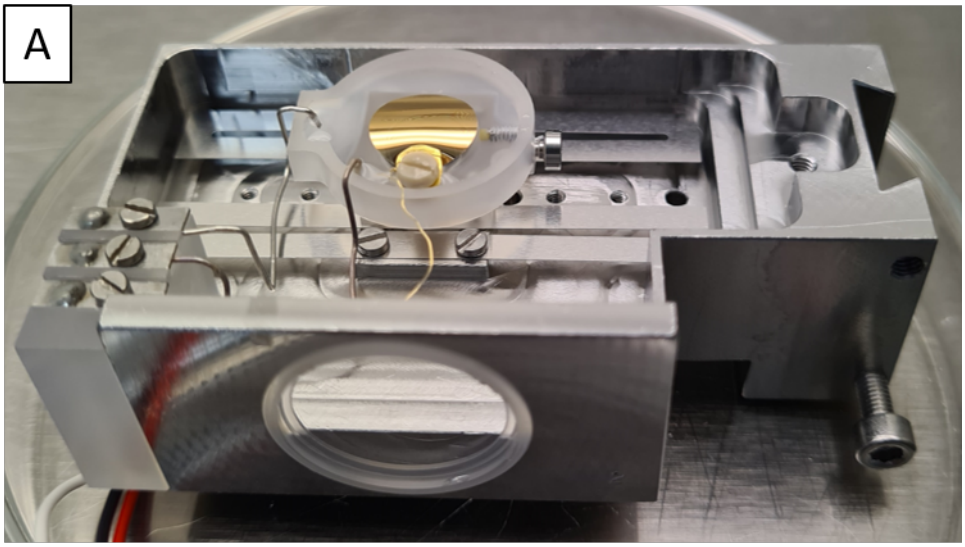
cell; a gold wire and a gold clamp are screwed into contact with the surface of the lens, far from the apex, as pictured in Fig. 3.6. The other end of the gold wire is screwed into a connector, along with the reference electrode (platinum) and pseudo-reference electrode (silver), which are dipped into the electrochemical cup. The connector is plugged into a potentiostat (Metrohm μAUTOLABIII/FRA2 impedance analyser). None of the wires can touch the cup nor the stainless steel boat, as this would cause mechanical coupling and/or an electrical short.

The templating of the glue with mica is used to obtain a uniform glue thickness across the lens. This makes template-stripping the gold layer much easier. If epoxy is applied by hand, it is harder to obtain uniformly smooth glue, which makes template-stripping harder. If there are ripples in the glue, when stripping, the mica may tear or the gold may not strip completely, leaving holes on the gold surface. Template-stripped glue makes laying down the gold more reliable and ensures that large areas of flat glue are obtained. Additionally, it is essential that the gold covers the lens all the way to the edge of the lens, so that the electrode may be connected from the side of the cup that holds the lens.

For the gold/mica setup, template-stripping the glue is not strictly essential, but it appears to yield better results in terms of reliably producing lenses that are completely covered in gold. The mica/mica setup prepares the glue by heating it, spreading it over the lens and waiting for the glue to smooth down on its own. For the gold/mica setup, heating and waiting after hand-applying glue is also an option. However, this tends to yield a smooth apex but lumpy edges as the glue bulges on the sides of the lens. If there are bulges on the edge of the lenses, the risk on tearing of mica or of uneven gold is higher.

The improved optical resolution is a factor of the quality of the interferometric system, but the combination of very smooth glue on the apex and good balance of reflectivity and transmissivity of the mirror seems to afford better resolution more reliably, and reduces the risk of off-apex roughness causing problems

with reaching the point of closest approach.



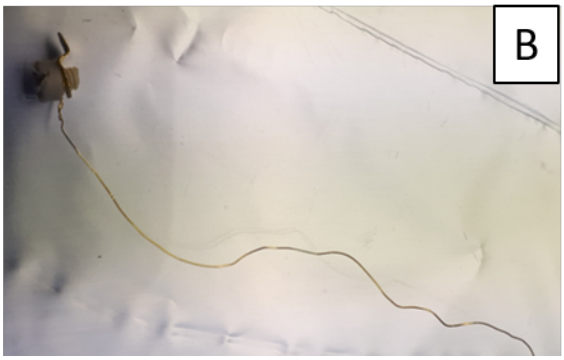


Figure 3.6: *(A) Bottom lens (gold) mounted in the electrochemical cell of the boat and connected by gold wire and clamp. The platinum CE and silver RE are also connected, and do not touch the side of the cup. The electrode connector on the left holds the CE, RE and WE wires in place. (B) The gold wire, Teflon screw and gold clamp assembled.*

Gold/Mica SFB: FECO in an Asymmetric 2-Layer Interferometer

The interferometer of gold/mica SFB differs from the classic SFB interferometer; the stack is $gold \mid liquid \mid mica \mid silver$, which is a two-layer interferometer (Fig. 3.7), as the lenses are index-matched to the epoxy glue used. The same method as for the 3-layer interferometer (*cf.* Section 3.3) is used to obtain the equations for the fringes in this system, but the equation for a 2-layer interferometer is different.

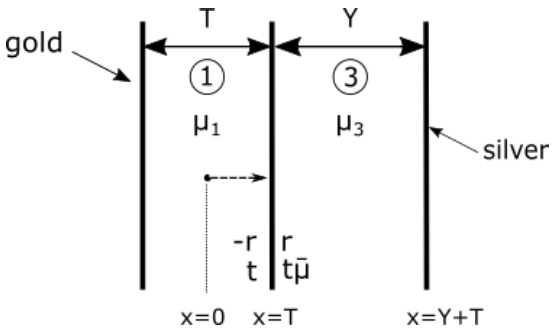


Figure 3.7: *Two-layer interferometer, simplified. In this method, the ray of light is considered as originating from the middle of the stack.*

We consider a beam of light incident on the stack at $x = 0$, where Eq. 3.3 is used. However, here the boundary condition is that the light returning to $x = 0$ must have phase 0 *only*. Thus T is substituted for $2T$ and ± 1 for $+1$, which gives:

$$-re^{2ik\mu_3 T} + t^2\overline{\mu}e^{2ik(\mu_3 T+\mu_1 Y)} + ... = +1$$

Which reduces to:

$$tan(2k\mu_3 T) = \frac{(1-r^2)\sin(2k\mu_1 Y)}{2r-(1+r^2)\cos(2k\mu_1 Y)} \tag{3.18}$$

When $T = 0$, the nth order fringe at wavelength λ^0 is given by $2k^0\mu_1 Y = 2n\pi$, or by $\mu_1 Y = n\lambda^0/2$. When T is finite, the fringe shifts by $\Delta\lambda_n$ to a wavelength λ, which is given by:

$$\tan(2k\mu_3 T) = \frac{(1-r^2)\sin(2n\pi\Delta\lambda_n/\lambda)}{-2r+(1+r^2)\cos(2n\pi\Delta\lambda_n/\lambda} \tag{3.19}$$

Where $\Delta\lambda_n = \lambda - \lambda^0$. This applies to odd and even order fringes, and thus for small separations, the same expression is used for both orders:

$$T{\mu_3}^2 = n\Delta\lambda_n\mu_1/2 \tag{3.20}$$

However this doesn't account for the phase changes. We introduce ψ the

phase change at the mica/silver interface, χ the phase change at the medium/gold interface, and D the distance between the surfaces, and rewrite:

$$\tan(4\pi\mu_3 D/\lambda + \chi) = \frac{2\overline{\mu}\sin(4\pi\mu_1 Y/\lambda + \psi)}{(\overline{\mu}^2 - 1) - (1 + \overline{\mu}^2)\cos(4\pi\mu_1 Y/\lambda + \psi)} \tag{3.21}$$

This means that at $D = 0$, the left-hand side of the equation has non-zero value, therefore there is no $(4\pi\mu_1 + Y/\lambda + \psi) = n\pi$ condition. To be able to solve this, it is necessary to know the values of ψ and χ, and Y needs to be calculated.

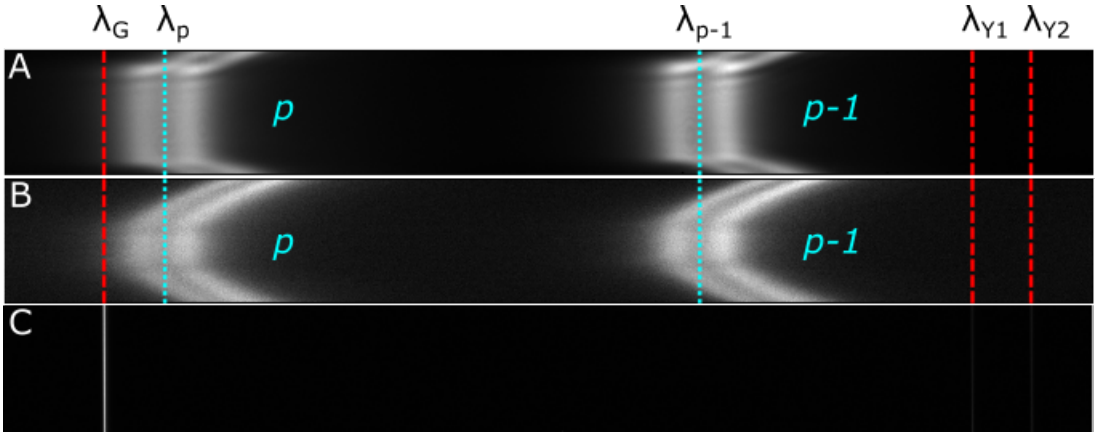


Figure 3.8: *(A) FECO of the gold surface in contact with the mica surface in air; (B) FECO of the gold surface and the mica surface at the point of closest approach in KCl (aq) 0.6 mM; (C) green λ_G and yellow λ_{Y1} and λ_{Y2} mercury emission lines. The values of λ_G, λ_{Y1} and λ_{Y2} are known, so the pixel position of each line can be converted to wavelength, and from these values, the wavelengths of the p and $p-1$ fringes, respectively λ_p and λ_{p-1} are obtained. The calibration for the wavelength corresponding to the separation $D = 0$ nm is obtained from the position of the p fringe in air (A), and from this the separation of the surfaces in all subsequent measurements can be known.*

In the gold/mica setup, the FECO look very similar to the fringes seen in mica/mica setups. Fig. 3.8 shows three images: (A) the FECO when the gold and mica surfaces are in adhesive contact in air, (B) the FECO when the surfaces are at the point of closest approach in a liquid (here it is dilute KCl (aq) 0.6 mM) and (C) the emission lines of a mercury lamp. The wavelengths are known of the emission lines are known to be $\lambda_G = 546.0735$ nm for the green line and $\lambda_{Y1} = 576.9598$ nm and $\lambda_{Y2} = 579.0663$ nm for the yellow lines, so the pixel position of each emission line can be converted to the corresponding wavelength.

From this calibration, the pixel position of the centre of mass of the p and $p-1$ fringes can be converted to their corresponding wavelengths λ_p and λ_{p-1}.

3.3.3 Making the Lenses

Due to their delicate nature and high sensitivity to contamination, SFB experiments require exceptional care in every step of preparing and assembling. All stainless steel tools and equipment (unless specified otherwise) were cleaned by sonicating in solvents (chloroform $\times 2$, toluene, isopropanol, ethanol), followed by rinsing ten times in deionised water and left in a nitric acid bath (2:1 water : nitric acid 70%) overnight. They were rinsed with deionised water immediately before use. All glassware (unless specified otherwise), including the lenses, was cleaned with the same solvents as the tools, rinsed ten times in deionised water and left in a piranha solution (3:1 concentrated sulfuric acid 99.9% : hydrogen peroxide 30%) overnight. The glassware was taken out of piranha and rinsed ten times in deionised water and dried in a laminar flow hood (LFH) immediately before use. All deionised water used came from a Milli-Q® IQ 7003 (Merck Millipore Limited) purification system, which provides deionised water with less than 2 ppb total organic content (TOC).

Gold Lens

Gold lenses are made ahead of time and in batches, usually several days or weeks in advance of the day of the experiment, and all steps are carried out in laminar flow hoods (LFH). As the face of the gold lens is adhered to the atomically smooth mica against which it is templated, it is protected from contamination or degradation until the mica is stripped off.

Before starting the fabrication process, it is necessary to prepare gold-

coated mica so that it is ready-to-use. This process is very similar to that of cleaving for back-silvered mica, with notable differences: the side of the mica piece that is of importance is the one facing *up*, as opposed to silvered-mica, when the *down* face (which will be the confining surface) must be as clean as possible. The single facets of mica being cleaved are used as a template for the gold, to produce the smoothest possible metal surfaces. As such it is imperative that the up-facing surface of the mica pieces be as clean as possible at the time of evaporation. A one hour window was used within the particle-free environment of an LFH to cleave all facets onto a thicker, freshly cleaved mica basesheet, to minimise the risk of any dust or contaminants depositing on the surface. It is also important that the single pieces be large enough to cover the whole surface of a 1 cm diameter lens, without the edges of the mica being more than a few mm larger than the area of the surface. Gold is slowly evaporated onto the mica pieces by physical vapour deposition (HHV Auto306 (HVV Ltd.)), with a particularly slow evaporation rate of 0.01 nms^{-1} for the first 2 nm, and a rate of 0.1 nms^{-1} for the remaining 40 nm.

Once the gold-coated mica facets have been prepared, the fabrication can begin in earnest. A single facet of muscovite mica (Ruby Mica Grade #1 V–1/V–2, S&J Trading, Inc.) is cleaved and placed on a 2 cm $\times$ 2 cm silicon chip (cleaned in solvents, piranha, RCA). The mica facet is carefully lifted with tweezers and 40 – 60 μL of ethyl acetate (Sigma-Aldrich, $\geq$99.7%, (EtOAc)) is dripped under it with an auto-pipette; this step ensures that the facet is laying completely flat on the chip and facilitates a future step. The chip is placed in a spin coater (Ossila Spin Coater; 3000 rpm; 30 s) and 40 μL of a solution of EPON 1004F epoxy glue (Shell, refractive index n=1.54$\pm$0.03 as measured by ellipsometry) in EtOAc (1g EPON for 3 ml of EtOAc) is dripped onto the mica facet and immediately spin-coated.

An NBaLF–5 lens (refractive index-matched to the glue) is placed on a

glass slide on a hotplate at 150° C. The silicon chip is placed on the hotplate as well. The heat causes the EtOAc under the mica piece to evaporate, creating bubbles that make lifting the mica off the chip possible. Using a sharp syringe needle and tweezers, the EPON-coated mica is lifted off the chip, taking care not to tear it. Once free, it is glued onto the lens by allowing the EPON-coated side of the facet to make contact with one of the lower edges of the hemicylindrical lens. Once contact has been made, the piece can be left to deposit itself, as the mica will "lay down" gradually as the glue/glass front travels across the surface of the lens. If the mica is cleaved thin enough, the whole facet will come down entirely on its own. If it is a little thick, one can lightly press down on the mica with clean tweezers to help it go down. It is preferable for the piece to go down on its own, as this will result in a very smooth, uniform coat of glue. If the piece is too thin, too thick, incorrectly placed, or poorly glued manually, this may result in gaps, ripples and/or bubbles in the glue, which are highly undesirable as a smooth point of closest approach is necessary for surface force experiments.

Once the mica piece has completely glued down, covering the whole surface of the lens, it is removed from the hotplate to cool down. After cooling, the mica can be stripped; this is done by completely immersing the lens in water and carefully stripping the mica off with tweezers. While stripping, the tweezers must not touch the surface of the glue and it is crucial that the mica does not tear, otherwise the subsequent step cannot be performed. Once stripped, the lens is left to dry before placing it in a dish on a hotplate for 30 min at 150° C to degas any remaining EtOAc in the glue, and to allow the glue to smooth further. After 30 min the lens is removed to cool down.

To proceed with the gold-coating step, the lens is placed back on the hotplate. A gold-coated facet of mica is lifted from its basesheet (prepared beforehand) with a needle and tweezers, and glued gold side down onto the lens. Just as with the EPON-coated mica, the piece is deposited by allowing the edge

to come into contact with one of the low sides of the lens, and then left to deposit itself. It is therefore important to cleave the mica pieces for gold coating such that they are thin enough to glue themselves down, but not so thin that they go down too quickly, which leads to ripples or bubbles. The ideal thickness is estimated to be about 4 μm. Once the gold-coated mica is completely glued to the surface, the lens is removed from the hotplate to cool down. The mica is left on the surface as a protective layer, and is only stripped off immediately before the lens is mounted into the SFB.

This fabrication method yields extremely smooth polycrystalline surfaces on very smooth glue, which affords excellent sub-nanometric resolution in combination with a silvered mica lens, as evidenced by the results described in the next two chapters.

Silvered Mica Lens

The silvered mica lens is made on the day of the experiment. An NBaLF–5 lens (1 cm diameter) is placed on a hotplate at 180° C and EPON epoxy glue is dabbed onto it before being smoothed with the side of a needle. When the glue is smooth and free of imperfections, a piece of back-silvered mica (vapour deposited, Ag 45 nm thickness) is cut and glued onto the surface. In these experiments, pieces with large surface areas compared to mica/mica experiments were used as there is no need to cut two pieces from the same single crystal. The larger piece also affords more choice in the position of the top lens over the bottom one, which helps position the stack so that the top lens doesn't touch any of the screws or wires used in the electrochemical cup. The thickness of the mica needs to be tailored to the asymmetric setup, as it needs to be thin enough to be deposited on the lens but thick enough for there to be at least two interferometric fringes in view. If too thick, it will not stay glued down due to the rigidity of thicker pieces, and if too thin, only one fringe will be in view at a time in the spectral range

of the spectrometer. This makes tracking the fringes difficult during the analysis, as single fringes pass out of view before the next comes into view when the surfaces are near the point of closest approach. Single-fringe experiments require extra calibration measurements to determine the wavelengths of the p and $p-1$ separately.

3.3.4 The Classic Three-Electrode Cell

To understand the SFB three-electrode cell, one must first review the basic principles of the three-electrode cell. For a majority of electrochemical measurements, the three electrode cell shown in Fig. 3.9 (A) is used as it is both a versatile and reliable method.

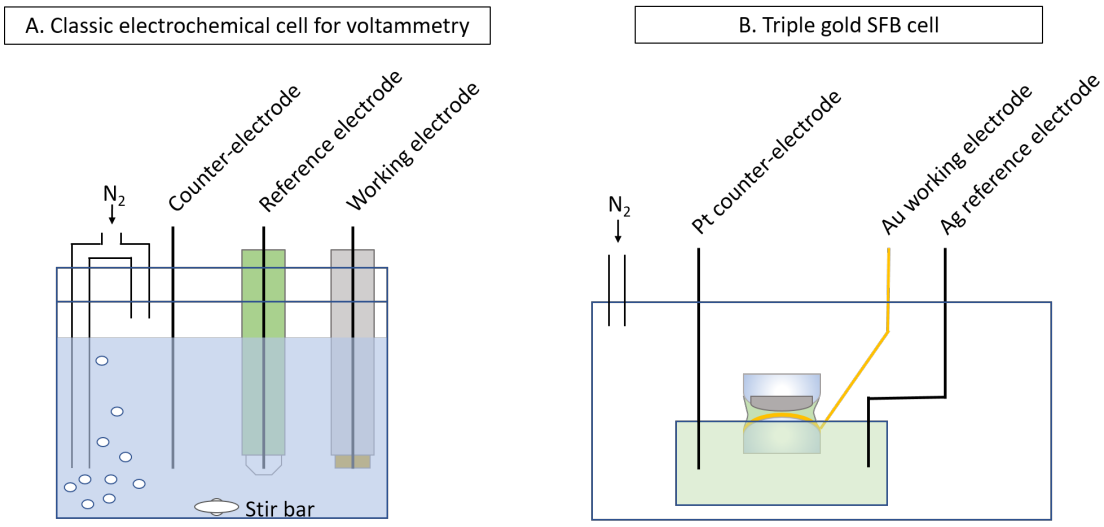


Figure 3.9: *(A) The classic three-electrode cell. A potential is applied to the WE and current flows between the WE and the CE, which is measured against the RE. The nature of each of these electrodes varies depending on the experimental specifications and the electrolyte being used. To eliminate unwanted oxygen from the system, nitrogen gas is often bubbled through the liquid, and the cell is sealed. (B) Diagram of the gold/mica SFB electrochemical cell. The functioning is the same as the conventional cell. The WE is gold, the CE is platinum and the pseudo-RE is silver. The SFB chamber is purged with nitrogen gas and sealed before starting measurements.*

As illustrated in Fig. 3.9 (A), the electrolyte is contained in a closed ves-

sel through which nitrogen gas is bubbled in order to remove oxygen, as it could interfere with reactions when the electrodes are at work, either by reacting with the surface of an electrode or by dissolving into the electrolyte. The nitrogen is used to purge the system, after which it is shut off and the vessel is sealed. The electrolyte solution is composed of charged ions which will migrate through the liquid when potential is applied in order to preserve overall electroneutrality. Electrolytes range from salts dissolved in solvent to ionic liquids, molten salts to deep eutectic solvents, and thus are tremendously versatile. It is extremely important that the electrolyte, whatever its composition, be pure; any impurity could affect the electron-transfer process and could lead to incorrect measurements.

There are three modes of transportation for ions to move through the liquid: diffusion, migration and convection. Diffusion occurs when there is a difference in concentration between two areas in the liquid. Ions will move from concentrated areas to more dilute ones. Migration is caused by the presence of an electric field, which attracts oppositely charged ions. Convection is induced by mechanical force (*e.g.* stirring, sonication). Measures should be taken to minimise these effects, such as ensuring that there are no vibrations.

There are many options when it comes to the choice of electrodes; the nature of the electrolyte and the electrochemical window (the potential range where no irreversible changes occur at the working electrode) will influence this choice. The three electrodes each have a different function: The working electrode (WE) is the one at which the current will be applied – it is where the event of interest occurs. The counter-electrode (CE) is the one to which the current will flow (from the WE) when potential is applied; it closes the circuit. The reference electrode (RE) measures accurately the potential applied to the system relative to a reference reaction. The current flows from the counter-electrode to the working electrode and is measured against the reference electrode (noted as *vs RE*) [117].

In terms of the electrochemistry, because the current flows from WE to CE, a reduction (donation of electrons) occurs at the WE and an oxidation (uptake of electrons) occurs at the CE; this exchange is known as a redox reaction. The material of the WE must be inert to the redox reaction in the electrochemical window being studied, and needs to be extremely clean, especially if the material used is very sensitive to air or water (*e.g.* gold, carbon). It is also important for the surface area to be accurately measured and well defined. The *raison d'être* of the CE is to close the circuit when current flows from the WE and through the electrolyte. In terms of kinetics, it is important that the surface area of the CE be greater than that of the WE, so that the flow of electrons is not impeded. Platinum is a very common choice for CEs, as it is extremely chemically inert and will not react with the electrolyte. The reference electrode should have a very stable, well-known equilibrium potential, as it is against the RE that the real potential of the other two electrodes will be measured; as such, silver electrodes are a standard choice. Steps should be taken to ensure that the surface of the electrode is not oxidised when in use, and it is also essential that the RE does not react with the electrolyte within the electrochemical window of choice [117, 118].

The Gold/Mica SFB Three-Electrode Cell

The three-electrode cell used in the gold/mica SFB (as well as Au3 SFB), a diagram of which is shown in Fig. 3.9 (B), was custom-made to suit the restrictions of the SFB whilst adhering to the principles that define a reliable electrochemical cell, as outline in the previous section. In the gold/mica setup, the surface of the gold lens doubles up as a WE surface, as well as a mirror. A platinum wire is used as a CE and a silver wire serves as a RE, and both are bent to fit around the geometry of the boat and the cup in which the bottom lens is held along with the electrolyte. Simple wires were used instead of conventional electrodes to avoid the release of ions into the liquid medium.

The silver quasi-reference electrode is used because the silver is stable in IL and it avoid significant changes to the SFB apparatus. This setup was designed for measurements in IL, and the use of another type of RE would have required modifications to the SFB. The stability of the electrode is shown in the CVs in Chapter 4 in Fig. 4.2 and Fig. 4.8.

The gold surface is template-stripped right before loading into the boat, so it remains clean, water-free and atomically smooth. A gold wire is pinched down onto its surface with a custom-made Teflon screw and solid gold clamp, all of which are cleaned in chloroform, toluene, isopropanol and ethanol beforehand, to eliminate contaminants. The gold wire is sheathed in Teflon, and the ends are shaved off to expose the gold itself for the connections.

The platinum and silver wires are cleaned in chloroform, toluene, isopropanol and ethanol, and stored in ethanol until they are mounted onto the boat. When they are mounted, the CE and RE wires dip into the cup without touching the Teflon boat, to avoid mechanical coupling during the experiment. The open circuit potential is measured with a potentiostat after injecting the liquid to determine whether the cell is working. The ionic liquid used in this work was dried on a Schlenk line for at least twenty-four hours before injecting it between the lenses and filling the cup. After injection, the door of the chamber of the SFB was promptly closed and nitrogen gas was used to purge it for 20 min. In these experiments, water is considered to be an impurity, and these measures are important to avoid the ionic liquid or the surfaces of the electrodes becoming excessively wet. In the experiments with dilute KCl (aq), the mixtures were prepared with care not to contaminate the electrolyte solution.

3.3.5 Experimental Setup

The lenses are mounted in crossed-cylinder geometry, as in the classic setup. The bottom lens is the gold lens, and sits with its apex parallel to the length of the boat, mounted in a Teflon electrochemical cup that itself is mounted onto leaf springs. The counter-electrode and reference electrode are clamped so that they are immersed in the liquid in the cup without touching any of the surfaces, to avoid mechanical coupling or an electrical short-circuit. The gold wire of the working electrode has a loop on one end, through which a Teflon screw is threaded. The wired screw is then threaded through the eye of the gold clamp. This is screwed into the Teflon cup so that the clamp is in contact with the side of the gold lens and the wire is pinched between the head of the screw and the clamp. It is extremely important not to scratch or dirty the lens, especially its apex, during this process. The conductivity of the lens/electrode is then tested by connecting a multimeter to tweezers cleaned in nitric acid (2:1 water : nitric acid 70%) and pinching the other end of the old wire with one pair of tweezers, while very gently touching the tip of the other pair to the side of the lens, taking extreme precaution not to scratch or contaminate the surface.

The top lens is the silvered mica lens, the apex of which is set up to be perpendicular to the bottom lens. It is mounted onto a Teflon holder, itself mounted onto the piezoelectric tube and lateral leaf springs. When setting up the top lens holder, it is very important to check that the head of the screw used to tighten the top lens does not touch any of the wires of the electrochemical cell or the side of the electrochemical cup, as this will cause mechanical coupling.

A calibration measurement is made in air before injecting the liquid between the lenses, as in the classic setup.

3.3.6 Summary: Modifications to the Pre-existing Asymmetric Gold-Mica SFB

This version of the asymmetric SFB is based on previous versions of the EC–SFA described by other groups [23, 51, 52, 60, 119], and adapted for the SFB used in our lab. Some modifications were made based on our work on Au3 SFB, which is described in the next section; these improvements to the gold/mica setup can be summarised as follows:

- Improved gold lenses – Very slow deposition of gold on mica via physical vapour deposition, combined with spin coating of a controlled amount of EPON epoxy in ethyl acetate yield extremely smooth gold surfaces, which, when combined with a back-silvered mica surface, give excellent and reproducible sub-nanometric resolution ($\sim$ 0.1 nm), an example of which is shown in Fig. 3.10.

- Gold lens mounted on the bottom – In previous gold/mica setups, the gold lens is typically mounted on top [23, 52, 54, 58, 71]. In this setup, the gold lens is mounted on the bottom, in the electrochemical cup .

- Gold clamps – In the Au3 SFB originally described [45], the gold wires were soldered directly onto the surface of the lenses. This introduced an extremely delicate step as a mixture of carbon black and EPON epoxy was used to solder the wire, which significantly increased the risk of contaminating the liquid once it was injected. To cut out this risk, gold clamps and Teflon screws were fabricated to pin the wire to the lens (Fig. 3.6).

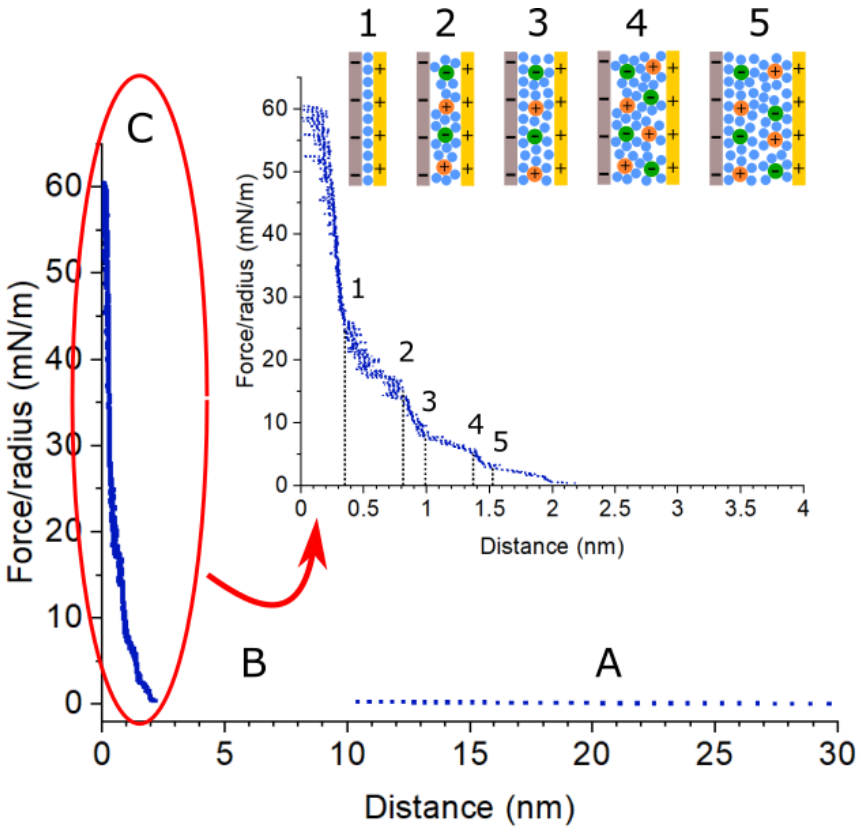


Figure 3.10: *Graph showing a force profile in KCl (aq) 0.6 mM measured at −300 mV with the gold/mica setup. Electrostatic repulsion is seen, which can be explained by the surfaces having the same sign potential. (A) Between 30 and 10 nm, a long-range force is observed, which is interpreted as the screening length, followed by a "jump-in" from 10 nm to 2 nm, where attractive van der Waals forces become dominant (B) [56, 146]. From 2 nm to 0 nm, a strong repulsion is seen (C). The inset shows a close-up of the repulsion region between 2 and 0 nm. Two different types of steps are observed: a larger step of about 0.4 nm and a smaller step of about 0.2 nm. The large step is more rapid, whereas the small step is more progressive, and requires an increase in force. These can be interpreted as structural forces in the electrolyte. The large steps can be interpreted as the expulsion of a hydrated ion; when the surfaces approach and the force between the surfaces reaches a maximum of the oscillatory force, a layer of ions is expelled from the slit. The small steps can be interpreted as the squeezing out of water molecules; the increase in force during these suggests that this is not a favourable process and that the water molecules are being squeezed within the slit before being expelled. The numbered cartoon illustrations propose a simplified interpretation of this process: (5) two hydrated ion layers, (4) compression and gradual expulsion of the equivalent of one layer of water molecules, (3) expulsion of a hydrated ion layer, (2) compression and gradual expulsion of equivalent of one layer of water molecules, (1) expulsion of a hydrated ion layer. The final water layer trapped between the surfaces is gradually squeezed out. It is likely that ions are strongly adsorbed on the surface, and the attractive force between the surfaces during the jump-in is not sufficient to extrude them. They are only expelled when driving the surfaces together.*

This version of the electrochemical gold/mica SFB improves on previous versions, and is the first time such an asymmetric gold/mica setup has been used in the Oxford group. Results obtained with it are presented in the following two chapters (Ch. 4 and 5) and demonstrate that the modifications significantly and reliably improve the performance of this asymmetric system. Thanks to these improvements, the gold/mica setup has become an important addition to the setups in use in this lab and is being used to pursue new measurements.

3.4 The Triple Gold Mirror Surface Force Balance

3.4.1 Introduction

The Triple Gold Mirror SFB setup (SFB Au3) is a symmetric setup which uses two potential-controlled gold surfaces, as proposed by van Engers *et al.* [45] in 2018. It resolves the issues that had hindered previous attempts at a symmetric gold setup, namely loss of resolution due to the absence of a spacer, loss of optical information and roughness of the surfaces, all of which equally resulted in experimental hurdles and difficult analysis. The Au3 setup also doesn't require any major modifications to the conventional SFB, unlike the Kurihara symmetric setups [46, 47].

Since the inception of SFB as a technique, there have been many attempts to use one (asymmetric) or two (symmetric) metallic/conductive surfaces to measure forces across air or liquids [23, 45–47, 49–54, 58, 62, 71, 72, 116, 120]. It remains a challenging field and there is much to be done both on a technical and experimental level to elevate symmetric electrochemical SFB setups. In this section the history of these setups will be briefly discussed before describing the one used for the results reported in Ch. 6. The history of asymmetric setups was discussed in the previous section; however, as stated there, the development

of symmetric and asymmetric setups are intertwined and cannot be regarded as completely separate from each other, and it is worth considering them together when discussing advances in electrochemical SFB.

Kasuya and Kurihara proposed a symmetric SFA for opaque samples [47], where twin-path interferometry [46] is used to measure forces between hard surfaces by shining a laser light through the stack and measuring the light reflected on the back of the lower surface. Using this technique, they also developed a symmetric gold/gold electrochemical setup (EC SFA) using template-stripping to prepare the surfaces [47] and, a few years later, a symmetric platinum/platinum EC SFA [49]. In these setups, surface force measurements were made in dilute electrolyte, with and without potential control, as well as some electrochemical measurements such as cyclic voltammograms. The resolution of the twin-path interferometry technique was reported to be 0.2 nm, but it required significant modification to the apparatus and thus cannot easily be directly implemented in other SFAs. Another drawback of this twin-path interferometry model is that there is no direct measuring of the distance between the surfaces, nor of the integrity of the surface, as the light does not pass through the medium and the liquid. This can be a source of problems, as with metal surfaces it is sometimes the case that the surfaces at the contact spot are changed due to cold welding or damaged from the repeated stress of multiple iterations of bringing the surfaces together.

A symmetric graphene SFB (gSFB) was proposed by Britton *et al.* in 2014 [120], using chemical vapour deposited graphene on mica to create ultra-smooth (0.19 nm RMS) surfaces and classic multiple beam interferometry (MBI). This setup allowed for potential control, but also presented considerable technical difficulties, making its use very challenging. The synthesis of a single layer of graphene requires expertise in furnace-grown graphene preparation and access to specialist equipment, and the transfer of the single layer to the lenses necessitates great skill, which takes time to develop. In the case of Britton *et al.*, there

was reliance on a third-party collaborator, which made the fabrication slow and complicated.

In 1994 Levins and Vanderlick [62] proposed a 3-mirror symmetric gold setup where one lens was coated in template-stripped gold and the other in doubly mirrored mica. However, the gold on the latter had to be deposited directly, resulting in an RMS (root mean square) roughness of $>$1 nm, which is too high for surface force measurements at small length scales.

The 2018 van Engers *et al.* variation on the 3-mirror setup involves template-stripping both outer gold layers, yielding ultra-smooth surfaces that can also be used as electrodes [45]. As the RMS roughness of the surfaces is $\sim$ 0.2 nm [60, 121], this technique is suitable for small length scales, as the roughness is of the scale of individual molecules and shorter than the range of typical intermolecular and surface forces measured in SFB.

In 2021, Valtiner *et al.* described a new symmetric gold SFB setup that uses mica as a spacer instead of glue [122] and includes an electrochemical cell designed for bilayer transfers. Additionally, this setup is modified to fully decouple the interferometric distance determination from force sensing. It uses a three-mirror interference pattern to determine the separation of the surfaces.

3.4.2 The Triple-Gold Mirror Setup

Fig. 3.11 (a) depicts the Au3 SFB. The interferometer is bounded by the gold mirrors Au1, Au2 and Au3. Au3 is deposited onto a thin adhesion layer of chromium (2 nm) on the surface of the lens by physical vapour deposition (PVD) and has roughness $>$1 nm. Au1 and Au2, the gold surfaces which are in contact with the medium, are template-stripped and glued onto the lenses with epoxy. The roughness of the template-stripped gold surfaces is about 0.2 nm

[45]. Although this is much rougher than the RMS roughness of mica (0.034 nm), it is significantly less than vacuum-deposited gold and it is suitable for surface force measurements at small length scales. The cylindrical lenses are set up with cross-cylindrical geometry, as with the setups described in sections 3.2. and 3.3..

The template-stripped gold surfaces Au2 and Au3 fulfil the three purposes: mirrors, confining surfaces and working electrodes. This means that there are no spacers between the surfaces and the mirrors, unlike in classic SFB, where the mica surface acts as a spacer between the silver mirrors. In Au3 SFB, to be able to measure distances smaller than the diffraction limit of visible light, which is about 250 nm [123], there needs to be a third mirror: Au1. The epoxy layer between Au1 and Au2 serves as a spacer and thus it is possible to have resolution below the diffraction limit of visible light.

Light is shined from the bottom of the stack, and the light that interferes constructively between the mirrors emerges as an interference pattern made up of three different types of FECO patterns corresponding to three different types of reflections (*cf.* Fig. 3.11). Primary fringes ($P(D)$) occur as a result of reflections between Au2 and Au3, and thus are distance-dependent. They appear as arcs in the interferogram and move when the distance between the lenses (D) changes. Secondary fringes (S) are a result of reflections between Au1 and Au2, the wavelength of which corresponds to the epoxy layer $Z1$ on the double-coated lens. As a consequence, they are distance-independent and the fringes appear in the interferogram as fixed bands of light. Tertiary fringes ($T(D)$) arise from reflections between Au1 and Au3, and are consequentially distance-dependent. The lenses used for Au3 SFB are refractive index-matched to the EPON epoxy glue, as if they have different refractive indices, it introduces another type of reflection (EPON/lens interface). By index-matching the two, it avoids adding the fit of these reflections to the already optically complex analysis.

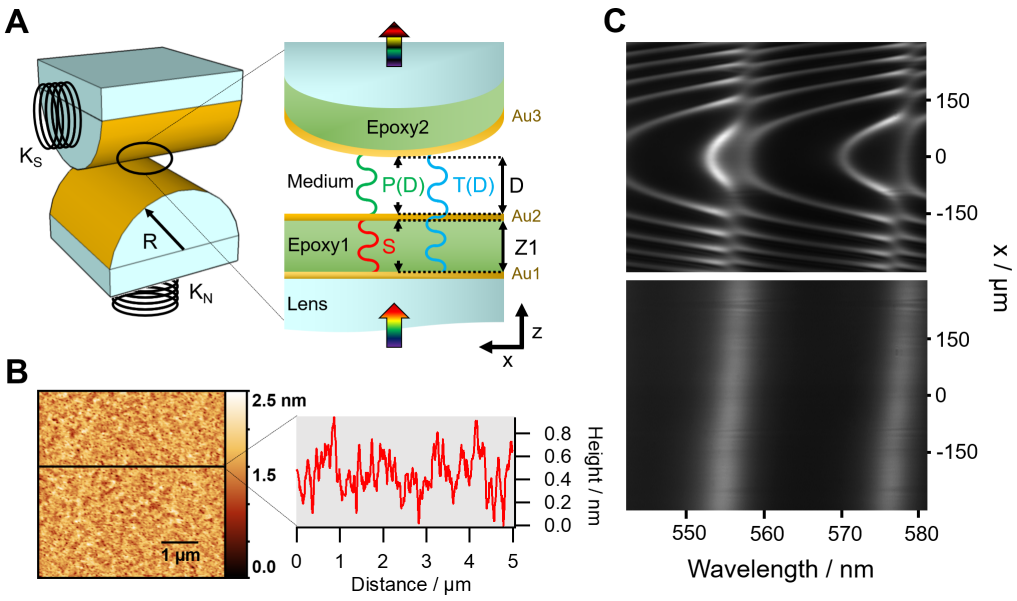


Figure 3.11: *(A) Diagram illustrating the triple gold mirror SFB setup. As with the conventional SFB, crossed-cylindrical geometry, equivalent to a sphere on a flat surface, is used, and normal and lateral forces can be measured by the displacement of the springs with force constants K_N and K_L respectively. Light is shined through the stack and an interference pattern emerges as a result of constructive interference between the mirrors. Primary fringes ($P(D)$) arise from reflections through the medium between Au2 and Au3 , the surface layers, and thus depend on distance D. Secondary fringes (S) result from reflections between Au1 and Au2, which are separated by the epoxy layer of thickness Z_1 and are therefore distance-independent. Tertiary fringes ($T(D)$) arise from reflections between Au1 and Au3,and are also distance-dependent.(B) A CM–AFM height map shows the RMS roughness of the template-stripped gold, which is 0.23 nm. (C) (Upper) Typical experimental interferogram. The primary fringes are seen as curved arcs, whereas the secondary fringes appear as vertical bands, which do not move. The primary fringes move depending on variations of D, and the apex corresponds to the point of closest approach. Tertiary fringes cannot be seen, but they cause blueshift. (Lower) Experimental interferogram showing the secondaries without the primaries; the greater the distance between secondaries, the thinner the epoxy thickness Z_1. Figure from van Engers et al. [45].*

However, they don't appear as fringes in the interferogram and only cause blueshift, which is a decrease in the wavelength of the light. This is due to the intensity of the tertiary fringes $I_{T(D)}$ being a product of two more transmissions through mirrors than that of the primary $I_{P(D)}$ or secondary I_S fringes. In other words, the light path of the tertiary fringes goes through the Au-Epoxy and the Au-medium interfaces, whereas the path of the primaries just goes through Au-

Medium, and the path of the secondaries through Au-Epoxy. This is rationalised in previous work by van Engers *et al.* [45] and overviewed in the next section.

Two experimental interferogram are shown in Fig. 3.11(C). Both are images taken at large separation, but the top one is taken with the surfaces at rest (D is not changing), so the primary fringes appear clearly as arcs. The secondary fringes appear as near-vertical bands of light. The bottom image was taken while the surfaces were moving away from each other at speed, blurring out the distance-dependent interferences ($P(D)$) while the distance-independent fringes (S) remain static. This type of image, once analysed, gives the thickness of the epoxy spacer.

It is essential for the epoxy layer $Epoxy1$ to be of uniform thickness, so that in the region of closest approach the thickness is uniform. This is so the contact area is flat, ensuring a single point of contact, and so the secondary fringes are as smooth as possible. If the epoxy is too uneven, there will be multiple points of contact, which makes a force measurement impossible. If the epoxy is moderately uneven in the area of closest approach, the S fringes are very irregular and make the analysis more complicated, as it is difficult to determine exactly what the thickness of the glue is, and thus what $D = 0$ is. The secondaries are also more vertical when the glue is uniform. The alignment of the secondaries can be optimised by rotating the top lens about the vertical axis, but it is preferable not to have to do this, as it means departing from the crossed geometry of the hemicylinders. Additionally, it presents a risk of the electrode wires moving and coupling mechanically to the cup or being shorted on the stainless steel boat (*cf.* Fig. 3.13). Irregular or off-vertical secondaries complicate the analysis of the interferogram to the point where it can become impossible.

Due to the presence of three mirrors, the exact thickness of each will strongly influence the character of the interference pattern. As demonstrated in previous work [45], the effect of the tertiary fringes is exacerbated by an increase

in the transmission through Au-Epoxy and Au-Medium. This means that when Au2 is thin, blueshift is more pronounced, and when it is thick, its effect is negligible. However, optimising resolution requires careful weighting of each factor (the three Au thicknesses and the epoxy thickness), as increasing the thickness of the gold will result in a loss of transmittance that will be all the more exacerbated by the presence of three mirrors (as opposed to two in classic SFB), while decreasing the thickness of the gold layer will eventually compromise the integrity and smoothness of the surface. The minimal achievable thickness for a gold mirror to be uniform, atomically smooth and "stripable" without damaging it is about 20 nm. Spectral resolution is at its best when Au1 and Au3 are "thick" (30 – 40nm), Au2 is "thin" (20 – 25 nm) and the epoxy layer $Z1$ is as thin as possible whilst still being bigger than the diffraction limit of light, which corresponds to a $Z1$ thickness of 4 – 5 μm.

In the Au3 SFB, the tracking of the secondaries is used to calculate the distance between the surface. Due to the interferometer's configuration, as the surfaces come closer together, the primary fringes evolve so that it is no longer possible to track the apex of the p fringe. Instead, the change in intensity of the secondary fringes is used to calculate the distance. As a result, it is more accurate to fit the whole interference spectrum, as opposed to fitting the peak positions, which is the method used in conventional SFB [61].

3.4.3 Fabrication of the Lenses

The fabrication of the lenses was learned from Dr. Marco Balabajew and Dr. Christian van Engers, who had the idea for the technique [45]. Marco and I refined the fabrication process and performed the proof-of-concept measurements in liquid in 2017. During my own independent work on the asymmetric gold-mica setup, I performed further modification to the fabrication process, mostly in the

thickness and smoothness of the glue and gold layers. Gold clamps were also introduced to avoid soldering, a change which significantly decreased the risk of contamination of the experiment by eliminating the carbon black/EPON mixture used as solder.

As with all SFB operations, it is imperative that all tools and materials be extremely clean and particle-free. All glassware and the lenses are cleaned in piranha solution (3:1 concentrated sulfuric acid : hydrogen peroxide 30%), and tools are cleaned in aqueous nitric acid (2:1 concentrated nitric acid : water) unless indicated otherwise. The water used in all steps is cleaned by a Milli-Q® IQ 7003 purification system, which provides deionised water with less than 2 ppb total organic content (TOC).

Before starting, it is necessary to distinguish the two lenses since they are prepared slightly differently, as illustrated by Fig. 3.12. Both are hemi-cylindrical NBaLF–5 lenses (radius of curvature = 1 cm); one has double gold mirrors and will be called $lensD$ (Fig. 3.12 (D)), the other has a single mirror and is referred to as $lensS$ (Fig. 3.12 (C)). $LensD$ is mounted into the electrochemical cup, itself mounted onto the springs in the boat, which sits on the bottom in the SFB, whereas $lensS$, the top lens, is placed in a holder mounted onto a sectored piezoelectric tube. The single-coated lens $lensS$ is made in the same way as the one used in gold/mica, except that the thickness of the gold layer is 25 nm, so we refer to section 3.3.3. for the method of fabrication of $lensS$.

Preparing *lensD*

The first gold mirror on $lensD$ is deposited by thermal evaporation (Edwards Auto 306 Cryo Evaporator). The lens is first coated with 2 nm of chromium, as gold does not adhere readily to quartz, and the gold (35 nm) is then evaporated onto it. This is particularly useful because it allows the bottom mirror $Au1$

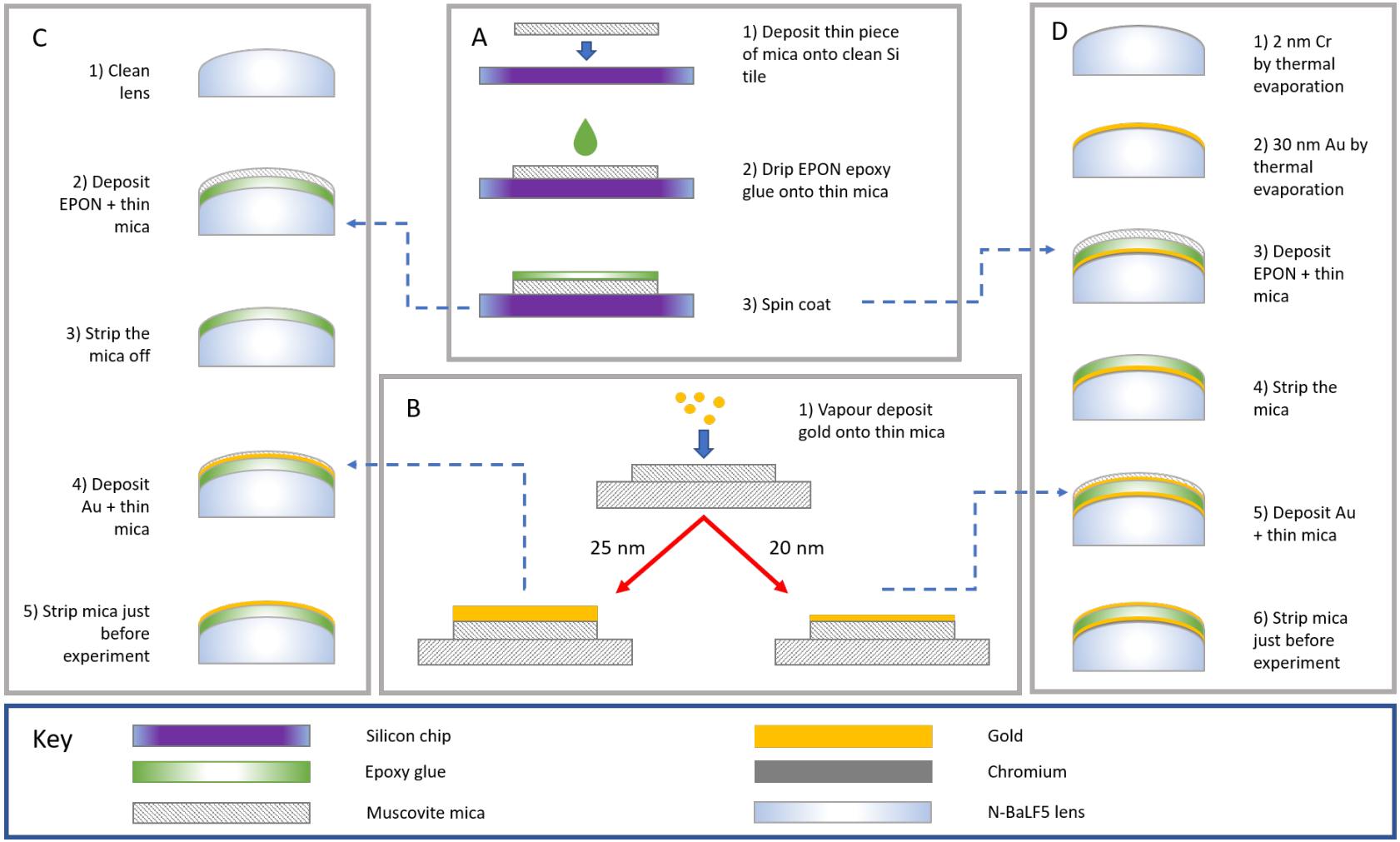


Figure 3.12: *Diagram illustrating the different steps of the fabrication process of the gold-coated lenses. (A) The spin coating process. (B) Vapour-depositing gold on thin mica for template-stripping. (C) Fabrication of* $lensS$*. D. Fabrication of* $lensD$*.*

to be reused several times, as it can be cleaned in piranha and cycled through several experiments. Both $lensD$ and $lensS$ are cleaned in piranha before the template-stripped gold mirrors can be applied.

Spin-Coated EPON

This step is identical for both lenses, and it is the same process as the one used to fabricate the gold lens in the gold/mica setup, so we refer to section 3.3.3. for the fabrication methods. As this methodology yields ultra-smooth glue over large areas, it can be assumed that $Z1$ has a uniform thickness at the point of closest approach. In a force measurement, the lenses are assumed to be aligned perfectly orthogonally to each other but in practice, there are small mechanical and optical factors that can create a minute lateral travel during approaches from large distances ($>$100 nm) to contact ($\sim$ 0 nm). While it is important to consider the impact of this on the calculation of D, the estimated thickness variation of the glue layer is less than 0.2 nm, which has negligible effect on D.

Template-Stripped Gold

The two lenses have template-stripped gold mirrors, but of different thicknesses; as shown in Fig. 3.12, $lensS$ is coated with 30 nm of gold, whereas $lensD$ is coated with 25 nm gold. The fabrication method is the same as in section 3.3.3., so we refer to that for methods. The top layer of mica, which protects the surface of the gold, is only removed right before an experiment.

3.5 The Three-Electrode SFB Cell

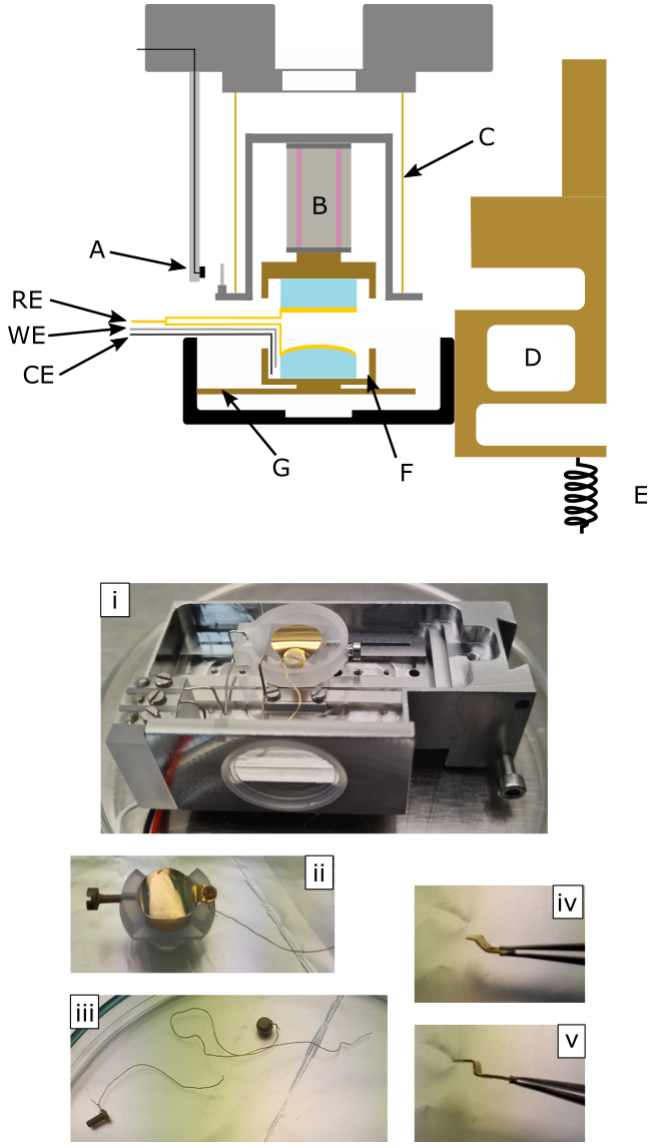


Figure 3.13: *Top: Diagram showing the inside of the SFB with the Au3 electrochemical setup, with (A) the capacitance probe, (B) the piezoelectric tube, (C) the lateral leaf springs, (D) the stiff spring, (E) the helical spring, (F) the electrochemical cup, (G) the normal leaf spring, (WE) the gold working electrode and wire, (RE) the silver pseudo-reference electrode and (CE) the platinum counter-electrode. Bottom: (i) Bottom lens* $(lensD)$ *mounted in the electrochemical cell of the boat and connected by gold wire and clamp. The platinum CE and silver WE are also connected, and do not touch the side of the cup. The electrode connector on the left holds the CE, RE and WE wires in place. (ii) Top lens* $(lensS)$ *mounted in the Teflon cup, which is mounted onto the piezoelectric tube during experiments. (iii) Wires, clamps and screws for both lenses. (iv) Gold clamp for* $lensS$*. (v) Gold clamp for* $lensD$*.*

The electrochemical cell used in Au3 SFB is the same as in gold/mica SFB, except that the top lens is also connected to the potentiostat via a wire and a clamp screwed into contact with the gold surface, as shown in Fig. 3.13. This means that the top and bottom lens are identical working electrodes, and the reference and counter-electrodes are the same as in gold/mica SFB. A detailed description of this cell is included in the section 3.3.4.

3.6 Conclusion

This chapter presents the principles of the surface force balance, and presents two novel electrochemical methods. The gold/mica SFB (section 3.3.)is based on previous works, and improvements to the fabrication method of the gold lens result in excellent resolution. Layers in IL and dilute aqueous electrolyte have been measured with this setup, demonstrating that the improved fabrication reliably gives resolution of 0.1 nm. To our knowledge, this level of resolution is previously unseen in other gold/mica setups. Results obtained with this setup are reported and discussed in Ch. 4 and 5.

The Au3 SFB is a novel three-mirror setup that gives symmetric electrical potential control of both surfaces. The fabrication methods and experimental setup are described in section 3.4 and the measurements obtained with this setup are presented in Ch. 6. These are the first measurements made with Au3 SFB, and the advantages and drawbacks of this setup are discussed in detail in the conclusion of Ch. 6.

Chapter 4

Results from the Gold/Mica SFB Setup: Underscreening

4.1 Introduction

As described earlier, Debye-Hückel theory only applies in dilute electrolytes, so it follows that a new approach must be adopted when trying to understand the behaviour of concentrated electrolytes. At high ion concentrations, these liquids diverge significantly from what is expected by mean-field theory, exhibiting long-range screening lengths [22–25, 124]. Some theoretical and computational work has been done to explain these experimental results, but their origin remains open [15, 17–19, 94, 99, 125, 126].

As detailed in Ch. 2, Lee *et al.* proposed that underscreening is a property of the liquid [22]. However, the experiments performed by them were done with a classic SFB setup, where the surface charge of the mica surfaces can neither be monitored nor controlled accurately, so the effect of surface charge could not be determined.

With the gold/mica SFB, it is possible to apply potentials to the electrode surface and record the resulting current, which means that the relationship of both of these with forces in the liquid can be investigated. The results reported in this chapter describe this, along with results from control experiments in dilute electrolytes, which lead to interesting observations.

4.2 Materials and Methods

The gold/mica setup was prepared as described in the previous chapter. All glassware was cleaned in piranha solution (3:1 concentrated sulfuric acid 99% : hydrogen peroxide 30%) and all stainless steel tools and parts were cleaned in nitric acid (2:1 water : nitric acid 70%). The syringe used for injecting the liquid between the lenses, the electrode wires, the clamps and the screws were cleaned by sonicating sequentially in chloroform (twice), toluene, isopropanol and ethanol.

The IL used in the experiments reported below was 1-butyl-1-methyl-pyrrolidinium bis(trifluoromethanesulfonyl)imide (C_4C_1pyrr TFSI). It was dried on a Schlenk line overnight (5×10^{-3} mbar, 60° C) and experiments were performed under nitrogen atmosphere, with P_2O_5 in the chamber to remove any remaining atmospheric water. For the experiments in dilute electrolyte, the solution was prepared on the day of the experiment in glassware that was cleaned in piranha solution immediately beforehand. The dimensions of these ions are presented in Tab. 4.1.

Table 4.1: *Diameters of a water molecule [127, 128] and of ions in C_4C_1pyrr TFSI [2, 22, 25–27, 129] and KCl (aq) [130–134].*

Ion	Ion diameter [nm]
H_2O	0.275
C_4C_1pyrr TFSI	1.0
C_4C_1pyrr	0.55
TFSI	0.51
K^+ (hydrated)	0.66
Cl^- (hydrated)	0.57

4.3 Results and Discussion

4.3.1 Force Measurements in Ionic Liquid

Force profiles were measured in pure C_4C_1pyrr TFSI, and a range of potentials within the electrochemical window were applied to the WE to determine whether applied potential has an effect on the screening length. Approaches were made with the piezoelectric tube at approximately 0.5 nms^{-1}. Like many ionic liquids, C_4C_1pyrr TFSI has a very wide electrochemical window of 5.8 V [135], where no electrochemistry or irreversible chemical changes are occurring on the surface of the working electrode. Each measurement was taken well within this window after changing surface potential and letting the current settle for 10 min. This wait-time was chosen empirically, by observing how long it took for the current to reach equilibrium after changing the applied potential. Cyclic voltammograms (CVs) of C_4C_1pyrr TFSI are shown in Fig. 4.2, and CVs of KCl (aq) 1.5 mM and 0.6 mM are shown in Fig. 4.8.

Fig. 4.3 and 4.4 show force profiles in C_4C_1pyrr TFSI, taken at a range of applied surface potentials, by plotting the measured force F divided by the radius of curvature of the lens R on a log scale versus distance. The force profiles in Fig. 4.3 were all measured in the same experiment, and the force profiles in Fig. 4.4 were all taken on a different day, in a different experiment with another set of lenses and sample of the same IL. In total, seven separate experiments were successful, and examples of force profiles from these other experiments are included in the Appendix. In most experiments, repeats of force profiles at the same applied potential were measured, and these can also be

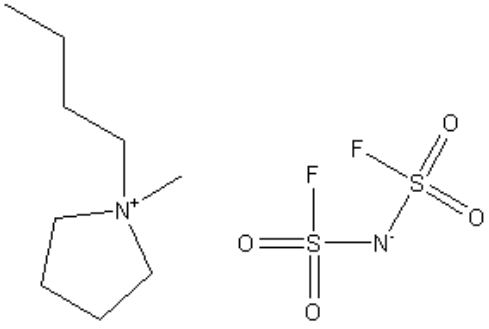


Figure 4.1: *Molecular structure of C_4C_1pyrr TFSI.*

found in the Appendix.

In each force profile of Fig. 4.3 and 4.4, a long-range decaying tail appears in the 6 – 20 nm region and steps are observed in the 2 – 6 nm range. The surfaces do not come into contact at 0 nm, but reach a “hard wall” at approximately 2 nm, beyond which no further approach is possible, even when applying high pressure with the piezoelectric tube or the motor. No change in the magnitude of the forces is observed when varying surface potential, and there is no change in screening length with applied potentials.

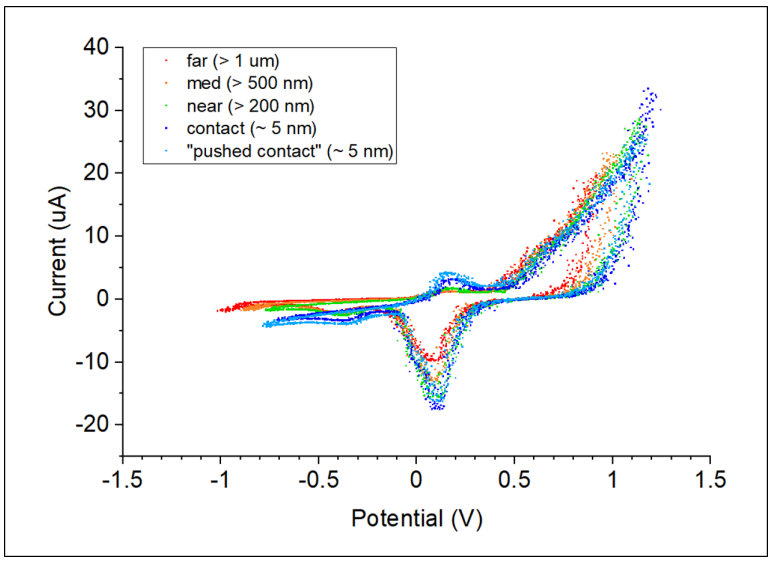


Figure 4.2: *Cyclic voltammograms of C_4C_1pyrr TFSI measured at different separations of the surfaces in Au3 SFB. The separations at which the CVs were measured were: >1 μm (red), $>$500 nm (orange), $>$200 nm (green), $\sim$ 5 nm (light blue), which corresponds to the point at which the surfaces come into contact, and $\sim$ 5 nm (dark blue), which corresponds to driving the surfaces towards each other with the piezoelectric tube for a while after they come into contact. This was done to attempt to squeeze as much of the IL out from between the surfaces as possible. The potentials applied in the force profiles in Fig. 4.3 and 4.4 are all within the stable range.*

Underscreening

Tab. 4.2 and 4.3 indicate screening lengths measured by fitting the long-range tails of the profiles, which appear to decay exponentially. The measured

screening lengths range between 5.1 nm and 7.8 nm, which is a scatter that falls within expected error and shows that surface potential doesn't influence the measured apparent screening length.

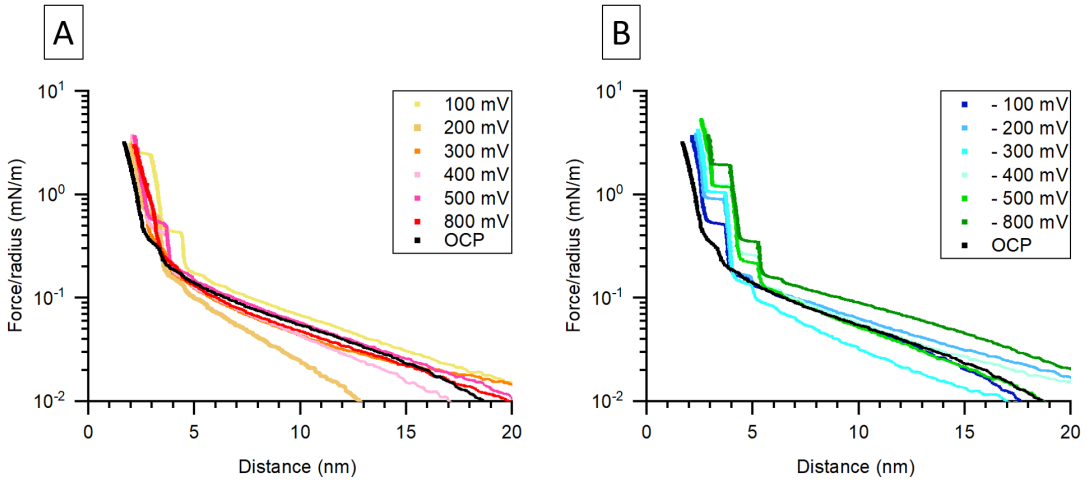


Figure 4.3: *Force profiles under potential control for C_4C_1pyrr TFSI, all measured within the same experiment, with (A) force profiles at positive potentials ranging between $+100$ and $+500$ mV, and at $+800$ mV, and (B) force profiles at negative potentials ranging between -100 and -500 mV, and at -800 mV. No change in screening length was observed when varying the surface potential of the gold lens. The long-range "tails" in the 6 – 20 nm region are exponential, and are interpreted as the electrostatic screening length. Structured layers were observed at shorter ranges ($\sim$ 2 – 6 nm), demonstrating the high resolution of this asymmetric gold/mica setup.*

Underscreening manifests in force profiles as a long-range decay length extending several nm from the point of closest approach. The screening length of C_4C_1pyrr TFSI has been reported in classic SFB experiments as about 6 – 8 nm [22]. As shown in Tab. 4.2 and Tab. 4.3, screening lengths for this IL at open circuit potential (OCP), where no potential is applied to the surface of the WE, and at applied potentials are all in good agreement with results from classic SFB.

As explored in Ch. 2 [21, 22], concentrated electrolytes do not follow Debye-Hückel theory, and a scaling law was proposed instead by Lee *et al.*:

$$\lambda_S \sim l_B c_{ion} a^3 \tag{4.1}$$

This empirical law proposes that the length scale of underscreening is solely de-

Table 4.2: *Measured screening length for the force measurements shown in Fig. 4.3.*

Screening Lengths – C4C1pyrr TFSI 100 – 800 mV range		
Applied potential	Screening length [nm]	Error [nm]
OCP	6.0	0.3
0 mV	5.5	0.3
100 mV	6.2	0.3
300 mV	5.7	0.3
400 mV	5.1	0.3
500 mV	5.9	0.3
800 mV	6.3	0.2
- 100 mV	5.6	0.3
- 200 mV	6.5	0.3
- 300 mV	5.0	0.2
- 400 mV	6.0	0.3
- 500 mV	5.5	0.3
- 800 mV	7.8	0.3

pendent on Bjerrum length l_B, concentration c_{ion} and ion size a. It also suggests that there are no other factors determining the screening length, including surface charge. However, the measurements on which this scaling law was based were performed in mica/mica, so the effect of surface charge could not be verified, as mica is an insulator. The results from the electrochemical measurements shown in Fig. 4.3 and 4.4, where surface potential was applied and charge was monitored, demonstrate that surface charge does not affect screening length, which provides proof that underscreening in independent of surface potential.

On the other hand, although DLVO theory does not predict a change in the decay length with changing potential, it does predict that surface potential should change the magnitude of the forces between surfaces, as the electrostatic contribution will be affected by the surface charge. It is therefore surprising that there is no discernable change in the magnitude of the forces measured in C_4C_1pyrr TFSI when potential is increased. One would expect there to be a change corresponding to the sign and magnitude of the applied potential, as the charged surfaces should attract (positive gold, negative mica) or repel each other (negative gold, negative mica) until the point of approach where van der Waals

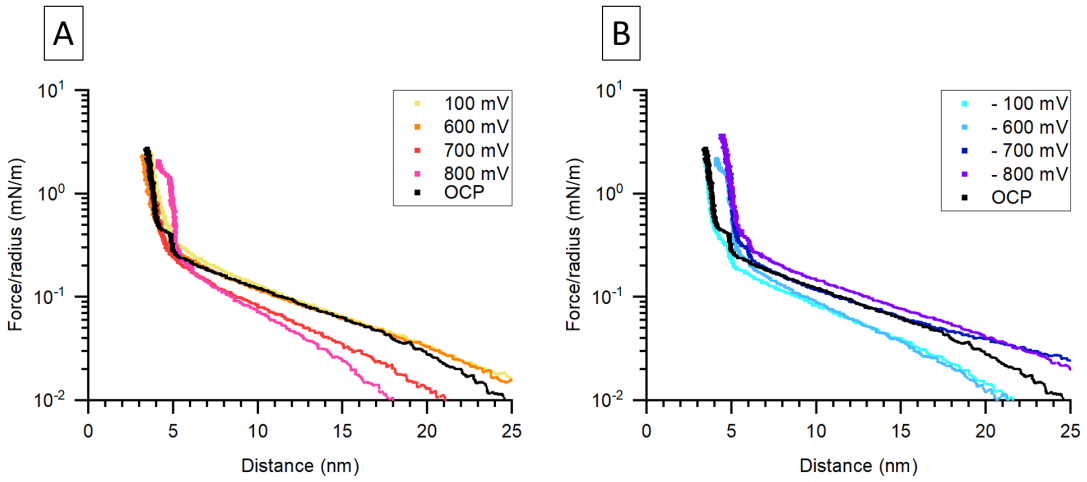


Figure 4.4: *Force profiles under potential control for C_4C_1pyrr TFSI, all measured within a single experiment, which is separate to the one which gave the force profiles in Fig. 4.3 with (A) force profiles at positive potentials ranging between +500 and +800 mV, and at +100 mV, and (B) force profiles at negative potentials ranging between −500 and −800 mV, and at −100 mV. The exponentially decaying long-range tail in the 6 – 20 nm range is interpreted as the electrostatic screening length, which does not change with applied potential. The steps in the 2 – 6 nm range indicate structured molecular layering. This level of resolution is reproducible across a majority of experiments thanks to the improved lens fabrication method described in Ch. 3.*

forces take over and result in adhesion. Interestingly, this is not the case here – magnitude does not scale with applied potential. This suggests that the applied potential is completely screened by the near-surface ion layers, and that the effective potential is independent of applied potentials as a result.

Capillary freezing

Additionally, in these measurements with C_4C_1pyrr TFSI it was observed that the surfaces do not come into contact at 0 nm. Instead the approach ends at a "wall" at about 2 nm separation across all clean experiments. This cannot be put down to inaccuracy, as in a contact-free calibration, as asymmetric measurements use contact calibration and error in this determination is usually of the order of 1 nm. In all measurements involving C_4C_1pyrr TFSI, this wall was observed and it was not possible to squeeze out the last few layers of ions, even

Table 4.3: *Measured screening length for the force measurements shown in Fig. 4.4. These were made on a different day to the ones in Fig. 4.3 and show similar screening lengths.*

Screening Lengths – C4C1pyrr TFSI 600 – 800 mV range		
Applied potential	Screening length [nm]	Error [nm]
OCP	7.2	0.5
0 mV	6.4	0.5
100 mV	7.1	0.5
600 mV	7.1	0.6
700 mV	5.6	0.5
800 mV	7.0	0.5
- 100 mV	6.3	0.4
- 600 mV	5.5	0.6
- 700 mV	7.4	0.5
- 800 mV	7.6	0.5

when driving the surfaces together to high levels of applied pressure, textwhich suggests the ions are more strongly adsorbed on the surface than the force we can apply with the SFB. This observation was also true at a separation of ~ 5 nm in Au3 SFB, as will be discussed in Ch. 6. There is no discontinuity in the fringe position during these measurements.

At this stage, it is important to verify that this wall is not due to contamination of the experiment. In classic SFB, a contaminated experiment will typically not come into contact at 0 nm, but there are other telltale signs. If there are large-scale contaminants, approach to distances smaller than 100 nm is usually not be possible, and even for small molecular contamination, approach to distances smaller than 10 nm is generally not possible. Additionally, molecular layering is not seen in a contaminated experiment due to disruption to the layers, and one might also expect a contaminated experiment to show anomalous long-range forces or cyclic voltammograms, depending on the type of contamination. However, the results presented here show clear evidence of layering in the "steps" between 2 – 6 nm and CVs were normal. These measurements were repeatable across numerous experiments, and the "hard wall" was present in all clean experiments.

This raised the necessity to determine whether there was a problem with the setup, or if this was in fact a consequence of intermolecular and surface behaviour. Control measurements were made in dilute potassium chloride in water (KCl (aq)). Anticipating on the results from the dilute KCl (aq) measurements (*cf.* Section 5.3.2), the electrochemical cell was shown to work well and surfaces came into contact at 0 nm, which means that the non-zero contact in C_4C_1pyrr TFSI is a result of the liquid interacting with the solid at the interface (*e.g.* adsorption, capillary freezing...). The rest of the results from the dilute electrolyte experiments are discussed later in this chapter, but first the implications of these control experiments on the IL results are discussed.

There is no change in magnitude of the force between the surfaces with varying potential, and a “hard wall” at a separation of about 2 nm, which corresponds to about 2 bilayers. The wall is found on every approach, regardless of surface potential, so the EDL and the interfacial behaviour need to be considered anew to explain these phenomena.

The EDL consists of a layer of counterions forming on an oppositely charged surface. In dilute electrolytes, the concentration of co-ions (oppositely charged to the counterions) increases away from the Stern layer. In ionic liquid, bilayers are formed on charged surfaces in order to maintain electroneutrality. In 2013, Gebbie *et al.* reported force measurements in a similar asymmetric setup with another ionic liquid, where the applied potential had a clear effect on the force profiles of mica vs gold on approach [23]. A long-ranged electrostatic force between the surfaces, now interpretable as underscreening, was reported with the observation that its decay length was not changed by modifying surface potential, whereas the magnitude of the force scaled with the magnitude of the applied potential. The surface charge was shown to be only partially screened by the Stern layer (or inner Helmholz plane), resulting in a “residual potential” being felt away from the WE.

However, in the measurements reported here, applied potential has no effect on the magnitude of the decay length. Two approaches may be used to explain this:

1. Stern layer

   The first follows the interpretation of Gebbie *et al.* [23], where the Stern layer and diffuse double-layer formed in response to the applied potential mask surface charge. In our measurements, this suggests that the two bilayers confined between the surfaces when the "hard wall" at 2 nm is reached are sufficient to screen applied potentials between $+$800 and $-$800 mV, and so tightly bound to the gold surface that they cannot be squeezed out of the slit.

2. Capillary freezing

   The second possibility is capillary freezing, which was described in 2017 by Comtet *et al.* [136] as a phenomenon wherein an ionic liquid confined between metallic confining substrates exhibit a solid-like response beyond critical confinement $D = \lambda_S$. In this work this critical confinement will be referred to as λ_C to avoid confusion with the terminology used in underscreening. The characteristics of capillary freezing are a strong elastic repulsive response which occurs at $D >$0 and a solid-like response that can withstand high applied pressure and is repeatable. Repulsive forces are apparent in all force profiles seen in Fig. 4.3 and 4.4, and the "hard wall" does exhibit solid-like properties, being impossible to squeeze out. The force required to move the surfaces apart after arriving at the wall is more akin to forces required to separate solid surfaces than to those observed when separating surfaces across a liquid barrier. Fig. 4.5 shows a plot of F/R vs distance while driving the surfaces away from each other at constant velocity. The minimum of each trace shows the force required to separate the surface from contact at the "hard wall" in mN/m. Valtiner *et al.* measured the ad-

hesion force between mica and gold in 10 mM HNO_3 in an electrochemical SFB setup [52], and found that the surfaces jumped out of contact around 1 mN/m. In the IL experiments reported here, despite the surfaces not coming directly into contact because of the "hard wall", the jump-out F/R is between -3 and -6 mN/m, as seen in Fig. 4.5. By comparison, the force required to separate a Si_3N_4 AFM tip from contact at 0 nm with a mica surface in the same IL was measured at -4 mN/m [24]. The force measured to separate two mica surfaces in contact in SFB, with the same IL, was between -2 and -4 mN/m. This means the force required to separate the gold/mica surfaces at the "hard wall" is similar to the one required to separate other surfaces in adhesive contact across the same liquid. The higher higher force occurs despite the surfaces not being in adhesive contact, and suggests that the "hard wall" exhibits solid-like behaviour.

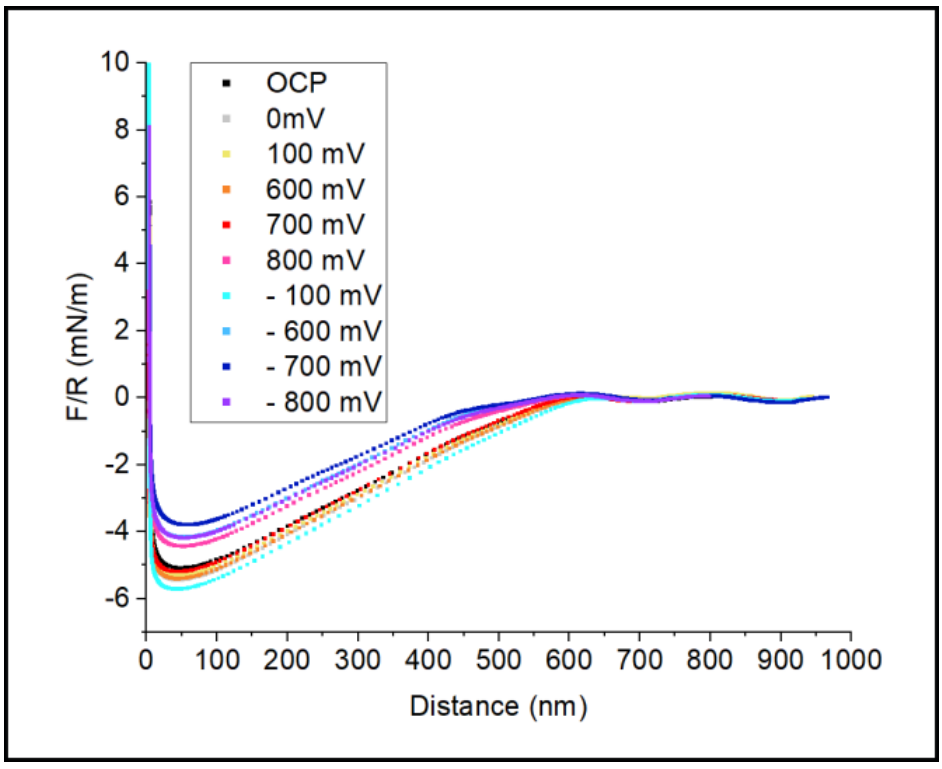


Figure 4.5: *Force measured while separating the surfaces at different applied potential. There is no apparent effect of applied potential on the force required to jump out from contact. The force required to separate the surfaces varies between -3 and -6 mN/m.*

The "hard wall" at 2 – 4 nm and adhesion force are observed across all

applied voltages and OCP measurements, which suggests that the surface potential of the gold surface has no effect on λ_C.

A shift in phase transition can be defined with the Gibbs-Thompson equation:

$$\Delta T = T_C - T_B = 2\frac{T_B \Delta\gamma}{\rho L_h \lambda_C} \tag{4.2}$$

Where ΔT is the change in transition temperature, T_C is the transition temperature in confinement, T_B is the transition temperature in bulk, ρ is the density of the liquid, L_h (also known as ΔH°_{fus}) is the latent heat of fusion and $\Delta\gamma = \gamma_{wl} - \gamma_{ws}$ with γ_{wl} is the surface energy of the liquid phase with the substrate and γ_{ws} is the surface energy of the solid phase with the substrate. The latent heat of fusion can be calculated from:

$$\ln x_2 = -\frac{\Delta H^\circ_{fus}}{R}(\frac{1}{T} - \frac{1}{T_{fus}}) \tag{4.3}$$

Which can be reordered to:

$$\Delta H^\circ_{fus} = -\frac{R \ln x_2}{(\frac{1}{T} - \frac{1}{T_{fus}})} \tag{4.4}$$

Where R is the gas constant, x_2 is the mole fraction, T is the atmospheric temperature, T_{fus} is the temperature of fusion. For C_4C_1pyrr TFSI, this gives us:

$$\Delta H^\circ_{fus} = -\frac{8.314 \times \ln x_2}{(\frac{1}{298.15} - \frac{1}{267.15})} = -214.91 \ \ Jmol^{-1} \tag{4.5}$$

Which gives us $L_h = 508.8$ Jkg^{-1}. $\Delta\gamma$ is not known for C_4C_1pyrr TFSI, as solid-solid phases are not studied commonly in ionic liquids. No literature values could be found for γ_{ws}, but γ_{wl} was measured by Carvalho *et al.* as $\gamma_{wl} = 34.93$ mNm^{-1} [137]. If we assume γ_{ws} is smaller than that and that $\Delta\gamma$ is of the order of 10^{-4} – 10^{-5} Nm^{-1}, this gives us 270.9 K$<$T$_C<$304.64 K, i.e. -2° C$<$T$_C<$30.85° C, which means that capillary freezing would occur when approaching the surfaces to λ_C. To verify this, γ_{ws} it would need to be

measured empirically or computationally.

The "hard wall" observed in all force profiles of C_4C_1pyrr TFSI exhibits a behaviour similar to capillary freezing as reported by Comtet *et al.* [136] and Schlaich *et al.* [20]. Our qualitative reasoning shows that it is indeed plausible. The λ_C value for C_4C_1pyrr TFSI falls in a sensible range and distinct solid-like behaviour is observed for every iteration of approaches. It is also noteworthy that the growth of multilayers of ILs on Au (111) has been seen in ultra-high vacuum [138]. Electrochemical microcalorimetry has shown that the EDL in C_4C_1pyrr TFSI charges slowly due to strong rearrangement of the ions in the EDL, and that the strong restriction of the ions in the EDL explain the unusually high partial molar entropy of formation of the EDL. Strong electrostriction effect were found in the EDL, with immobilisation of ions increasing with increasing strength of the electric field [3]. To verify if capillary freezing is being observed in nanoconfinement, it would be necessary to measure the friction between the surfaces while approaching them. If there is a solid-like response, we would expect a stick-slip profile when the surfaces reach critical separation.

It should also be noted that exact composition of the ionic liquid might affect whether or not capillary freezing is observed in a given system, as the steric and thermodynamic properties of ILs vary substantially depending on the ions used. This would affect the response to confinement between metallic surfaces, and further investigation into this phenomenon would benefit from determining what properties of the IL are important in inducing capillary freezing. Additionally, in the measurements reported here it is not possible to confirm whether the solid-like layer of ionic liquid present on the surface at all separations, or if it is confinement-induced, and further measurements would be necessary to determine this.

Structural Forces

In the 2 – 8 nm range, oscillatory behaviour due to structural forces was observed. The layers when coming close to contact in Fig. 4.3 and 4.4 are of a thickness of about 1.1 nm , which is in accordance with previously measured bilayers in C_4C_1pyrr TFSI between mica surfaces or between an AFM Si_3N_4 tip and mica [2, 22, 25, 26]. To the best of our knowledge, this level of resolution has not previously been reported in gold/mica SFB, which speaks to the excellent resolution of this setup. The fabrication method for the gold lenses very reliably allows for this level of resolution, which demonstrates that this method is very effective at producing highly reproducible high-resolution measurement in gold/mica experiments with ionic liquids, and can even be used with other liquids with smaller ion diameters exhibiting structural forces, as discussed in the next sections.

4.3.2 Force Measurements in a Dilute Electrolyte

To confirm that the observations made in the measurements in C_4C_1pyrr TFSI described in the previous section are particular to the IL, control measurements were made in KCl (aq) at two different concentrations (1.5 mM and 0.6 mM), also with the asymmetric gold/mica SFB. These measurements were made particularly to verify that it was possible to come into adhesive contact at 0 nm, and to see if attractive and repulsive forces between the surfaces are observed. Additionally, these experiments yielded interesting results independently of their role as a control, and demonstrated that the new gold/mica setup described in Ch. 3 has excellent resolution.

The KCl aqueous electrolyte was chosen for two reasons:

- Most organic solvents relevant to electrochemical measurements dissolve EPON epoxy glue. Several options were tested but all dissolved the glue

of the lenses almost immediately. Water was the only common solvent that was found not to damage the lenses.

- Water is relevant as a solvent for electrochemistry. KCl (aq) is a common electrolyte and has been reported in conventional electrochemical measurements [139] and in classic SFB measurements [11, 140], so there is material to which results can be compared, whilst remaining relevant to the field of electrochemistry.

Fig. 4.6 and 4.7 show results of force profiles under potential control in KCl (aq) for concentrations of 1.5 mM and 0.6 mM respectively. It should be noted that the open circuit potential (OCP) for both of these experiments is quite high, around 300 – 350 mV, and as such the negative applied potentials result in *less positive* effective potentials, rather than negative effective potentials. In all force profiles in Fig. 4.6 and 4.7, a long-range decay is observed in the 25 – 10 nm region, then the surfaces jump into adhesive contact from a distance of 10 nm to one of 4 – 2 nm, with an average jump-in distance of 7.5 nm. As shown in more detail Fig. 4.10, the surface jump in to a slightly larger separation of $\sim$ 4 nm when the applied potential is positive, and to a smaller separation of $\sim$ 2 nm for negative potentials. A repulsive force is observed in the 2 – 0 nm region, and the surfaces come into adhesive contact at 0 nm. In the KCl (aq) 0.6 mM solution, layering of K^+, Cl^- and water molecules was observed, as shown in Fig. 4.10. There appears to be a small change in the magnitude of the forces with the magnitude of the applied potential. It is possible that potassium cations and chloride anion adsorb on the surfaces of the mica and the gold respectively, which would screen the surface charge and result in a weaker effective charge – hence the interactions changing only weakly.

The surfaces coming into adhesive contact at 0 nm in dilute KCl (aq) suggests that the "hard wall" observed in C_4C_1pyrr TFSI is particular to the interactions of the IL with the metal surface. The apparent small change in magnitude

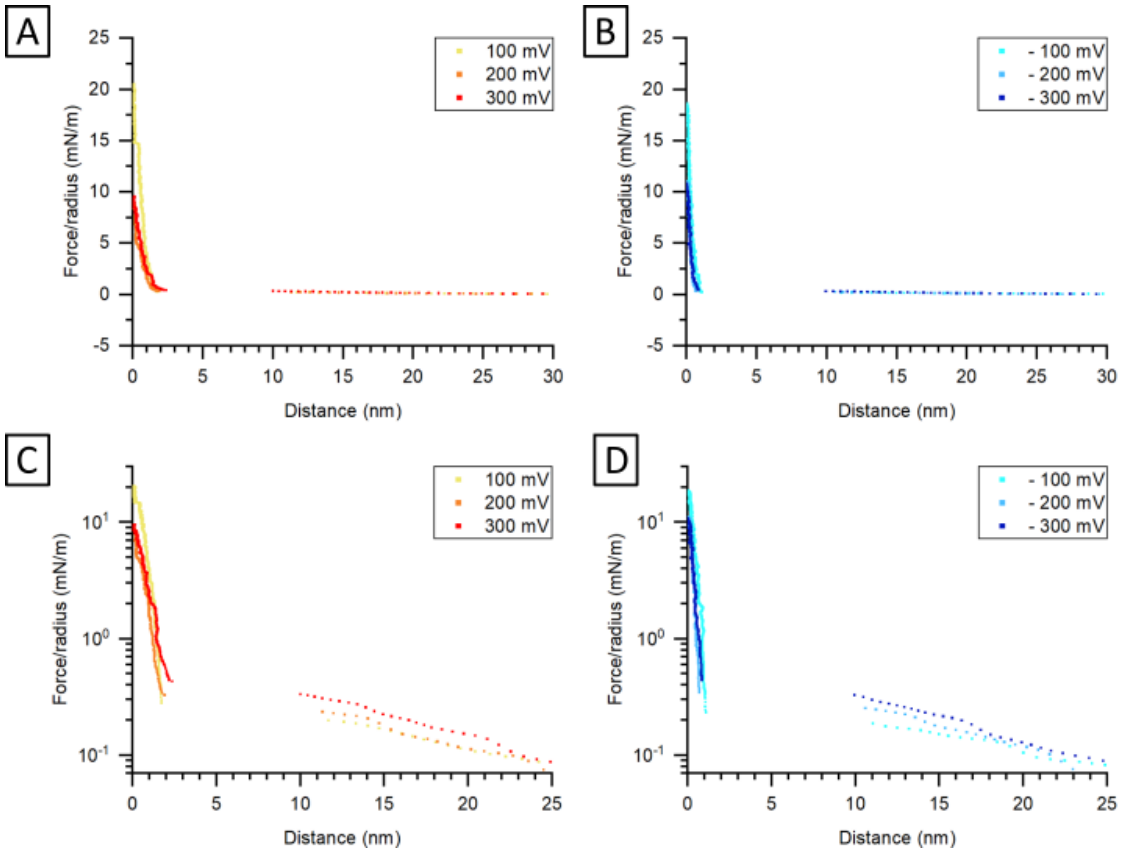


Figure 4.6: *Force profiles under potential control in KCl (aq) 1.5 mM, with force profiles at positive potentials between +100 and +300 mV on (A) a linear-linear scale and (C) a log-linear scale, and force profiles at negative potentials between −100 and −300 mV on (B) a linear-linear scale and (D) a log-linear scale. No change in screening length is observed with modifying surface potential. Surfaces come into adhesive contact at 0 nm after a jump-in of about 7.5 nm.*

of the forces with applied potential in dilue KCl (aq) also supports the theory that the absence of shift in magnitude in IL is particular to that system.

The screening lengths in KCl (aq) do not change with varying potential. Expected screening length for these concentrations can be calculated using the following model: when considering the Stern layer and Helmholtz plane, where the Poisson-Boltzmann equation does not hold, if one assumes that the dielectric constant of the combined Stern-Helmholtz layer is uniform and denote it as ε_δ, it can be modelled as a capacitor. We use a capacitor with plates of charge densities $\pm\sigma$ and of potential difference ψ_0 separated by the Debye length $1/\kappa$. At

Table 4.4: *Screening lengths measured from force measurements shown in Fig. 4.6.*

Screening Lengths – KCl (aq) 1.5 mM		
Applied potential	Screening length [nm]	Error [nm]
OCP	9.8	0.9
0 mV	11.0	0.8
100 mV	10.1	0.8
200 mV	11.3	0.8
300 mV	10.1	1.2
- 100 mV	11.8	1.0
- 200 mV	10.2	1.0
- 300 mV	9.9	1.2

Table 4.5: *Screening lengths measured from force measurements shown in Fig. 4.7.*

Screening Lengths – KCl (aq) 0.6 mM		
Applied potential	Screening length [nm]	Error [nm]
OCP	15.4	0.3
0 mV	13.3	0.8
100 mV	15.7	0.2
200 mV	13.2	0.4
300 mV	14.1	0.9
- 100 mV	14.5	0.4
- 200 mV	12.8	0.7
- 300 mV	14.0	0.7

low potentials, the simplified Grahame equation, which relates σ and ψ_0 gives us:

$$\sigma = \varepsilon_0 \varepsilon \kappa \psi_0 \tag{4.6}$$

So the potential ψ_0 is proportional to surface charge density σ, and the magnitude of Debye length $1/\kappa$ is dependent only on the properties of the electrolyte. Filling in variables for an aqueous 1:1 electrolyte solution:

$$\kappa^{-1} = 0.304/\sqrt{M}\ nm \tag{4.7}$$

This gives us a screening length of 7.9 nm for 1.5 mM KCl (aq) and 12.4 nm for 0.6 mM KCl (aq). The average measured screening lengths for 1.5 mM KCl (aq) is

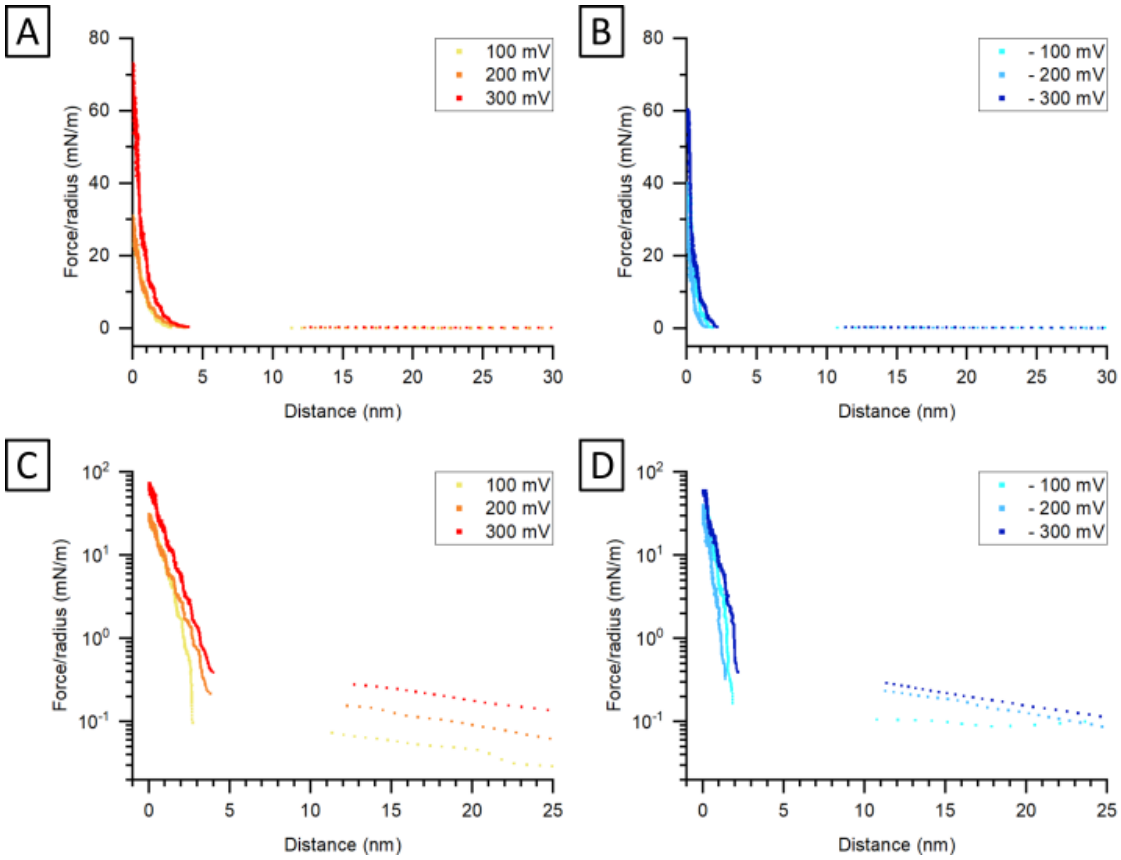


Figure 4.7: *Force profiles under potential control in KCl (aq) 0.6 mM, with force profiles at positive potentials between +100 and +300 mV on (A) a linear-linear plot and (C) a log-linear plot, and force profiles at negative potentials between −100 and −300 mV on (B) a linear-linear plot and (D) a log-linear plot. No change in screening length is observed, and the surfaces come into adhesive contact at 0 nm. The jump-in is of about 7.5 nm. A repulsive force and layering of ions and water molecules is observed after the jump-in – this is shown in more detail in Fig. 4.10.*

10.6 nm and 14.1 nm for 0.6 mM KCl (aq), which means concentrations may have been closer to 0.8 mM and 0.5 mM respectively. If Debye-Hückel applies quantitatively in this range, then the measured values of $1/\kappa$ imply concentrations of 0.8 mM and 0.5 mM, but it may already be non-quantitative at mM concentrations [141], so hereafter the concentrations measured when preparing the solutions (0.6 mM and 1.5 mM) will be used to refer to the dilute electrolytes.

The screening length for the dilute electrolyte doesn't change with changing potential, which is as expected from the Debye length calculation above. Due to the stable electrochemical window of water being quite narrow compared to

the IL (2.3 V for 0.1 M KCl (aq) [142] and approx. 1 V for 0.6 mM as measured by cyclic voltammetry) it cannot be said for sure that there is a change in magnitude in the screening lengths, but there does appear to be a trend. In all force profiles,

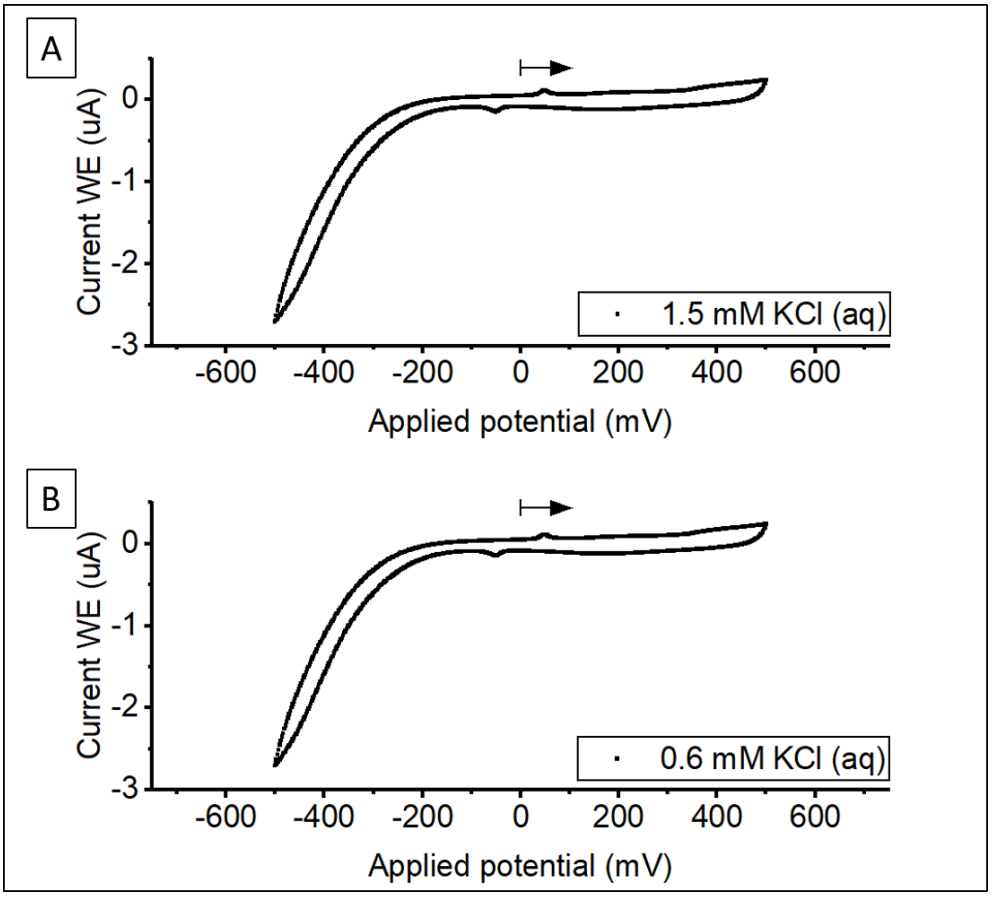


Figure 4.8: *Cyclic voltammograms of dilute potassium chloride (KCl) in water (A) 1.5 mM and (B) 0.6 mM.*

a large "jump" into contact occurs from a distance of about 10 nm to about 3 nm from contact. On average, these jumps are measured to be of about 7.5 nm. This can be explained by van der Waals forces taking over as the surfaces approach each other, and they have been observed in other studies using gold/mica surfaces [52, 88] and mica/mica surfaces [41, 143, 144]. If we consider this within the constant potential/constant charge, where the gold surface has constant potential and the mica surface has constant charge, and we assume that the gold potential has a negative effective potential (as suggested by the repulsive forces seen in the force profiles), the electrostatic interaction between the surfaces falls into the regime of "Surfaces of the Same Sign: Higher Potential Surface is at Constant

Potential" described in McCormack *et al.* [78].

The force profiles were fitted with a DLVO equation, as shown in Fig. 4.9, which shows a force profile (blue) of KCl (aq) 0.6 mM at -300 mV on a log-linear scale with the best fit of the long-range exponential decay (red), the best fit of the repulsive region (pink) and the DLVO best fit. The pink trace is a good fit of the repulsive region, from 2 – 0 nm, but does not fit the large jump-in (10 – 2 nm) or the long-range decay, whereas the red trace is a good fit of the exponential decay but doesn't fit the other two regions. The green trace shows good agreement with the force profile, particularly in the long-range region, and the jump-in matches up with the width of the well. The fit is not as good for the repulsive region, but it should be noted that structural forces were observed in this regime, which DLVO does not account for and will affect the fit. The Hamaker constant used to obtain the best fit was 8.5×10^{-20} J, which is in close agreement with other works [54, 58, 88].

When using different substrates, the potentials of the two surfaces cannot be decoupled, so care must be exercised when drawing conclusions. Here the mica was taken to have a potential of -110 mV [11, 41, 88], and assumed the effective potential on the gold surface was not equivalent to the applied potential. Repulsive forces are seen in the force profiles at applied potentials between ±300 mV, which suggests that the effective potential is always negative. The PZC was not measured in these experiments, but the PZC of aqueous potassium salt solutions at 10^{-3} salt concentration has been reported on various surfaces to be between 4-9 V [145]. To our knowledge there are no reports of the PZC of KCl (aq) at 10^{-3} M concentration on ultra-smooth gold surfaces. If we take the PZC to be 400 mV, the surface of the gold is always positive, but it is possible that strong chloride adsorption on the surface could screen the charge and result in an overall negative effective potential on the gold surface. It is also possible that charge inversion is occurring on the surface, as seen in other works in dilute electrolytes

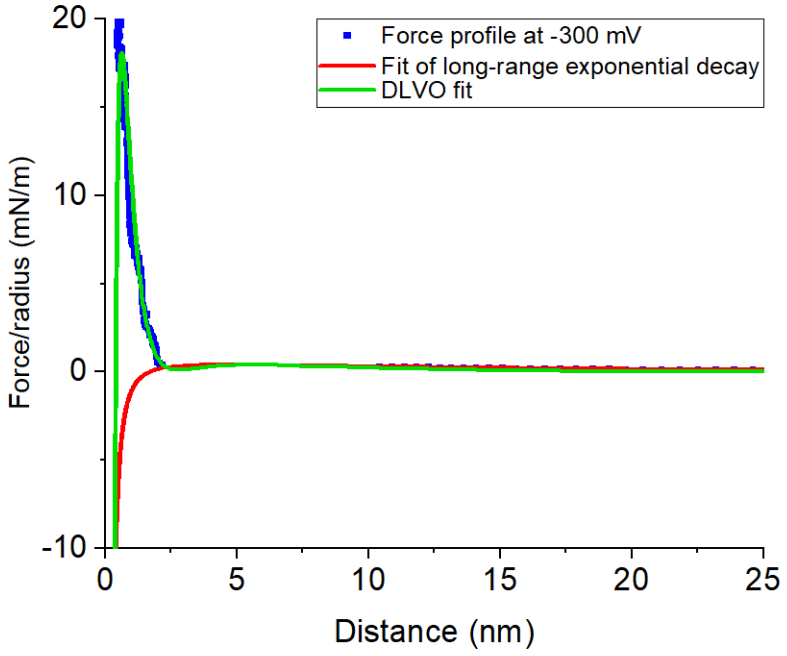


Figure 4.9: *Example of the fits used for the dilute KCl (aq). The blue trace is the force profile from KCl (aq) 0.6 mM at −300 mV, the red trace is the best fit for the long-range exponential decay, the pink trace is the best fit for the repulsive region near contact and the green fit is the DLVO fit of the whole profile, using a Hamaker constant of* 8.5×10^{-20} *J. Structural forces are observed in the repulsive region, which makes fitting it harder as DLVO does not account for these.*

[54, 58, 72]. Repeating these experiments with other dilute electrolytes would help clarify this.

The long-range tail decays exponentially and has a screening length of 14 nm. The large jump-in can be interpreted as the van der Waals forces taking over and resulting in a strong attractive force between the surfaces. Indeed we expect van der Waals forces to be dominant at this length scale [41, 52, 88, 143, 144, 146]. This is in agreement with work from Tivony *et al.*, which showed that the gold-mica contact is predominantly controlled by van der Waals forces [71]. The region from the end of the jump-in at 2 nm to when the surfaces come into contact at 0 nm shows fairly good agreement with the repulsive regime of the green fit, although stuctural forces are not accounted for in DLVO theory. Oscillatory behaviour was observed in the 0 – 2 nm range, after the jump; this is

discussed in the next section.

These measurements and fits are in agreement with previous work in dilute electrolytes (including KCl (aq)) in classic and gold/mica SFB for OCP [11, 58, 71]. It has been shown that Cl^- ions may adsorb on gold surfaces [147–150], so if this is the case, it may be that this layer is screening some of the surface charge, but there appears to be a slight shift in the magnitude of the forces. All of the force profiles show a monotonic decay at large distances and in the more dilute solution, an oscillatory decay is observed that corresponds to hydrated K^+ and Cl^- ions and interstitial water molecules.

4.3.3 Layering of KCl Ions and Water

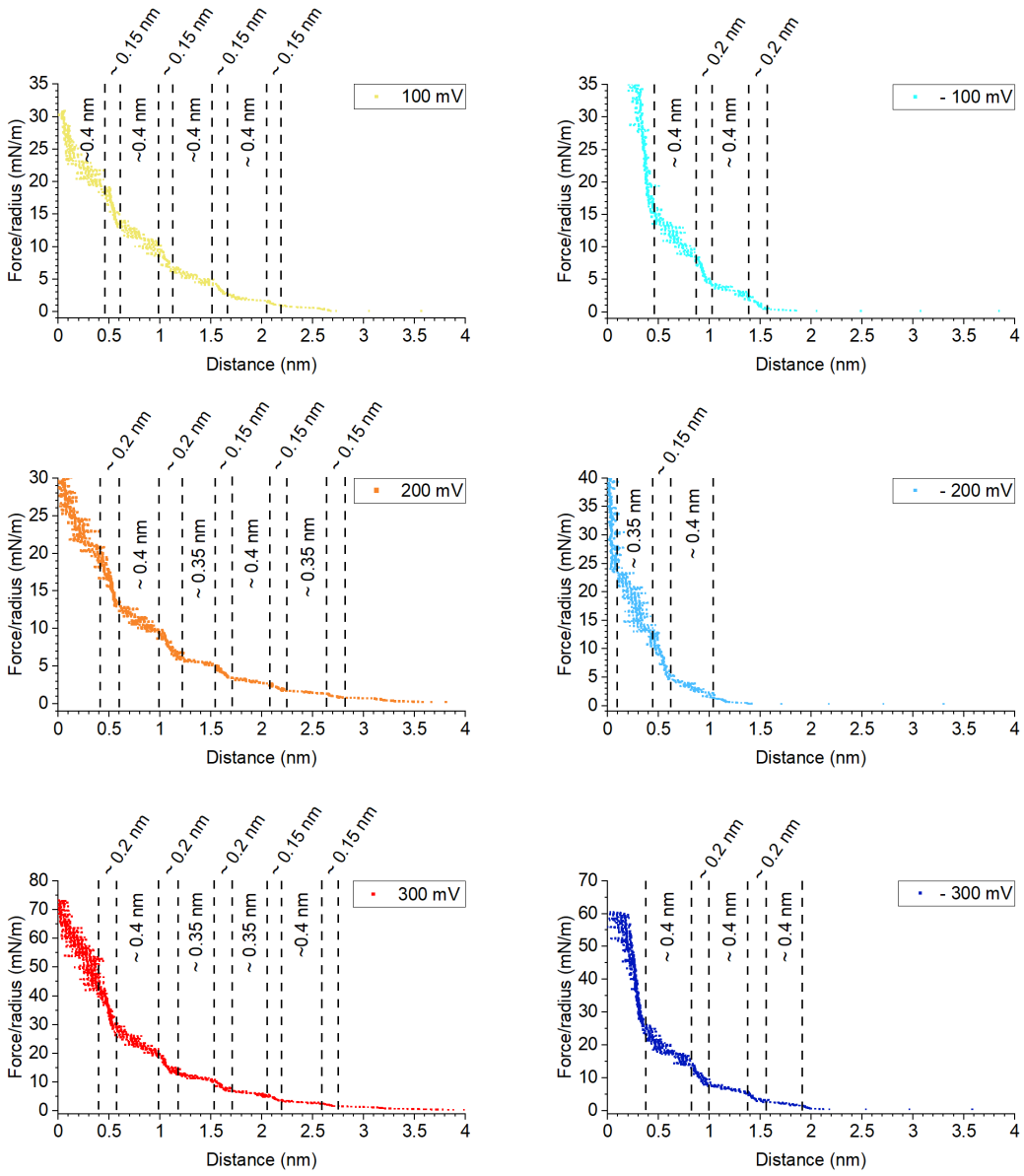


Figure 4.10: *Plots focussing on the 4 – 0 nm region of force profiles in KCl (aq) 0.6 mM at applied potentials. After the surfaces jump in to 4 – 1.5 nm separation, steps can be observed while the surfaces approach each other. There are two types: large steps of ∼ 0.4 nm and small steps of ∼ 0.2 nm. The large steps resemble structural force profiles seen in mica/mica experiments where oscillatory behaviour is observed, which are characterised by steps corresponding a layer of ions are expelled from the slit when the applied pressure reaches the maximum of an oscillation. The small steps have a steeper gradient than the large ones, which indicates a less favourable process where there is some resistance in the expulsion process. From the dimensions of the small steps, it can be deduced that they corresponds to the compression of water molecules. At positive potentials, layering can be seen from further out than negative potentials.*

In the 0.6 mM KCl (aq) solution layers were observed during the approaches, as shown in Fig. 4.10. This speaks to the high resolution of the novel asymmetric setup and to our knowledge has not been observed previously with an asymmetric metal/mica SFB. It can also be noted in Fig. 4.10 that layers can be observed from further out when higher positive potentials are applied.

The hydrated ion diameter of potassium is reported as about 0.66 nm [130–133] and the hydrated chloride ion as 0.57 nm [132–134]. The van der Waals diameter of water is 0.275 nm [127, 128]. In Fig. 4.10 it can be observed that the larger "steps" correspond approximately to a hydrated ion diameter, and the smaller "squeezes" may correspond to water molecules. Similar steps have been reported in KCl (aq) 0.6 mM in the classic mica/mica setup [151].

4.4 Conclusion

It has been demonstrated that applying potentials to a confining surface does not affect the screening length measured for an ionic liquid. However, the magnitude of the force is also unaffected, which is unexpected. An unusual hard wall at 2 nm was observed as well, which was attributed to capillary freezing as reported by Comtet *et al.*. Together these observations suggests that surface potential is completely screened with a few bilayers of ionic liquid. The resulting non-zero effective charge then arises from accumulation of the IL interface due to asymmetry in the liquid. Layering of the ionic liquid was also observed, which to our knowledge has not been reported previously in a gold/mica electrochemical SFB setup.

Control measurements were made in KCl (aq) at two different concentrations, 1.5 mM and 0.6 mM. These showed screening lengths qualitatively similar to Debye-Hückel predictions, and contact at 0 nm. In the 0.6 mM electrolyte, lay-

ering of potassium and chloride ions and water molecules were observed, which not been achieved before in a gold/mica electrochemical setup.

These measurements provide clues as to what governs underscreening, and raises other questions regarding the behaviour of concentrated electrolytes near charged surfaces. They also prove that when gold lenses are carefully and precisely made, resolution comparable to that in mica/mica SFB can be achieved. This demonstrates that the asymmetric setup, already well-established in the field, can still be improved on.

Chapter 5

Results from the Gold/Mica SFB Setup: Charging Dynamics

5.1 Introduction

In electrochemistry, two essential processes interplay: the transport of molecules (reactant and product) to and from the electrode interface, and the flow of charge at the interface. Understanding both of these is critical to the study of electrochemical reactions, and the electrical double layer (EDL) plays a crucial role in this. The structure of the EDL will influence the movement of ions and neutral molecules to and from the interface, which in turn influences the flow of electrons at the surface.

In dilute electrolytes, the EDL is well characterised, but in concentrated electrolytes and especially ionic liquids, this is not the case [100, 152]. A number of factors can be pointed out as particularly challenging in the determination of a definitive theory: ionic liquids have high ionic densities, are often composed of large and flexible molecules which can be polarized, and have complex and highly variable chemical properties. Because there is no solvent and most ionic liquids

have low melting points, certain forces that can be ignored in dilute electrolytes become important components to consider: Coulombic forces, dispersion forces, π-stacking and hydrogen bonding, to name a few.

Although there is no consensus on a definitive model for ionic liquids, several have been proposed that break down the EDL into an inner and an outer layer, the latter being more diffuse than the former [77, 153]. Theories on how ionic liquids and their EDLs respond to charged surfaces vary [87, 100, 153, 154]. In the models proposed by Kornyshev *et al.*, the relative permittivity of the ionic liquid does not vary with distance from the charged interface [77, 87, 153]. In opposition to this, Lauw *et al.* propose that the molecules composing the ionic liquid are polarizable and the electric field of the electrode imposes order on the EDL [154]. Lockett *et al.* also discuss the importance of adsorption of molecules on electrode surfaces and how it could influence the charging of the cell; very little is known about adsorption isotherms of ionic liquids, but it is a factor that must be considered when discussing charging/de-charging processes. It has also been shown that some cations (*e.g.* pyrrolidinium, imidazolium, piperazinium) and anions (*e.g.* TFSI) adsorb on the surface of a cell and reorient when changing to potentials away from the potential of zero charge (PZC) [155, 156]. The PZC is defined as the potential of the electrode at which the charge of the electrode-electrolyte interface is zero, and is used to determine the absolute electrode potential in the electrolyte.

To add to the complexity of this picture, what few theories have been elaborated to describe bulk or near-infinite ionic liquids cannot be used to discuss them in nano-confinement [100]. In confinement, conductivity can be significantly different from in the bulk due to ion collisions with the confining surfaces, hindrance to the ions passing each other within the pore and the electrode surfaces screening electrostatic interactions. Additionally, the surface area of the electrode, its porosity and the length of the pores are all important factors.

Potential step methods are used to study the kinetics within an electrolyte or a chemical reaction, the diffusion/migration of ions within the liquid and the adhesion of chemical species to charged surface. In these methods, a time-dependent square-wave potential is applied to an electrode, and the current is recorded as a function of time; these are some of the most powerful tools to study electrolytes electrochemically [118]. A potential step at the electrode results in a spike in current, which then decays back to equilibrium. The shape and timescale of this decay curve is determined by many parameters: the nature, size and geometry of the surface, and the nature of the electrolyte, as the concentration, charge localisation and shape/sterics of the ions will affect their response to the potential change, which in turn affects how the current of the surface changes. Chronoamperometry is concerned with recording the current resulting from the application of a square-wave potential to an electrode, whereas chronocoulometry is concerned with the charge (integrated current).

In dilute electrolytes such as KCl (aq), composed of single atom ions that can be treated as spherical charges, there is no molecular conformational change possible, so there are two relaxation modes for the current: a near-instantaneous electronic response and a slower diffusive response, where ions will move in the bulk and EDL to adopt the lowest-energy state and minimise the current. Ionic liquids have much higher ionic density and are largely made up of asymmetric, flexible molecules that can bend and distort, and often have asymmetric charge distribution. It has been shown that they can have complex responses to electric fields in nano-confinement as a result of the cumulation of numerous factors, such as concentration, composition of the liquid, composition of the confining surfaces, temperature, adsorption, steric effects [152, 155, 156]. It is possible, and indeed probable, that ionic liquids have more than two modes of relaxation. Roling *et al.* described this in 2012, showing with electrochemical impedance spectroscopy (EIS) that there are three relaxation modes in the IL 1-butyl-1-methylpyrrolidinium tris(pentafluoroethyl)trifluorophosphate ($Py_{1,4}FAP$) [98, 157] .

In this chapter, the interfacial behaviour of C_4C_1pyrr TFSI and of dilute KCl (aq) (1.5 and 0.6 mM) between gold and mica surfaces at close separations ($<$5 nm) are observed within their respective electrochemical windows through the use of chronoamperometry and chronocoulometry. The results obtained shed a some light on the charging dynamics and interfacial behaviour of the confined liquids, in particular how layering is affected by square-wave potential methods and how the current decays after a potential is applied to the gold surface.

5.2 Theory

In potential step methods, a potentiostat is used both to control the potential and monitor the electrical response of a three-electrode cell during an experiment. To achieve a particular potential at the surface of a working electrode (WE), the potentiostat passes a current through the cell to achieve this set potential. It adjusts the voltage to maintain a potential difference, which is measured between the working electrode and the reference electrode (RE). As the conditions in the electrolyte change due to the applied potential, so does the current required to maintain surface potential. This means that the current reflects the flow of electrons required to maintain a particular potential at a surface as well as any electrochemical process that might be occurring on it. When time-dependent square-wave potential steps are applied to the WE and the resulting current is recorded vs time, this is known as chronoamperometry, and when the integral of current (*i.e.* charge) versus time is recorded, this is known as chronocoulometry. Here the theory that applies to bulk measurements will be briefly discussed to explain the relevance and versatility of potential step methods. Only reversible processes will be covered, as all the measurements reported here were performed within the stable electrochemical windows of the liquids, in order to avoid irreversible chemical reactions.

The movement of a species within the electrochemical cell is governed by the cumulation of several transport phenomena: diffusion is defined as the movement of a species due to a chemical potential gradient; migration is the movement of a charged species due to an electrical potential gradient; convection is caused by stirring or hydrodynamic transport. Together, they contribute to total mass transfer, or the movement of a species from one point to another. By eliminating one or two of these modes of transport, it becomes possible to characterise the others.

Approaching a bulk electrochemical experiment with conventional mean-field theory, we use Fick's laws, which describe the flux and concentration of a species as a function of time, and the current-potential characteristic, which describes the relation between current and potential in a given system. Fick's laws are as follows:

1st law $-J_O(x,t) = D_O \frac{\partial C_O(x,t)}{\partial x}$

2nd law $\frac{\partial C_O(x,t)}{\partial t} = D_O(\frac{\partial^2 C_O(x,t)}{\partial x^2})$

where $J_O(x,t)$ is the diffusion flux, defined as the number of moles of species O passing a particular point per second per cm^2 area normal to the axis of diffusion, D_O is the diffusion coefficient, C_O is the concentration of O, t is time and x is the position. The first law shows that flux is proportional to concentration gradient ($\partial C_O(x,t)$), and the second law describes how concentration changes with time.

Describing current as a function of potential underpins a large portion of electrochemistry. From a practical point of view, current and potential can both be measured with commonly available equipment (*e.g.* multimeter, potentiostat), and a current-potential plot yields a wealth of information about the electrodes, the electrolyte, and physical and chemical processes within the liquid and at the interface. Concentration, standard potential, mass transfer coefficients, kinetic pa-

rameters, equilibrium and rate constants can be derived from a current-potential curve. The current-potential characteristic is given by the Butler-Volmer equation [118]:

$$i = FAk^0[C_O(0,t)e^{-\alpha f(E-E^{0'})} - C_R(0,t)e^{(1-\alpha)f(E-E^{0'})}]$$

Where i is the current, F is the Faraday constant, A is the frequency factor, k^0 the standard rate constant, α the transfer coefficient, $E^{0'}$ the equilibrium potential reference point, E the new potential,and $f = F/RT$, where R is the ideal gas constant and T is temperature.

In bulk measurements where a potential is being applied to an electrode, the effect of the transport of the species to and from the electrode is extremely important, as the reaction rate depends on how quickly unreacted species can diffuse towards the surface. When considering an experiment under diffusion control, we use the Cottrell equation to find the diffusion-limited current $i_d(t)$ [118]:

$$i(t) = i_d(t) = \frac{nFA{D_O}^{1/2}C_O^*}{\pi^{1/2}t^{1/2}} \tag{5.1}$$

Where n is the number of electrons involved in the reaction, D_O is the diffusion coefficient, $C_O^* = \lim_{x\to\infty} C_O(x,t)$ and t is time.

However, it should be noted that while the diffusion layer is used to refer to the area close to the surface of the electrode where the concentration of the electrolyte behaves differently to the bulk, its thickness depends on a number of factors and there are several different ways of defining it. In a nano-confined liquid, the movement of ions in and out of the pore is hindered, as steric effects within the liquid and the geometry of the nanopore make it difficult for ions to move past each other. This means that diffusion and migration behave very differently in confinement and are often much slower than in the bulk.

For a potential step method in a reversible chemical process, we obtain a curve showing how current varies as a function of time when potential is applied

and held at a given value for a certain period of time t. In this characteristic curve, we can consider two regimes: the first occurs in the timescale where current is transient, and the second in the later timescale where the system has reached a steady-state. The details of the reversible current-potential curve, or wave, can be used to extract a huge wealth of information regarding these processes. As there is no definitive theory applicable to ionic liquids in nano-confinement, in our measurements of current vs time a fitting tool was used to obtain the best fit of the current decay curves.

5.3 Material and Methods

All the measurements discussed here were measured in situ in the electrochemical call of the gold/mica SFB. The setup and electrochemical cell were prepared as described in Ch. 3, Fig. 3.9 and Fig. 3.6. All glassware was sonicated in chloroform $\times 2$, toluene, isopropanol, ethanol, rinsed in ultra-pure water and cleaned in piranha solution (3:1 concentrated sulfuric acid 99% : hydrogen peroxide 30%). Stainless steel parts and tools were sonicated in the same solvents as the glassware, rinsed with water and cleaned in nitric acid (2:1 water : nitric acid 70%).

As in Ch. 4, the ionic liquid 1-butyl-1-methylpyrrolidinium bis(trifluoromethanesulfonyl)imide (C_4C_1pyrr TFSI) was dried on a Schlenk line overnight (5×10^{-3} mbar, 60° C) and measurements were performed under nitrogen atmosphere. A small pot of P_2O_5 was kept in the sealed chamber of the SFB to absorb atmospheric water. The KCl (aq) solutions were prepared on the day of the experiment with tools and glassware freshly cleaned as described above. The dimensions of these ions are presented in Tab. 4.1.

The three-electrode cell is described in detail in Ch. 3, but the working

electrode (WE) was the gold surface of the bottom lens, the pseudo-reference electrode (RE) was a silver wire and the control electrode (CE) was a platinum wire.

5.4 Results and Discussion

5.4.1 Ionic liquid

Chronoamperometry

The surfaces were brought into "contact" (hard wall at $\sim$ 2 nm where closer approach is no longer possible) before the experiment was started. The chronoamperometric cycle was composed of repeat potential steps from positive to negative values, which were each held for 30 s or 60 s. These times were chosen empirically by monitoring how quickly the current decays back down to an equilibrium value. Each positive/negative step was repeated three times before moving on to the next. Current vs time was recorded with a potentiostat (Metrohm μAUTOLABIII/FRA2 impedance analyser, Metrohm), and the change in the separation between the surfaces was monitored using the same interferometric method as in the previous chapter, which allowed for a direct observation of the mechanical response of the confined film to potential steps.

Fig. 5.1 shows a plot of distance vs time during a full chronoamperometric cycle in C_4C_1pyrr TFSI. For $\pm$100 mV, there is no significant change in separation with potential steps. For $\pm$200 mV and $\pm$300 mV, it is possible to see a small response, a small "squeeze in" when the applied voltage is positive and corresponding "squeeze out" when the voltage is negative. This behaviour is seen more distinctly with $\pm$400 mV, and for $\pm$500 mV we begin to observe a defined change in film thickness of about 0.05 nm in response to potential steps.

For $\pm$800 mV and $+$1 V/$-$900 MV the relative distance change is clearer, with a defined step down (positive potentials) and up (negative potentials) of about 0.1 nm, which is much smaller than the thickness of a bilayer ($\sim$ 0.8 nm), or even the smallest dimension of a single C_4C_1pyrr cation or TFSI anion ($\sim$ 0.5 nm) [26, 27, 129]. Over the course of the whole cycle, the absolute separation goes from 2.6 nm to 1.8 nm.

In order to estimate whether the field between the surfaces resulting from the applied potential is sufficient to cause a change in orientation of the molecules, we need to compare the magnitude of the energy (per unit volume) of the electric field and at each applied voltage to the thermal energy. This will give the voltage at which the electric field is great enough to cause the re-orientation of dipoles. We use the energy introduced by the electric field U^E:

$$U^E = \frac{1}{2}\varepsilon E^2 \tag{5.2}$$

Where $\varepsilon = \varepsilon_0\varepsilon_r$, with ε_0 the permittivity of free space and ε_r the permittivity of C_4C_1pyrr TFSI, and E the electric field. The electric field E across a dielectric can be expressed as:

$$E = \frac{V}{D} = \frac{\Delta\psi}{D} \tag{5.3}$$

Where V is the voltage, D is the distance between the surfaces (here the distance between the gold and the mica surfaces) and $\Delta\psi$ is the difference in effective potential between gold and mica, such that $\Delta\psi = \psi_{eff}^{Au} - \psi_s^{mica}$. U^E is compared to the thermal energy density U^{Th}:

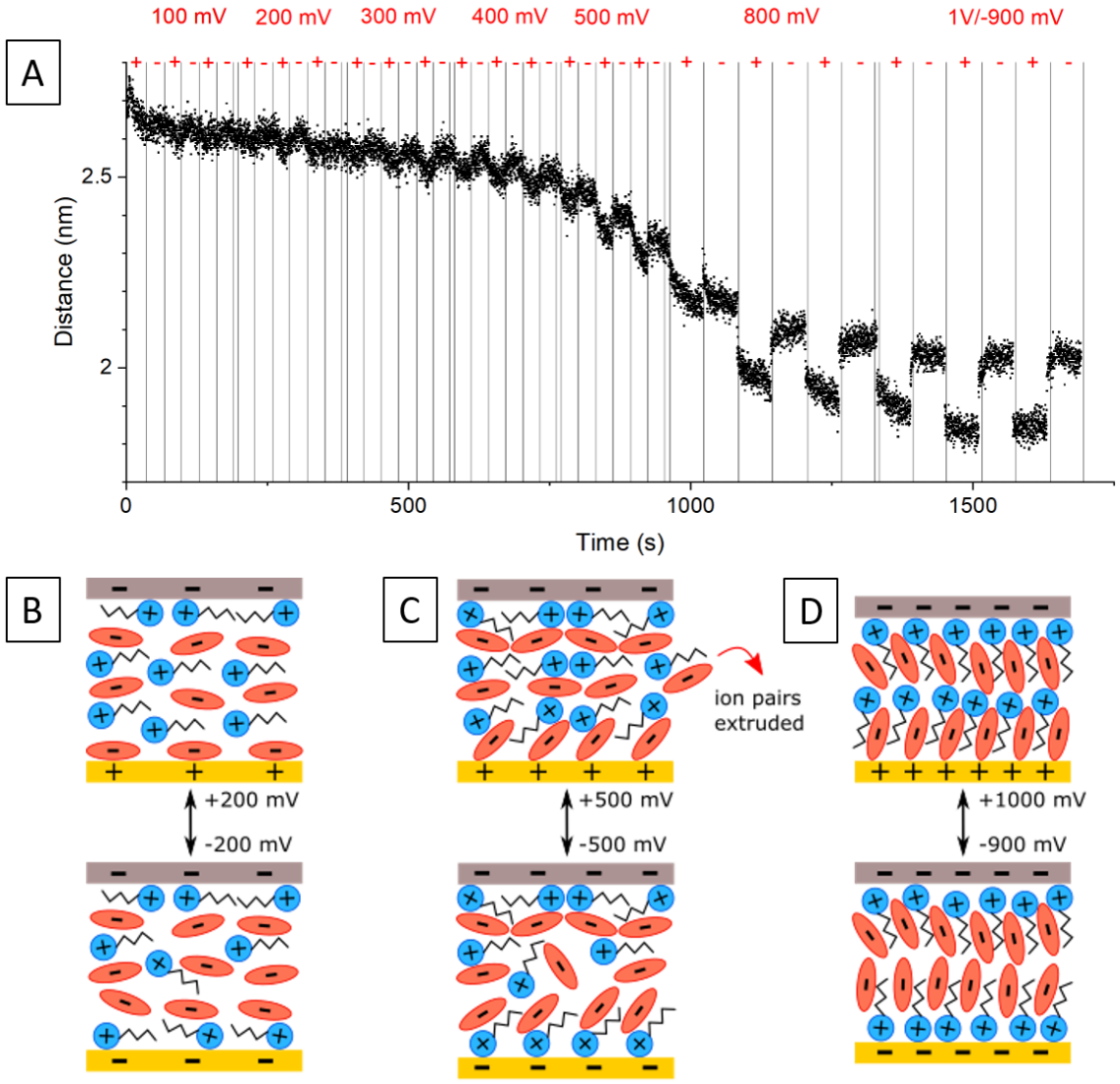


Figure 5.1: *(A) Separation vs times during the chronoamperometric cycle in C_4C_1pyrr TFSI. Dotted lines indicate the moment where potential is stepped. The separation change for the small steps ($\pm$100 mV and $\pm$200 mV) is negligible, but a small response is visible. As the steps are increased, this response is accentuated, with a distinct "squeeze in" and "squeeze out" from $\pm$400 mV. When switching between $+$500 mV and $-$500 mV, there is a more distinct change in separation, where positive steps cause the surfaces to move together by about 0.1 nm. At the same time, an inward drift can be observed. At the first $\pm$800 mV set, the drift is accentuated and the surfaces move together despite the switch to negative surface potential, suggesting that ions are being expelled from the slit. Thereafter, ($\pm$800 mV and $+$1 V/$-$900 mV), the surfaces move towards and away from each other by approximately 0.2 nm. (B) Cartoon depicting the change in the slit at small potential gaps. (C) Cartoon depicting the change in the slit at moderately large potential gaps. Ions tilt when the potential is moved away from the PZC [155], and ion pairs are gradually extruded over several iterations of the potential steps. (D) Cartoon representing the change in the slit at large potential gaps. The ions in contact with the surface are tilted.*

$$U^{Th} = \frac{k_B T}{a^3} \tag{5.4}$$

Where k_B is the Boltzmann constant, T is the temperature and a^3 is the molecular volume. We use $a^3 = 0.5 \times 10^{-27}$ m^3 per molecule (obtained from the molar concentration of C_4C_1pyrr TFSI), which gives us $U^{Th} = 50 \times 10^6$ Jm^{-3}.

To solve the equation for U^E, certain approximations must be made, as ILs in confinement do not behave in the way bulk theory predicts. For the purpose of this order of magnitude calculation, we treat the nanoconfined IL as a bulk dielectric. The bulk value of ε_r is 10-12 $CV^{-1}m^{-1}$, but is likely smaller in confinement and with ordering of ions [158]. For this calculation, we take the bulk dielectric permittivity $\varepsilon_r = 10$ $CV^{-1}m^{-1}$. We take $D = 2 \times 10^{-9}$ m and assume this distance is constant (in reality it is not).

To know the effective potential on gold, it is necessary to estimate the values of ψ_{eff}^{Au} from the applied voltages $\psi_{applied}^{Au}$. For this, the potential of zero charge (PZC) needs to be known, as $\psi_{eff}^{Au} = \psi_{applied}^{Au} - PZC$; the PZC of C_4C_1pyrr TFSI was not measured in our experiments. The PZC of ILs is difficult to measure due to the "camel" shape of the maxima of the potential dependence of the double-layer capacitance and the adsorption of ions to the surface of the electrode, which is not accounted for by current models [87, 152]. Lockett *et al.* estimate the PZC of bulk C_4C_1pyrr TFSI to be - 450 mV (measured in bulk with a "rough" gold electrode and Ag/Ag^+ reference electrode), and although this value is expected to be different at an ultra-smooth electrode, we use the above value here for the purpose of this calculation. The ψ_{eff}^{Au} for every value of ψ_{eff}^{Au} is shown in Fig. 5.2. The surface potential of mica ψ_s^{mica} is taken to be constant and to have a value of $\psi_s^{mica} = 100$ mV, obtained from Israelachvili [10] and from Coles *et al.* [27]. In practice, the IL is not a dielectric and will screen this ψ_{eff}^{Au} in an oscillatory

manner, but for the purpose of this calculation, we will proceed while considering the IL as a dielectric behaving as a bulk mean-field liquid.

Using the values above, we can calculate E for $\psi^{Au}_{applied} = +200$ mV, where $\Delta\psi = \psi^{Au}_{eff} - \psi^{mica}_{s} = -0.25 - (-0.1) = -0.15$ V. This gives us $U^{E}_{200mV} = 0.253 \times 10^{6}$ Jm^{-3}, which is a lot less than U^{Th}, and correlates with a very small change within the slit (see Fig. 5.1(A)). Repeating this calculation for $\psi^{Au}_{applied} = -500$ mV, we obtain $U^{E}_{-500mV} = 6.33 \times 10^{6}$ Jm^{-3}, which is an order of magnitude less than U^{Th}, and this potential step does result in more noticeable change within the slit. For $\psi^{Au}_{applied} = -800$ mV, we obtain $U^{E}_{-800mV} = 14.88 \times 10^{6}$, which is the same order of magnitude as the thermal energy U^{Th}, which suggests that the field should be strong enough to cause a change in the dipole orientation of the ions in the liquid. This correlates with the $\pm$800 mV and $+1$ V/$-$900 mV steps in Fig. 5.1 (A).

This rough calculation shows that the results obtained for the chronoamperometric measurement shown in Fig. 5.1 (A) are in line with what is expected from the theory. It is clear that when a few hundreds of mV are applied, the field is strong enough to limit the thermal motion and thus drive orientation of dipoles within the field. Additionally, we observe that the change in direction of the electric field occurs for applied voltages of 500 mV or above, which coincides with the observation of ion layers being squeezed out of the slit. Finally, there are two elements concerning the electric field $\Delta\psi = \psi^{Au}_{eff} - \psi^{mica}_{s}$ are particularly noteworthy. First, the absolute value of $\Delta\psi$ determines how "free" the ion dipole are within the field, so for a small value of $\Delta\psi$ the electric field is smaller relative to the thermal energy, resulting in ions being more free. Second, if the switching of voltage causes a large change in the electric field (large step and/or change of direction), the ions must rearrange, especially in the case where the sign changes.

Considering the order of magnitude calculation above, the "squeezes" can be interpreted in as a combination of two simultaneous effects:

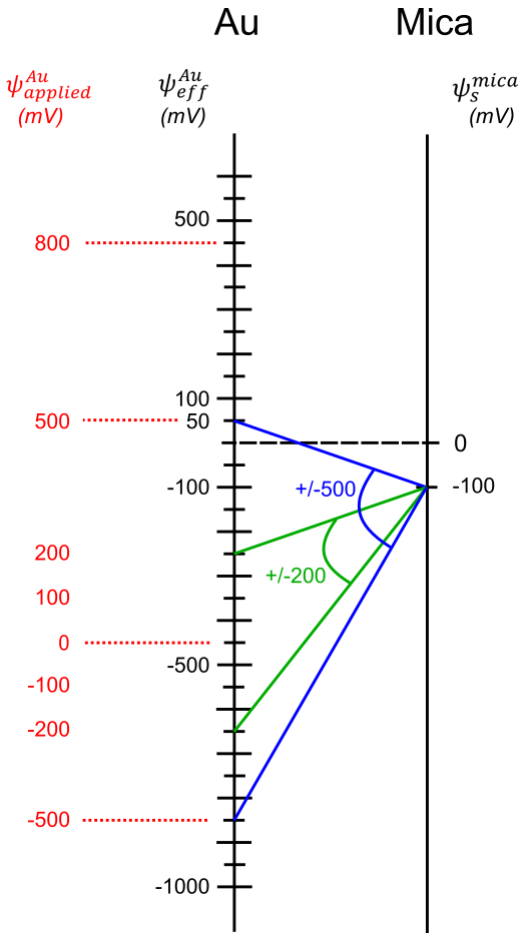


Figure 5.2: *Diagram showing the interaction between the gold surface and the mica across a dielectric. The gradient of the red and green lines correspond to the electric field between the surfaces at those applied potentials* $\psi^{Au}_{applied}$*. At* $\psi^{Au}_{applied} = \pm 200$*,* ψ^{Au}_{eff} *is being changed from -250 mV to -650 mV. The difference in gradient is not very significant. At* $\psi^{Au}_{applied} = \pm 500$*,* ψ^{Au}_{eff} *is being changed from 50 mV to -850 mV; this means that only when we get to* $\psi^{Au}_{applied} = \pm 500$ *does the field change direction when we switch voltage. The gradient changes sign, which means the ions must change orientation. This is reflected in a much more significant change in the liquid, as evidenced by Fig. 5.1 (A). This analysis correlates with the observations from Fig. 5.1 (A), and suggests that the shuffling out of a whole layer might be induced by repeatedly flipping the dipoles of the interstitial ions.*

1. Densification of the confined layer

It is well established that ionic liquids can stack in ordered layers or bilayers [26, 27, 159], and that they can adopt different anion-cation conformations depending on the shape and localisation of the ions [1, 10, 129]. For small potential gaps ($\pm$100 mV, $\pm$200 mV, $\pm$300 mV) the instantaneous electronic response to the positive potential steps is for the surfaces to attract slightly, which squeezes the layers together more tightly, effectively crushing the ions together. The response to the negative steps is to push the surfaces away from each other, allowing the ions to adopt the most favourable layering configuration.

As the steps are continued to higher gaps ($\pm$400 mV, $\pm$500 mV), the layering is increasingly disturbed by the alternating sign and magnitude of the potentials, as ions try to move to and from the charged surface. We can also see from the slope of the D vs t trace that the surfaces are moving together with some resistance, suggesting that this is unfavourable, which supports the idea that the limit of crushing ions together it being reached, which would require some ion pairs to leave the slit. It can be concluded that the disorder being induced within the system increases with increasing potential gaps, to the point where some ion pairs are gradually being squeezed out of the slit when the surfaces attract. When the first $\pm$800 mV switch is made, the attraction between the surfaces is enough to overcome the remaining barrier to excluding the equivalent of a bilayer of ions.

For the highest applied potentials ($\pm$800 mV, $+$1 V/$-$900 mV), we continue to observe that when the surfaces "squeeze in", there is some resistance, likely due to the unfavourable sterics of the ions being crushed between the surfaces. On the other hand, when the gold electrode is switched to a negative potential, the relaxation of the surfaces away from each other is instantaneous, akin to a "jump" out to a more favourable separation. In the longer steps, which are held for 60 s, we can also see that the surface

"jump" apart and then relax further out, which suggests that there is an initial electronic response causing the "jump", and then a longer-term ion response where the orientation and stacking of the molecules change to adopt a lower-energy state.

2. "Tilting" of ions

   As discussed in the introduction, there is good evidence that pyrrolidinium and TFSI ions adsorb on electrode surfaces at the PZC and change the angle of orientation when the surface potential is moved away from the PZC, so that the ions "tilt". Rivera-Rubero and Baldelli showed this adsorption through sum frequency generation vibrational spectroscopy (SFG) and cyclic voltammetry (CV) [155] and Segura *et al.* reported the structure of two IL at a mica surface, obtained by soft contact and amplitude AFM imaging [160]. The open circuit potential (OCP) of C_4C_1pyrr TFSI was measured to be $\sim$ 100 mV, but the PZC for C_4C_1pyrr TFSI at the ultra-smooth gold surface is not known, so a literature value for a rough gold electrode was used instead. Lockett *et al* measured the PZC of C_4C_1pyrr TFSI at a gold electrode to be -0.45 V vs Ag/Ag^+ [152].

   We suggest that for the lower potentials, the change in adsorption tilt is very small/negligible, and that as the potential is increased, the degree of tilt increases as well.

It can be concluded that that the "squeezes" seen in Fig. 5.1 are a combination of at least two processes. Further investigation into these mechanism though other surface force techniques and electrochemical methods would be desirable to gain better understanding of them.

Over the course of the whole cycle, the absolute separation goes from 2.6 nm to 1.8 nm, which is a total change of 0.8 nm and corresponds approximately to the thickness of a bilayer of C_4C_1pyrr TFSI measured in other works

[26]. When -800 mV is applied for the first time, we can see that although there is an immediate repulsion as the surfaces have the same sign of charge, this is quickly overcome and the surfaces move together, which suggests a change in the liquid. The absolute distance change can be interpreted as a gradual expulsion of a single bilayer. When changing the surface potential, there is an initial, nearly instantaneous electronic response, followed by a longer-timescale reorientation of the ions. With small potential steps ($\pm$100 mV, $\pm$200 mV, $\pm$300 mV), the change in surface charge can be compensated by the electronic responses and reorientation of ions, but at larger potential gaps, these are not enough to achieve equilibration. When $\pm$500 mV and $\pm$800 mV are applied, the electronic and orientational responses are not sufficient to accommodate the change in charge, so the structure of the interstitial layers is perturbed and a bilayer is gradually expelled over multiple cycles. It appears that the $\pm$500 mV cycles start a process of gradually shuffling out ion pairs of the slit, and when $+800$ mV is applied, a barrier is overcome, allowing a bilayer to be squeezed out of the slit. This can be seen when -800 mV is applied for the first time, the surfaces do not move away from each other, but continue to approach, as a bilayer is in the process of being expelled. After this, switches between positive and negative potentials result in the expected attraction/repulsion response.

A "hard wall" was observed at $\sim$ 2 nm in the force measurements in the previous chapter, and there we noted that the surfaces could not be approached past it, showing that several layers of ions were very tightly bound to the surfaces or possibly even frozen, exhibiting a solid-like response. It is possible that the rapid switching of surface potential with increasingly large potential gaps perturbs the structure of the layers, and this allows a bilayer to be gradually moved out of the slit.

From the plot of current vs time obtained during the corresponding chronoamperometric cycle (Fig. 5.3), we can also see that after the initial attraction/re-

pulsion, the separation finds its equilibrium quickly over a period of 30-60 s, and that the current drops from an initially high value back down within a few seconds of the potential being stepped. This shows that the liquid finds a new equilibrium very quickly, and that the ions reorder to screen the new surface potential within seconds of it being applied. To gain further insight into this, it is necessary to resolve how the current is decaying over the first few seconds, and we turn to chronocoulometry for this purpose.

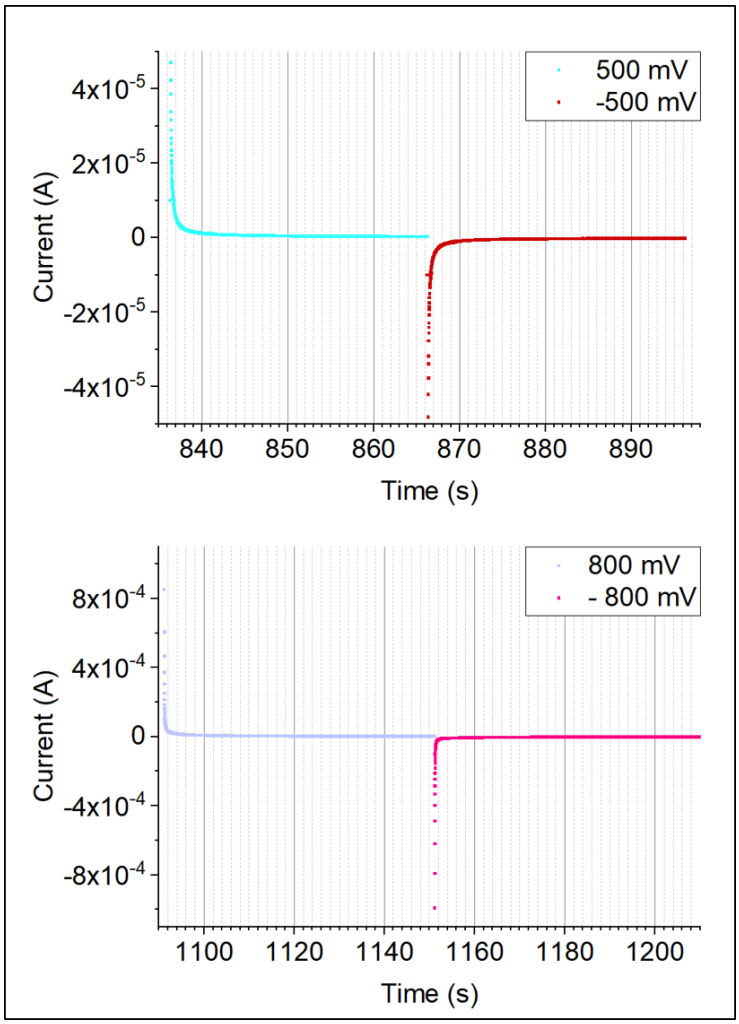


Figure 5.3: *Plots of current vs time for ±500 mV (top) and ±800 mV (bottom). For ±500 mV we can see the current decays to values below 5×10^{-6} A within 2 s of potential being changed, and for ±800 mV it drops below 1×10^{-5} A within 3 s. This means that most of the equilibriation occurs within the first few seconds of the potential being stepped, and we expect this to be the region of interest for different relaxation modes within the liquid. The longer tail of the current decay can be attributed to the minimisation of the current while the ions continue to reorder to the most favourable conformation.*

Chronocoulometry

As the chronoamperometric measurements did not have enough time-resolution, chronocoulometry was used to determine how the current and charge of the cell change in the first 5 s after stepping the potential. Here, chronocoulometry allows us to explore the current relaxation processes in C_4C_1pyrr TFSI. Since the electronic response to potential change is nearly instantaneous, chronoamperometry, which records current vs time with an interval time of 0.01 s, doesn't offer high enough time resolution to resolve the immediate response of the liquid. Coulometry records charge (*i.e.* the integral of current) vs time and samples at 0.001 s, which gives a resolution an order of magnitude higher than in chronoamperometry. This allows us to access the changes that occur almost immediately after the potential is stepped. By fitting the resulting charge decay to an exponential function, we can determine whether the overall decay is a sum of two or more exponential functions, each corresponding to a mode of relaxation.

Table 5.1: *Values returned for the best fits of the charge decays resulting from applied potentials ± 100 mV and ± 200 mV in C_4C_1pyrr TFSI.*

	Fit for +100 mV	Fit for -100 mV	Fit for + 200 mV	Fit for -200 mV
Plot	Integrated current for +100mV	Integrated current for -100mV	Integrated current for +200mV	Integrated current for -200mV
y0	2.76E-6 ± 1E-8	-2.95E-6 ± 1E-7	1.07E-5 ± 2E-7	4.85E-7 ± 9E-8
x0	9.98897	15.00442	9.98947	15.01217
A1	-2.15E-6	2.46E-6	-5.02E-6	4.30E-6
t1 [s]	0.159 ± 0.003	0.189 ± 0.002	0.379 ± 0.003	0.331 ± 0.002
A2	-9.499E-7	8.75E-7	-2.66E-6	2.17E-6
t2 [s]	0.475 ± 0.03	0.59 ± 0.04	3.17 ± --	2.82 ± --
A3	-1.976E-6	2.22E-6	-3.19E-6	2.61E-6
t3 [s]	2.49 ± 0.06	6.5 ± 0.5	3.17 ± --	2.82 ± --

Fig. 5.4 shows the charge decays immediately after potential is stepped from $+100$ mV to -100 mV and from $+200$ mV to -200 mV. Since the charging behaviour of ILs in nanoconfinement does not follow current mean-field theories [100], it was decided not to rely on any pre-existing bulk or mean-field models

to interpret the charge decay. The capacitor charging equation was not used because it treats the interstitial medium as a dielectric and does not apply to a nanoconfined IL. Instead, the purpose of the analysis of the charge decay was simply to determine whether there were two or more decay timescales - indeed Roling *et al.* have found that there are more than two in their work [98, 157]. Each decay is fitted to a function, with the best fit being a sum of three exponential decays (three-phase exponential decay):

$$y = y_0 + A1e^{(-(x-x_0)/t1)} + A2e^{(-(x-x_0)/t2)} + A3e^{(-(x-x_0)/t3)} \tag{5.5}$$

Where y is charge (measured experimentally), y_0 is initial charge (measured experimentally), x_0 is initial time (measured experimentally), x is time (measured experimentally) $A1$,$A2$ and $A3$ are amplitudes, and $t1$, $t2$ and $t3$ are the time constants for each exponential. Each exponential corresponds to a different mode of relaxation, each with a characteristic timescale, which can be rationalised by considering the three-dimensional structure of the ionic liquid's cations and anions with their localised charges and flexible chains. The values of the fits can be found in Tab. 5.1.

The first and shortest timescale, $t1$ is the immediate electronic response to the potential step. Electronic response happens very fast as there are no sterics involved, so it stands to reason that this would be the first and fastest mode of relaxation. For all four applied potentials shown in Tab. 5.1, the value of $t1$ is $<$1 s. For $\pm$100 mV, $t1$ is about 0.15 s, whereas for $\pm$200 mV $t1 \approx 0.35$ s, which is about double the time. The second timescale $t2$ can be rationalised as a conformational shift, where the asymmetric molecules reorient or distort to adopt the lowest energy conformation. For $\pm$100 mV, $t2 \approx 0.5$ s, whereas for $\pm$200 mV, $t \approx 3$ s. Once again, this can be rationalised by the potential gap being bigger: the reorientation required to equilibrate the potential change and drive the current down is greater for larger gaps, and takes more time. The third timescale $t3$ is

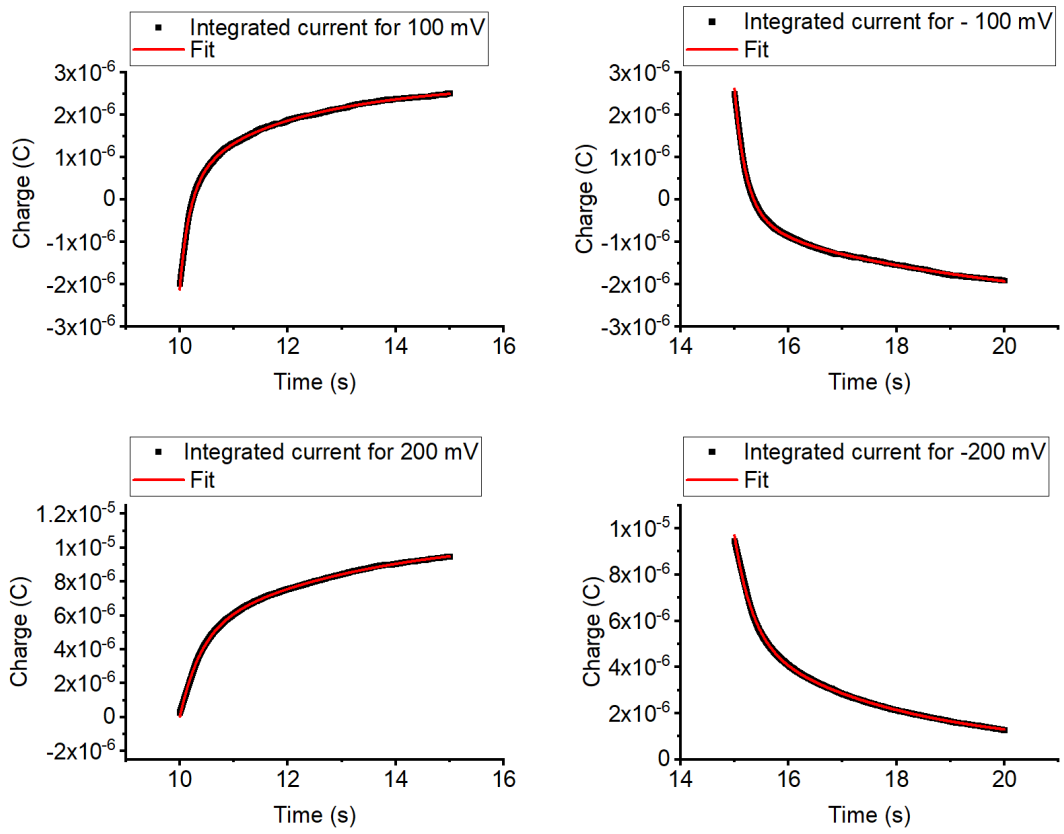


Figure 5.4: *Selected plots of charge decay vs time for C_4C_1pyrr TFSI during chonocoulometry for $\pm$100 mV and $\pm$200 mV steps, performed with surfaces in contact. The red traces are the best fits of the exponential decay of the charge. The best fit is a sum of three exponentials with three characteristic decay timescales corresponding to three relaxation methods.*

the longest, and corresponds to ions moving relative to each other to find a new equilibrium relative to the surface potential. For $\pm$100 mV and $\pm$200 mV, $t3$ is about the same, around 3 s or higher. The values for $t3$ being the same can be rationalised by the movement of ions relative to each other being dominated by steric constraints rather than the magnitude of the potential of the surfaces. These findings are in agreement with EIS results from Roling *et al.* [98, 157], which also found three distinct processes taking place at three characteristic timescales at the IL/Au(111) interface, where the IL is $Py_{1,4}FAP$.

5.4.2 Dilute Electrolyte

Control measurements were made in the same dilute electrolyte as previously, KCl (aq) 1.5 mM and 0.6 mM. As with the IL experiments, the surfaces were brought close to contact to perform the chronoamperometry and chronocoulometry. Although these measurements were made to compare the current and charge decay of a dilute electrolyte to the IL results, the control experiments also yielded results that are independently interesting.

Chronoamperometry

Potential was stepped from positive to negative values and repeated three times before moving on to the next cycle. The electrochemical window of dilute KCl (aq) is much lower than that of the IL, at about 1 V; the intervals used were $\pm$100 mV, $\pm$200 mV and $\pm$300 mV. Since OCP is high in these electrolytes (around 300-350 mV depending on the experiment), in practice the potential is being stepped from a high positive potential to a lower positive potential. The potential gap is the same, but as the PZC is not known, the absolute value of the potentials is not known.

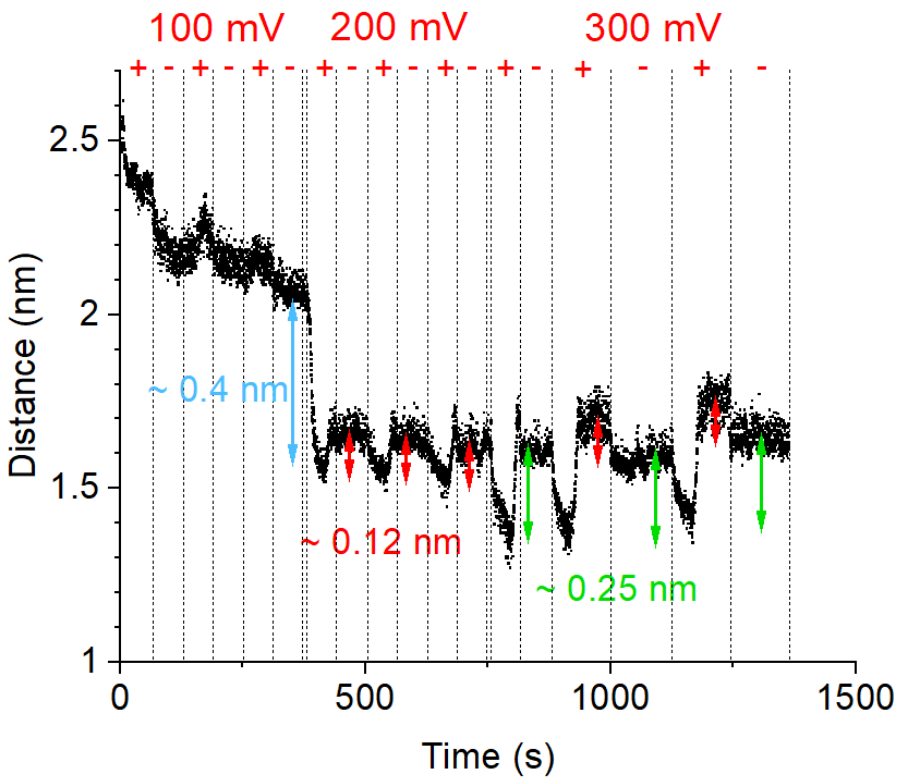


Figure 5.5: *Plot of distance vs time for a chronoamperometric cycle in KCl (aq) 1.5 mM. The applied potential is stepped from positive to negative potentials three times for each value of ±100 mV, ±200 mV and ±300 mV. The blue arrow corresponds to a distance change of ∼ 0.4 nm, interpreted as an ion layer being expelled from the slit, the red arrows (∼ 0.12 nm) are interpreted as a layer of water molecules being compressed when the surfaces attract, and the green arrows correspond to a change of ∼ 0.25 nm, interpreted as a layer of water molecules being moved in or out.*

Fig. 5.5 shows the resulting separation change during potential steps in KCl (aq) 1.5 mM. For ±100 mV intervals, there appears to be a slight response from the surface separation, but it is of ∼ 0.1 nm, with is at the limit of resolution. When switching from −100 mV to +200 mV, the surfaces move together by about 0.4 nm (blue arrow). The surfaces move away from each other before the potential is switched back to −200 mV. When switching from −200 mV to +200 mV, the surfaces come together by approximately 0.12 nm (red arrows). When switching from −300 mV to +300 mV, the surfaces move together by about 0.25 nm (green arrows). It is also noteworthy that when switching from −200 mV to +200 mV and from −300 mV to +300 mV, the surfaces move away from each other very clearly

before the potential is switched back to negative values, as seen in particular in last 4 steps at ± 300 mV, where the potential is held for longer. This is due to the EDL relaxing after the change to surface charge, which causes the force between the surfaces to decrease (lower attraction between the surfaces). The spring brings the lower surface back to its original position. This type of EDL relaxation has previously been observed by Tivony *et al.* in another dilute electrolyte (2 mM $NaNO_3$) using a similar SFB method [72].

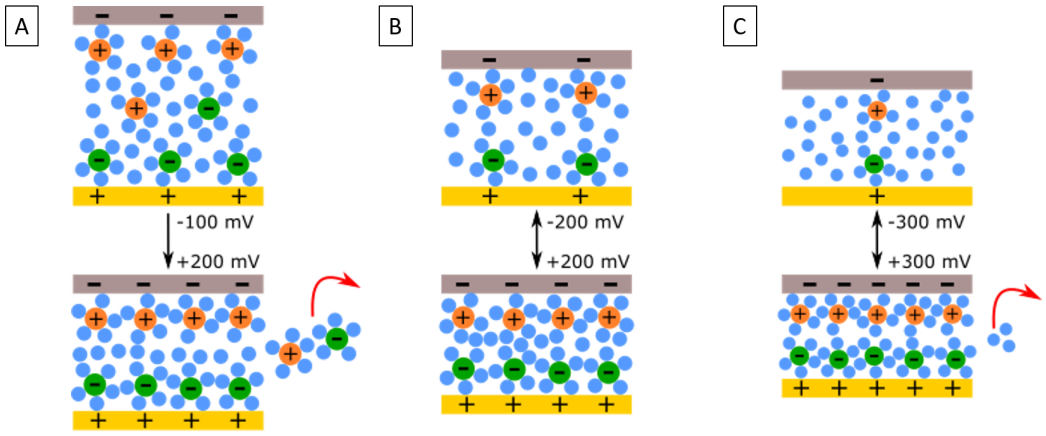


Figure 5.6: *Cartoons depicting the change in dilute electrolyte during potential steps. (A) Extrusion of a layer of ions when switching from negative to positive applied potential, e.g. the blue arrow in Fig. 5.5. (B) Compression of the interstitial layer when switching from −200 mV to +200 mV, equivalent to the compression of a layer of water molecules, e.g. the red arrows in Fig. 5.5 and 5.7. (C) Extrusion of a layer of water molecules when switching between −300 mV and −300 mV, e.g. the green arrows in Fig. 5.5 and 5.7.*

The surfaces move together by about 0.4 nm when switching from −100 mV to +200 mV (blue arrow in Fig. 5.5), which corresponds approximately to the size of a hydrated potassium ion (0.66 nm [130–133]) or that of a hydrated chloride ion (0.57 nm [132–134]). This suggests that an ion layer is being expelled from the slit when switching from −100 mV to +200 mV. The small diameter measured here can be rationalised by the hydration layer being compressed when the gold surface is positively charged.

The surfaces approach by approximately 0.12 nm when switching from

-200 mV to $+200$ mV, a separation which corresponds to about half the diameter of water [127, 128]. We suggest that the surfaces attracting compresses the water molecules in the interstitial layer, as the change in separation for the larger ± 300 mV corresponds to the diameter of a water molecule, and for the smaller potential step, the electric field might not be strong enough to extrude water molecules, only compressing them. This can be estimated with the same rough order of magnitude calculation shown above for the IL. This gives us a U^E two orders of magnitude lower than the U^{Th} for $\pm$ 200 mV if we assume the PZC of KCl (aq) to be 400 mV [145], which means the field is not strong enough to extrude water molecules.. This also supports the previous conclusion that the hydration layers of K^+ and Cl^- are compressed under -200 mV..

When switching from -300 mV to $+300$ mV, the surfaces move together by $\sim$ 0.25 nm, which is very close to the reported diameter of a water molecule (0.275 nm [127, 128]). In the steps of ± 300 mV that are held for 60s, it becomes clear that the surfaces relax away from each other before the potential is switched to -300 mV. In the trace of distance vs time, it can be seen that it takes $\sim$ 20s for the surfaces to move together by 0.25 nm, suggesting this is a sterically unfavourable process. Osmotic pressure may also resist the extrusion of the water from the slit [146]. On the other hand, whereas the EDL relaxation is much quicker, as it is due to the change of surface charge, which is instantaneous. The screening of the surface charge causes the electric field between the surfaces to become less strong, allowing the spring to restore the surfaces to their equilibrium separation. These two observations can be rationalised as follows: when surface potential is stepped from -300 mV to $+300$ mV, the surfaces experience a strong instantaneous attraction to each other, causing a layer of water molecules to be expelled from the slit. This is unfavourable sterically, so there is some resistance. Simultaneously, the EDL relaxation is occurring, and the effective charge decreases, causing the strength of the attractive electrostatic force between the surfaces to decrease. This allows a layer of water molecules

back into the gap while the surface potential remains unchanged.

When switching to -300 mV, the surfaces are attracted again, which might seem counter-intuitive. Since the PZC is not known, it is not possible to determine with certainty why this is, but it is possible that the effective potential of the gold surface is being switched from a high positive value to a lower positive value *after* the system has equilibrated. As the charge distribution is being changed again, the system must equilibrate again, so the surfaces experience a small attraction, which quickly relaxes back to equilibrium.

Fig. 5.7 shows similar behaviour in the more dilute system of KCl (aq) 0.6 mM. Switching between $+100$ mV and -100 mV shows no response, likely because it is lost in the background noise. When switching from -100 mV to $+200$ mV, the surfaces come together by about 0.26 nm. Switching between $+200$ mV and -200 mV results in squeezes in and out of about 0.15 nm and the -300 mV to $+300$ mV steps result in the surfaces approaching by $\sim$ 0.29 nm. In the ± 200 and ± 300 mV steps, the surface attraction is gradual, taking place over the whole length of time during which the potential is held. This suggests that the compression of water is disfavourable, as the molecules are compressed between the surfaces when they attract.

The surfaces come together by about 0.26 nm when switching from -100 mV to $+200$ mV, a separation that corresponds to the thickness of a layer of water molecules being expelled from the slit. Switching between -200 mV and $+200$ mV results in the surfaces moving together by about 0.15 nm, which we interpret as water molecules being compressed between the surfaces without being expelled from the slit. The approach of the surfaces by 0.15 nm takes place over 30s, which suggests that there is steric and osmotic resistance to them moving towards each other. The near-instantaneous response of the surface moving apart can be explained by the relaxation of the compressed liquid being a favourable process.

The -300 mV to $+300$ mV steps result in the surfaces approaching by $\sim$ 0.29 nm, which suggests a layer of water molecules is being squeezed out of the slit. As with the ± 200 mV steps, the surfaces move together with some resistance from the interstitial liquid, and move apart immediately when a negative potential is applied. This is in agreement with the compression and expulsion of a layer of water molecules being unfavourable as it is a process that requires the attractive force between the surfaces to overcome the osmotic pressure of the water in the slit. The EDL relaxation causes the field to weaken, which allows the spring to return the surfaces to the initial separation, creating a cavity that allows the water back in.

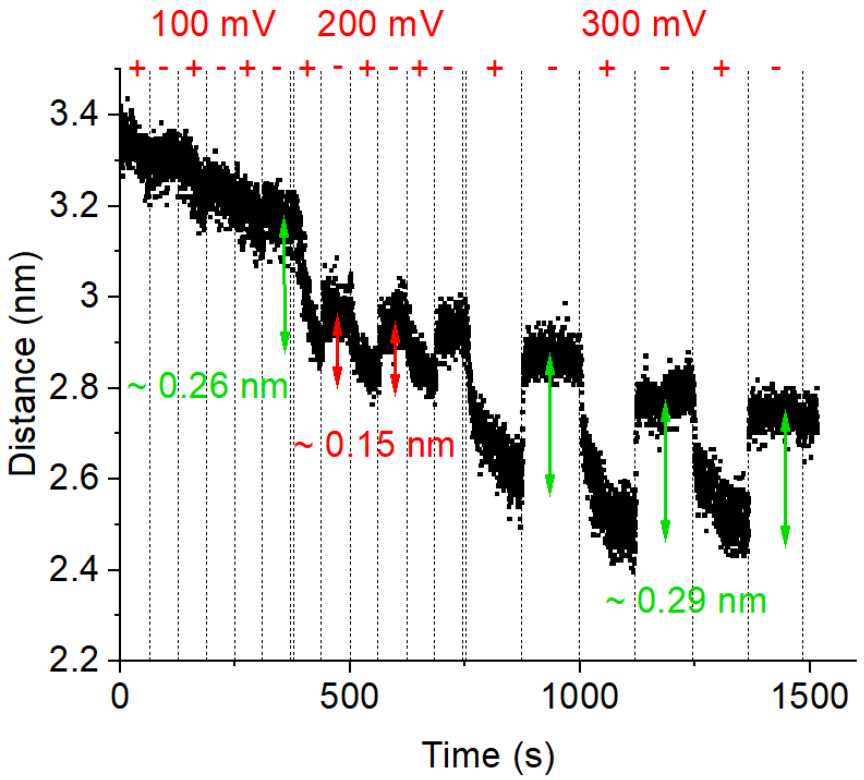


Figure 5.7: *Plot of distance vs time for a chronoamperometric cycle in KCl (aq) 0.6 mM. The applied potential is stepped from positive to negative potentials three times for each of ± 100 mV, ± 200 mV and ± 300 mV. The green arrows correspond to a distance change of about 0.26 – 0.29 nm, interpreted as a layer of water molecules being moved out. The red arrows indicate a distance change of $\sim$ 0.15 nm, which is interpreted as water molecules being compressed when the surfaces attract, and relaxing back to equilibrium when the surfaces move away from each other.It is noteworthy that EDL relaxation is not observed here.*

Looking back on the structural forces seen in Ch. 4 in KCl (aq) 0.6 mM, we saw similar dimensions for the layering: $\sim$ 0.4 nm for the larger steps, which we interpreted as KCl ion layers, and $\sim$ 0.15 – 0.2 nm for the smaller ones, which we interpreted as the compression of water molecules. The agreement between the dimensions shows that the results from the force profiles and the chronoamperometry match up well. Theses measurements also speak to the excellent resolution of the gold/mica setup, as it can resolve changes as small as half the diameter of water. This is a good demonstration of the versatility of the measurements made possible by the improvements to the setup.

Chronocoulometry

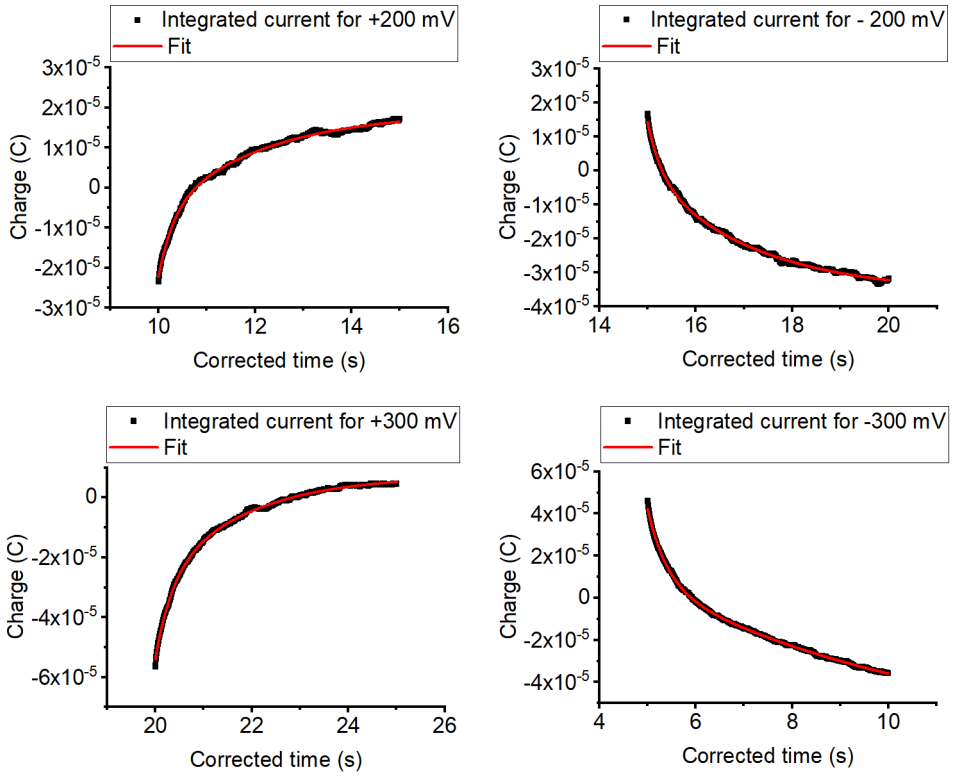


Figure 5.8: *Selected plots of charge decay vs time for KCl (aq) 1.5 mM. The red traces correspond to the best fit, which is a sum of two exponentials that reflect the different relaxation modes that occur as the electrolyte responds to the potential applied to the surface.*

Chronocoulometry was performed in KCl (aq) 1.5 mM to have a control

experiment against which to compare the results of chronocoulometry in C_4C_1pyrr TFSI. Fig. 5.8 shows the charge decay immediately after the surface potential is changed, with steps of $\pm$100 mV, $\pm$200 mV and $\pm$300 mV, with the red trace representing the best-fit exponential. As expected, and in contrast to the IL system, the equation for the best fit is a sum of two exponentials:

$$y = y_0 + A1e^{(-(x-x_0)/t1)} + A2e^{(-(x-x_0)/t2)} \tag{5.6}$$

This can easily be rationalised as two different relaxation processes, one for the electronic response, the other for the ions moving in the liquid to balance out the new surface potential.

Comparing the IL and dilute KCl (aq) data from Tab. 5.1 and 5.2, we can see that the timescales for the near-instantaneous electronic response $t1$ are similar, between 0.2–0.4 s, which can be rationalised by the electronic response being unhindered by the shape or sterics of the ions. The second timescale for dilute KCl (aq) $t2$ has similar values for $\pm$200 mV and $\pm$300 mV, about 2 s. This corresponds to ions moving in the liquid to minimise charge, so this timescale will be limited by the time it takes for ions to move past solvent molecules and each other. It can be compared to $t3$ for the IL, which has values averaging 3 s, slightly longer. It is noteworthy that the timescales corresponding to the ions moving in the liquid are similar, showing that the sterical hindrance in both liquids is similar.

The amplitudes also provide an interesting measure of the difference between the two liquids; we consider the exponential current decays for $\pm$200 mV in IL and dilute KCl (aq). The amplitude for the first exponential decay $A1$ is an order of magnitude smaller for the IL: approximately $\pm5\times10^{-6}$ vs $\pm1.5\times10^{-5}$ for KCl (aq). The same observation is true when comparing $A3 = \pm3 \times 10^{-6}$ for the IL and $A2 = \pm3 \times 10^{-5}$ for KCl (aq). This can be explained by the ion density at the surface being higher in the IL case, so the amplitude is smaller than in the dilute electrolyte.

Table 5.2: *Values returned for the best fits of the charge decays resulting from applied potentials ±200 mV and ±300 mV in 1.5 mM KCl (aq).*

	Fit for +200mV	Fit for -200mV	Fit for +300mV	Fit for -300mV
Plot	Integrated current for +200mV	Integrated current for -200mV	Integrated current for +300mV	Integrated current for -300mV
y0	1.90E-5 ± 1E-7	-3.61E-5 ± 9E-8	7.36E-6 ± 6E-8	-7.01E-5 ± 8E-7
x0	10.01188	15.02012	20.0061	5.15186
A1	-1.57E-5	1.447E-5	-2.5E-5	2.5E-5
t1 [s]	0.310 ± 0.006	0.292 ± 0.005	0.331 ± 0.004	0.407 ± 0.003
A2	-2.50E-5	3.48E-5	-3.6E-5	7.49E-5
t2 [s]	2.18 ± 0.03	2.23 ± 0.02	1.765 ± 0.015	6.1 ± 0.1

5.5 Conclusion

Chronoamperometry and chronocoulometry was performed on C_4C_1pyrr TFSI and on dilute KCl (aq) solutions confined to $<$5 nm.

Chronoamperometry on the IL showed that switching potentials with increasing gaps results in a distance change that is smaller than the size of a bilayer or the diameter single cation/anion. For small potential gaps, the change is small, and it increases with larger gaps. We suggest that this due to a combination of adsorption, electronic, steric and conformational changes induced by the change in surface charge. Chronocoulometry reveals three different decay exponentials, each with a characteristic timescale corresponding to the different modes of relaxation in the liquid.

Chronoamperometry on the dilute KCl (aq) solutions showed that depending on the size of the potential gap, water molecules and hydrated ions can be compressed or squeezed in and out of the slit. Chronocoulometry confirms that there are two exponential decay processes with two characteristic timescales.

There are very few theories established to model the charging dynamics of ionic liquids in nanoconfinement, and virtually no measurements studying them

[100]. We put these results forwards as a small building block towards better understanding the field. There is a lot to be explored, and going forward it would be interesting to repeat these measurements in different ionic liquids and at more potential intervals. There is also work ongoing in our group on performing EIS and capacitance measurements on ionic liquids.

Chapter 6

Results from the Au3 SFB Setup: Underscreening

6.1 Au3 SFB: Experimental Results and Discussion

The Au3 SFB was first put to work experimentally to measure simple force profiles, with the aim to observe the effect of varying surface electrochemical potential on the forces in the liquid. Of particular interest was underscreening in concentrated electrolytes, which had been theorised to be purely an effect of the liquid [22], with the characteristic screening length unchanged by surface potential. A symmetric gold/gold setup is desirable as both substrates are identical and symmetric and the applied potential is the same on each, which substantially simplifies the interpretation of results. The ionic liquid was chosen for these measurements based was 1-butyl-1-methylpyrrolidinium bis(trifluoromethanesulfonyl)imide (C_4C_1pyrr TFSI), which has been used in several studies investigating underscreening in mica/mica setups [22, 25, 26]. It has wide electrochemical window allows for a large range of applied potentials.

6.1.1 Materials and Methods

Experiments were prepared by stripping the mica off the gold surfaces, loading the lenses into the SFB and immediately injecting the IL, which had been dried on a Schlenk line overnight (5×10^{-3} mbar, 60° C). The chamber was sealed and purged with nitrogen gas for 20 min and P_2O_5 was placed inside to absorb remaining atmospheric water.

All glassware was sonicated in chloroform (twice), toluene, isopropanol and ethanol, rinsed in ultrapure water and cleaned in piranha solution (3:1 concentrated sulfuric acid 99% : hydrogen peroxide 30%). All tools and stainless steel parts were sonicated in chloroform (twice), toluene, isopropanol and ethanol, rinsed in ultrapure water and cleaned in nitric acid solution (2:1 water : nitric acid 70%). The syringe used for injecting the IL, the electrode wires, the clamps and the screws were cleaned by sonication in chloroform (twice), toluene, isopropanol and ethanol.

6.1.2 Underscreening

Fig. 6.1 (A) shows force profiles at $+100$ mV and $+500$ mV, and (B) shows a force profile at $+200$ mV where contact is not clean, but screening length is measured. The potentials were applied at ~ 1 μm separation and the current was left to settle for 20 min before the force profiles were measured. This wait time was determined empirically to ensure that the force profiles were performed at equilibrium. In Fig. 6.1 (A), the surfaces do not come into contact at 0 nm, but reach a "hard wall" between 5 – 6 nm beyond which approach was no longer possible. All three force profiles have a long-range tail that appears to decay exponentially. The insets show applied potential and corresponding screening lengths, which were measured by fitting the long-range tail. No change in screening length was observed with changing surface potential, and no change in the

magnitude of the forces was observed either.

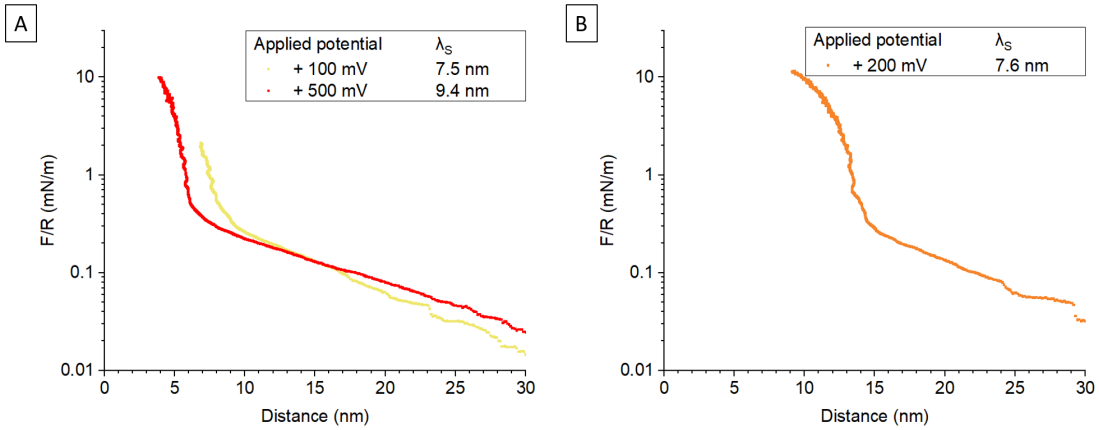


Figure 6.1: *Force profiles of C_4C_1pyrr TFSI with applied potentials. (A) The clean force profiles at +100 mV and +500 mV show a "hard wall" at 5 – 6 nm separation. Screening lengths, which are interpreted as underscreening, are noted in the legend and do not change significantly with applied potential. It can also be noted that the magnitude for the force does not vary with potential. (B) The force profile at +200 mV doesn't have clean contact but screening length could still be obtained, and is very close to that of +100 mV. Due to difficulties in measurements, each force profile was measured at a different contact spot, so there is variability in the position of the "hard wall".*

As mentioned previously, the long-range screening length of C_4C_1pyrr TFSI has been measured to be $\sim$ 6 – 9 nm and it was hypothesised that this length is independent of surface charge [22]. The most thorough way to verify this is to measure force profiles with both confining surfaces under identical applied potentials. In these force profiles, a long-ranged tail appears to decay exponentially; this is interpreted as underscreening. Both in Fig. 6.1 (A) and (B), the screening lengths are measured to be between 7.5 and 9.4 nm, which is within the expected error. It can be seen that there is no change in screening length with surface potential, as is the case in the gold/mica measurements reported in Ch. 4.

It can also be observed from Fig. 6.1 (A) and (B) that there is no change in the magnitude of the screening length, which was unexpected. Following DLVO theory, the electrostatic contribution would be expected to be affected by ap-

plied potential, and for the magnitude of the repulsion between the surfaces to increase with increasing potential gaps, but again this was not observed to be the case. This observation backs up the one made in the equivalent measurements in gold/mica SFB, and shows that the surface potential is strongly screened by the near-surface layers, resulting in an effective surface charge that is not appreciably affected by changes in the surface potential. It means that the liquid determines effective surface charge.

Additionally, the surfaces never came into contact in ionic liquid, with a strong repulsion between the surfaces, or "hard wall", at $\sim 5 - 6$ nm for the clean experiments (*cf.* Fig. 6.1). This "hard wall" could not be overcome with our apparatus, and the remaining interstitial layers could not be expelled from the slit. The thickness corresponds in C_4C_1pyrr TFSI to about $10 - 12$ ion layers, or $5 - 6$ bilayers [26]. This wall was observed at all applied potentials, and across all clean experiments. We suggest that one of two phenomena explain this: the Stern layer or capillary freezing, both of which are discussed in Ch. 4. The presence of this effect in a symmetric system, and the fact that the "hard wall" in Au3 SFB was observed at about twice the distance of the one in the gold/mica SFB is quite interesting: it suggests that each surface has its own bound/"frozen" layers, and thus that the "freezing" of these layers is indeed related to the metallic nature of the confining surfaces. To verify whether the freezing is confinement-induced, it would be interesting to use AFM and shearing in SFB.

Comtet *et al.* showed in 2017 that the threshold confinement for capillary freezing increases with increasing metallic nature of the surface [136]. In their experiment, they used a tungsten tip in AFM, and observed the largest separation for capillary freezing against platinum. The experiments reported in this paper have several other key differences: they use a different IL (Bmim BF_4), which has a much lower melting point than C4C1pyrr TFSI. The melting point of Bmim BF_4 is -70 C [136], whereas the melting point of C4C1pyrr TFSI is -6 C . Additionally, the

measurements done by Comtet et al. were performed in vacuum, whereas the measurements reported in this thesis were done at atmosphere, and we expect solvated water, even in small quantities, to affect this effect [27]. In the experiments presented above, the distance of the "hard wall" was observed to increase when increasing the number of metallic confining surfaces. In these measurements, it is not possible to distinguish whether the metallic surfaces each have a "wetting layer" of bound ions at all separations, which are being probed when the surfaces come into contact, or whether this is a confinement-induced effect, where the critical confinement λ_C increases with increasing metallic nature of the confining surfaces. Whether considering the strongly-bound layer theory or the capillary freezing theory, we suggest that the separation of the "hard wall" in Au3 is twice that in gold/mica because both surfaces are metallic, which means that the effect is twice as great.

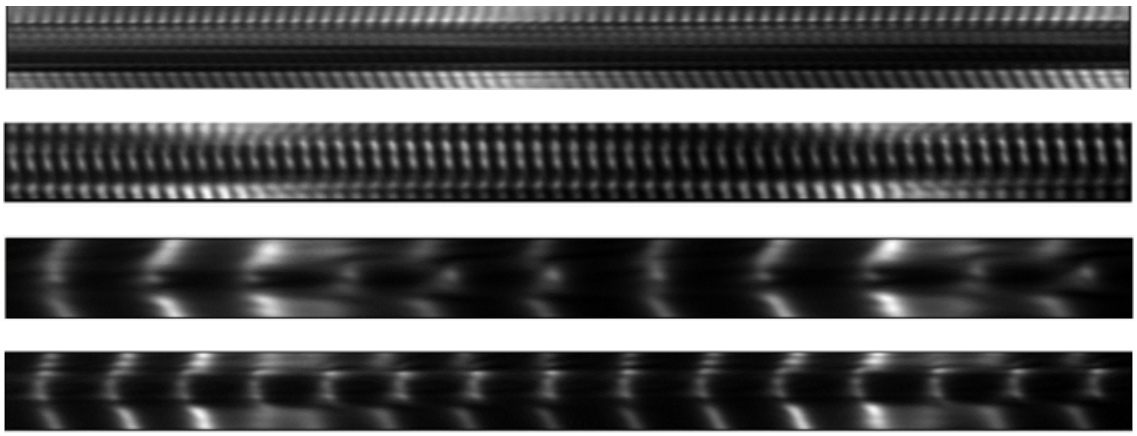


Figure 6.2: *FECO after separating the surfaces. In dilute electrolytes, the surfaces weld and separating them strips some or all of the gold on one or both of the contact points of the lenses. Several solvents and electrolytes were tried, and these images are from four different spots across three experiments in dilute lithium chloride ($\sim$ 1 mM) in ethylene glycol. Because of this, no control experiments in dilute electrolytes were achieved.*

As this is a contact-free calibration there is a level of uncertainty as to the accuracy of the calibration of the separation of the surfaces. However, when control experiments were attempted in dilute electrolytes (KCl (aq), C_4C_1pyrr TFSI in ethylene glycol, LiCl in ethylene glycol), the surfaces jumped together when van der Waals forces took over and welded at a separation of 0 nm (see Fig. 6.3),

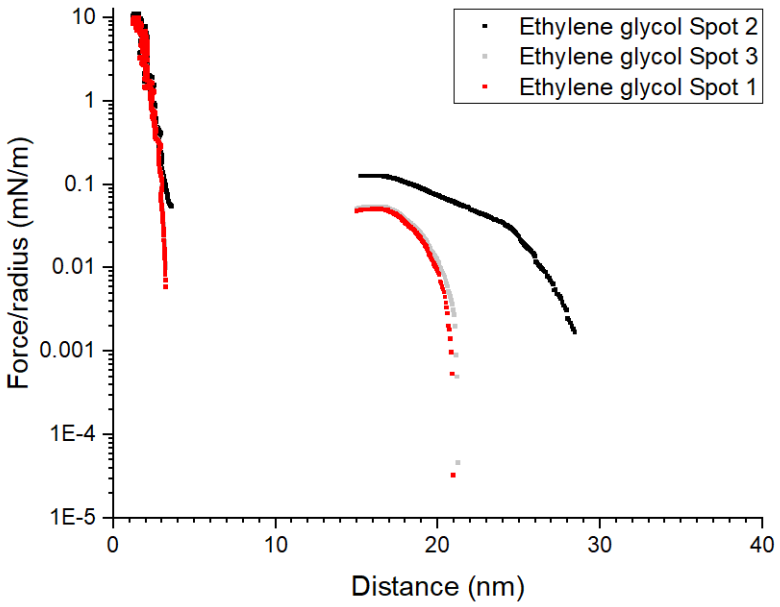


Figure 6.3: *Examples of force profiles in ethylene glycol, where the first approach was recorded. After each of these approaches, the two gold surfaces welded and the surfaces were destroyed when separating the lenses, as one of the two gold layers was stripped from the epoxy layer glueing it to the lens.*

demonstrating that surface roughness was not the issue, and that the multi-matrix method is able to accurately measure separation down to 0 nm. However, this also meant that it was not possible to make control measurements in dilute electrolytes, as the welding of the surfaces destroyed the point of closest approach, often stripping the gold from one of the lenses when they were separated. FECO of damaged lenses are shown in Fig. 6.2.

The adhesion between the gold surfaces cannot be estimated from these measurements, as the two gold surfaces weld when they come into contact and when separating the lenses, it is the epoxy/gold interface that ruptures. This can be seen in Fig. 6.2, which shows the FECO after the destruction of the surfaces, and could also be seen when inspecting the lenses visually after the experiment. After the welding, no interface exists between the two gold surfaces, and the tear is irregular, so cannot be quantified.

Examples of first-approach force profiles in ethylene glycol are shown in Fig. 6.3. Two gold surfaces have the same surface potential, so if we consider them in the context of two surfaces at constant potential and the special case of two identical surfaces, we expect repulsive forces to be present [78]. It can be seen that the surfaces to jump into adhesive contact when they reach a critical separation, which can be interpreted as van der Waals forces becoming dominant.

6.1.3 Comparing Results From Three SFB Setups

This thesis has presented results from two electrochemical setups; here we compare the force profiles obtained with these to a typical mica/mica SFB force profile. Fig. 6.4 shows three force profiles: (A) was taken in a mica/mica setup, (B) was taken in the gold/mica setup and (C) was taken in Au3 SFB. All three are force profiles in $C_4C1pyrr$ TFSI, and (B) and (C) were taken with an applied potential of $+500$ mV. The mica/mica force profile (Fig. 6.4 (A)) shows that the surfaces come into contact at a separation of $D_{min} = 1$ nm, as well as steps characteristic of structural forces between 5 – 1 nm and a screening length $\lambda_S = 8$ nm. Approximately 4 layers are seen in this force profile. The gold/mica force profile (Fig. 6.4 (B)) shows $D_{min} = 2$ nm, layers between 5 – 2 nm and a screening length of $\lambda_S = 7$ nm. Fewer layers are seen in (B) than in (A), with only two distinct steps. The Au3 SFB force profile (Fig. 6.4 (C)) shows $D_{min} = 4$ nm, no apparent layers and a screening length of $\lambda_S = 9$ nm.

The value of D_{min} in the mica/mica force profile can be explained by the final bilayer of ionic liquid not being expelled from the slit, which is normal in mica/mica experiments [9, 26]. In the gold/mica force profile, D_{min} is larger, corresponding to several bilayers, which were interpreted as layers “frozen” in place by capillary freezing or a metal-induced surface effect. This was unexpected, as

the surfaces are oppositely charged and were expected to come into adhesive contact. Instead, the “hard wall” was reached at 2 nm could not be overcome with the apparatus. A similar “hard wall” was seen in the force profile in Au3 SFB at 4 nm, which suggests that the thickness of the “hard wall” is due to the ionic liquid forming a solid-like layer on the metal surfaces. It is not possible to determine from these measurements whether this effect is confinement-induced (as reported for capillary freezing by Comtet *et al.* [136]) or present at all separations.

Structural forces are seen in Fig. 6.4 (A) and (B). The mica/mica setup (A) has much smoother surfaces with two surfaces of 0.034 nm RMS roughness when compared to the gold/mica setup, which has one mica surface (0.034 nm RMS roughness) and one gold surface (0.1 nm estimated roughness). This means that more layers are seen in the mica/mica setup as the surfaces are smoother. No structural forces are seen with Au3 SFB, as although the gold surfaces are very smooth, it is not enough to see structural forces.

The screening lengths are all of similar values, and are not changed when applying a potential to the surface(s) with gold/mica or Au3 SFB. The values for λ_S are between 7 – 9 nm, which is within the error expected for screening lengths in SFB. These values are consistent with the literature [22].

This comparison shows that both electrochemical setups show excellent agreement with the mica/mica setup for screening lengths, and that the gold/mica SFB has excellent resolution. It is clear that the “hard walls” seen in the electrochemical setups are a manifestation of the unusual interaction of the ionic liquid with the gold substrate. It can be seen that the gold/mica setup used here harnesses high resolution and electrochemistry, and is a valuable tool for surface force experiments. The Au3 SFB setup shows promise despite having lower resolution, and demonstrated the type of measurement that can be realised with it.

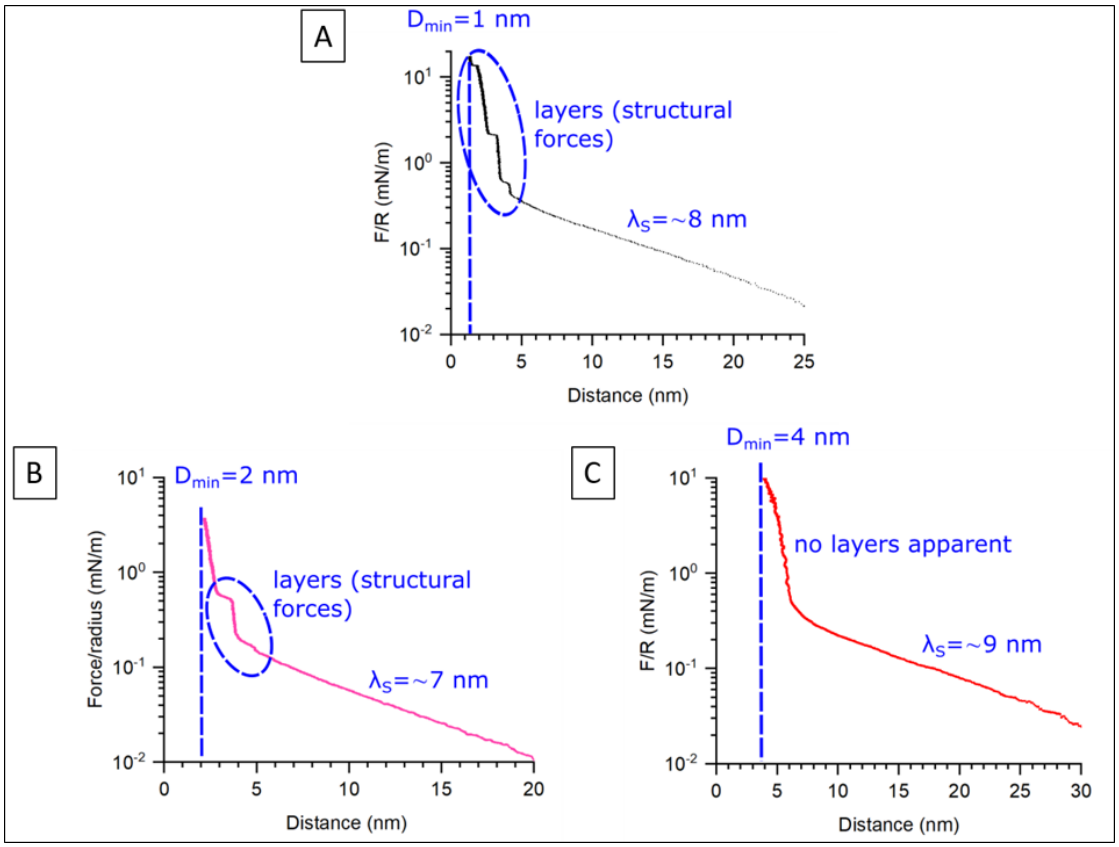


Figure 6.4: *Force profiles in C_4C_1pyrr TFSI from a mica/mica SFB setup (A), the gold/mica SFB setup (B) and the Au3 SFB setup (C). The force profiles in (B) and (C) were measured at +500 mV. The distances of closest approach are $D_{min} = 1$ nm for (A), $D_{min} = 2$ nm for (B) and $D_{min} = 4$ nm for (C). The large D_{min} for (B) and (C) are interpreted as being caused by the formation of solid-like layers on the metal surfaces. Layers are seen in (A) and (B), indicative of the presence of structural forces. All three force profiles show an exponentially decaying force in the 30 – 5 nm range, which is interpreted as underscreening. The screening lengths are of similar values, with $\lambda_S = 8$ nm for (A), $\lambda_S = 7$ for (B) and $\lambda_S = 9$ nm for (C).*

6.2 Conclusion

A mica-free, 3-mirror electrochemical gold/gold SFB setup was developed using template-stripping methods and contact-free calibration via the multi-matrix method, and was successfully used to measure force profiles. The first measurements performed in this setup demonstrated that screening length is not changed by applying potentials to the confining surfaces. It was also observed

that the magnitude of the forces measured does not change with applied potential, which goes against expectations based on DLVO theory and suggests that surface charge is independent of surface potential. A “hard wall” was observed at a separation of 5 – 6 nm, twice the thickness of the “hard walls” seen in equivalent gold/mica measurements, suggesting that the phenomenon causing this occurs at the metal surface and that it is twice as large in Au3 SFB because it uses two metallic surfaces, against gold/mica’s single one. These results demonstrate that Au3 SFB has a lot of promise for electrochemical and surface force measurements. However, several factors prevent it from becoming a popular EC SFB setup.

Firstly, learning how to make the lenses of a quality that is high enough for a successful experiment is a particularly lengthy process, even by SFB standards. It is vital to be able to reliably produce lenses with smooth, 2-fringe secondaries, otherwise analysis of the data becomes impossible.

Secondly, the experimental setup itself is also difficult to execute, as the number of wires significantly increases the risk of mechanical coupling, but even mechanically sound setups also have a high failure rate compared to classic SFB, with approximately one in ten experiments being clean. Gold surfaces are prone to contamination, and the surfaces are easily scratched or damaged during preparation and experiments. Unlike with mica surfaces, there is very little margin for error with gold surfaces – the lightest contact with another hard surface or the slightest lateral motion when the surfaces are in contact can damage the point of closest approach beyond being usable.

Finally, in the process of trying to make control measurements in Au3 SFB, it became clear that it is not suitable for pure solvent or low concentration salt solutions. All attempts to make force measurements in propylene carbonate, ethylene glycol and water, all of which were tried pure and doped with low concentrations of KCl or C_4C_1pyrr TFSI, resulted in cold welding and destruction of

one or both of the surfaces upon first approach. Due to the solubility of EPON glue in a number of conventional solvents, viable options for suitable solvents that are also electrochemically relevant are thin on the ground. To resolve this issue, it would be necessary to use another type of glue, but this option was explored in depth by previous group members in regards to classic SFB experiments, and they found that there are very few viable alternatives to EPON, and none that would suit the fabrication process of Au3 SFB. Even if there were a suitable option, it would not bypass the problem of the welding. In light of this, it is likely that Au3 SFB may only be suitable for measurements in IL, where the large, flexible ions protect the surface. It is also possible that measurements in solutions with high salt concentrations may be achievable, but this remains to be tested.

Beyond the experimental aspects, the analysis is an especially difficult step, where any unusual optics can derail the processing of the data, rendering it impossible to analyse even if the experiment itself was clean. In particular, irregular or off-vertical secondary fringes and spectra with more than two secondary fringes have proven extremely difficult or outright impossible to fit.

In summary, Au3 SFB is an equally promising and challenging electrochemical setup, which holds a lot of potential but currently suffers from a number of technical and analytical drawbacks that keep it from being adopted more widely for electrochemical SFB measurements.

Statement of Authorship for joint/multi-authored papers for PGR thesis

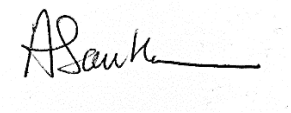
To appear at the end of each thesis chapter submitted as an article/paper

2586

The statement shall describe the candidate's and co-authors' independent research contributions in the thesis publications. For each publication there should exist a complete statement that is to be filled out and signed by the candidate and supervisor **(only required where there isn't already a statement of contribution within the paper itself).**

Title of Paper	A 3-mirror surface force balance for the investigation of fluids confined to nanoscale films between two ultra-smooth polarizable electrodes.
Publication Status	X Published □ Accepted for Publication □Submitted for Publication □Unpublished and unsubmitted work written in a manuscript style
Publication Details	Van Engers, C. D., Balabajew, M., Southam, A., & Perkin, S. (2018). *Review of Scientific Instruments*, *89*(12). https://doi.org/10.1063/1.5045485

Student Confirmation

Student Name:	Astrid Southam		
Contribution to the Paper	Performed proof-of-concept measurements with Dr. Balabajew, contributed to the fabrication process of the lenses, wrote part of the manuscript.		
Signature 		Date	09/06/2022

Supervisor Confirmation

By signing the Statement of Authorship, you are certifying that the candidate made a substantial contribution to the publication, and that the description described above is accurate.

Supervisor name and title: Prof. Susan Perkin		
Supervisor comments I approve the above statement of contribution to this collaborative project.		
Signature. 	Date	16.Jun.2022

This completed form should be included in the thesis, at the end of the relevant chapter.

Chapter 7

Conclusion

The aim of this thesis was to develop surface force balance (SFB) setups that allowed one or both of the surfaces to be potential-controlled, so that the influence of applied potential on surface forces could be explored and so electrochemical methods could be used to study electrolytes. Two setups were described: an improved asymmetric gold/mica SFB setup (gold/mica SFB), based on previous work in other research groups and which has one polarizable surface, and a triple gold mirror, which was proposed by van Engers *et al* in 2018 [45] and has two polarizable surfaces (Au3 SFB). Both were successfully used to obtain results and these were reported in this work in Ch. 4, 5 and 6.

The gold/mica setup and its preparation are presented in Ch. 3, along with the important modifications to the fabrication of the lenses that afforded significantly improved resolution. In particular, it was found that slow, controlled evaporation rates of gold on mica for templating yields extremely smooth polycrystalline surfaces that consistently give high enough resolution to see structural forces in the ionic liquid (IL) 1-butyl-1-methylpyrrolidinium bis(trifluoromethanesulfonyl)imide (C_4C_1pyrr TFSI) and in dilute KCl (aq). The resolution of absolute distance between the surfaces is of $\pm$ 0.1 nm, which, to our knowledge, has not been achieved in other gold/mica SFB setups. The experimental results obtained

with the gold/mica setup are discussed in Ch. 4 and 5.

Ch. 4 sought to investigate the effect of applied potentials on normal surface forces in IL and compare it to control experiments in dilute KCl (aq) solutions (1.5 and 0.6 mM). Of particular interest is the effect of applied potential on the unusual long-range screening length observed in concentrated electrolytes and ILs, termed "underscreening" [22–24]. Previous work in mica/mica SFB setups hypothesised that underscreening is dependent only on the Bjerrum length, ion concentration and ion radius, implying that it is independent of surface potential [22]. In the present work, force profiles are measured at a range of applied potentials ($\pm$800 mV) within the stable electrochemical window of C_4C_1pyrr TFSI, and no change in screening length is observed, confirming that underscreening is not affected by surface potential. Additionally, the magnitude of the screening lengths does not scale with the sign and magnitude of the applied potentials, which goes against predictions based on DLVO theory. This suggests that effective surface charge is determined by the liquid and independent of applied potential. Finally, a "hard wall" was observed at a surface separation of 2 nm, beyond which approach was not possible. The solid-like behaviour of this contact despite the remaining interstitial ions suggests that this may be caused by capillary freezing, a recently reported phenomenon where an ionic liquid exhibits properties of a frozen solid when confined between metal surfaces to a critical separation [20, 136]. The force profiles all show steps characteristic of molecular layering (structural forces), which require atomically smooth confining surfaces, and to our knowledge is the first report of this level of resolution in a gold/mica SFB.

Control measurements in dilute KCl (aq) confirm that the "hard wall" is particular to the interfacial behaviour of the IL, and force profiles show typical DLVO behaviour with a Hamaker constant of 8.5×10^{-20} J, which is in agreement with other works [54, 58, 88], and a jump-in of 7.5 nm. In the force profiles in

KCl (aq) 0.6 mM, molecular layering was observed, with large steps of $\sim$ 0.4 corresponding to the expulsion of a layer of hydrated ions and smaller steps of $\sim$ 0.2 nm corresponding to the compression and expulsion of a layer of water molecules. Structural forces were observed from $\sim$ 4 nm at positive potentials and $\sim$ 2 nm at negative potentials. To our knowledge, this has not been reported in any other works using a gold/mica setup, and is also rarely seen in mica/mica setups despite the higher resolution afforded by using two mica surfaces.

Ch. 5 continued the investigation of C_4C_1pyrr TFSI under potential control with two types of potential-step methods: chronoamperometry and chronocoulometry. A chronoamperometric cycle was applied within the stable electrochemical window and at a surface separation of 2.6 nm, and the plot of surface separation vs time showed the gradual expulsion of the equivalent of a layer of ions was observed over the course of this cycle. It was suggested that this was due to the continuous disruption of the interstitial ion layers by the potential steps, in particular the larger ones ($\pm$500 mV, $\pm$800 mV, $+1$ V/$-$900 mV). The steps at $\pm$800 mV and $+1$ V/$-$900 showed that the compression of the interstitial layers is unfavourable and the relaxation of the surfaces away from each other is more favourable, which supports the hypothesis that the confined layer exhibits solid-like behaviour when confined to 2 nm surface separation. Two processes were proposed to explain the mechanism of expulsion: densification of the confined layer and tilting of ions, both of which have been observed in other works [155, 160]. The plot of current vs time shows that the current relaxation after the potential is stepped occurs very rapidly, dropping down to equilibrium values within 2 – 3 s, even for the larger steps. Chronocoulometry was used to resolve this short timescale and the modes of decay. The analysis of plots of charge vs time revealed that the decay is a sum of three exponentials, each with a characteristic timescale and amplitude. The initial and fastest timescale is attributed to the near-instantaneous electronic response, the second to the tilting of ions (conformational shift) and the third and longest to the movement of ions within the slit,

a process limited by the time needed for ions to pass each other in nanoconfinement. This is in agreement with previous works by Roling *et al*, which also reported three timescales for the ionic liquid [98, 157]. The amplitudes do not change significantly between the different applied potentials, which is in agreement with the absence of changes in magnitude of the force profiles measured in Ch. 4.

The control experiments performed in dilute KCl (aq) revealed interesting results independently of the C_4C_1pyrr TFSI measurements. Both in the 1.5 mM and 0.6 mM dilutions, the chronoamperometric cycle was performed between -300 and $+300$ mV, which is within the stable electrochemical window, and the surface separation at the start of the cycle was at 2.5 and 3.4 nm respectively. Chronoamperometry in KCl (aq) 1.5 mM showed the expulsion of a hydrated ion from the slit and the compression of the equivalent of a layer of water molecules by ~ 0.12 nm when stepping the potential between $+200$ mV and -200 mV. When switching from -300 to $+300$ mV, a layer of water molecules (~ 0.25 nm)was initially expelled form the slit and then allowed back in after the surface charge had relaxed back to equilibrium, causing the surface to relax away from each other. In the 0.6 mM solution, the plot showed compression of the water molecules by ~ 0.15 nm when switching between $+200$ and -200 mV, and the expulsion of a layer of water molecules (~ 0.29 nm) when stepping the potential from -200 to $+200$ mV. The plot shows the expulsion as unfavourable and the relaxation that allows the water layer back in as favourable. These measurements speak to the exceptional resolution of the gold/mica setup. The chronocoulometry showed that the current decays with two characteristic timescales corresponding to the near-instantaneous electronic response and the movement of the ions within the liquid, confirming that the results in C_4C_1pyrr TFSI differ from the behaviour of a simple dilute salt solution.

Ch. 3 presents the triple gold mirror SFB (Au3 SFB), its preparation and

results obtained with it. It is a novel setup where both confining surfaces are potential-controlled and mica-free ultra-smooth gold, and three mirrors are used to obtain sub-nanometric resolution. The surfaces are obtained by templating the gold to single-crystal facets of mica and glueing these to template-stripped EPON epoxy glue, then stripping away the mica pieces. Contact-free calibration and the multi-matrix method are used to measure the separation between the surfaces. Ch. 6 presents force profiles that were measured under potential control with this setup, and these show that underscreening is independent from surface potential. A "hard wall" was observed at $\sim$ 5 nm, suggesting that capillary freezing may be occurring, as the critical separation is larger than in the gold/mica setup, in agreement with the hypothesis that critical separation increases with more metallic systems. There are two metal surfaces in Au3 SFB, and the "hard wall" is seen at about double the separation of the one in gold/mica SFB.

In conclusion, two electrochemical SFB setups were developed and used to make measurements that provide some new insights into the behaviour of concentrated electrolytes. These measurements show good agreement with other works from the field and demonstrate the potential of setups that harness high resolution and electrochemical methods.

Appendix A

Appendix A

A.1 Chapter 6: The Triple Gold Mirror Surface Force Balance

A.1.1 Contact-Free Calibration - The Multi-Matrix Method

Contact calibration in air cannot be used with two ultra-smooth metal surfaces, as they will weld and the mirrors will be destroyed in the process. A contact-free calibration was used in the triple gold mirror SFB (Au3 SFB). When using smooth metal as confining surfaces and as mirrors without mica spacers, the optical output of the interferometer is significantly complicated by the appearance of additional fringes. The methods detailed above no longer apply and a new one needs to be elaborated [112, 161].

The interferometric stack used in Au3 SFB includes $NBaLF-5 \mid Cr \mid Au1 \mid EPON \mid Au2 \mid medium \mid Au3 \mid EPON \mid NBaLF-5$. The EPON and NBaLF–5 are index-matched, and the dispersion of the EPON is negligible. The thickness of the Au layers are known, as the gold-coated mica used to template

Au2 and Au3 are kept and the step edges measured by AFM, so the thickness of the gold on each lenses can be measured. The thickness of Au1 was measured by coating a silica chip at the same time as the lenses, and the step edge measured by AFM. If we consider a classic SFB setup and its reflections, the thickness of the spacers $Z1$ and $Z2$, and the thickness of the medium can be determined numerically. This is achieved by creating a spectrum via the multi-matrix method and comparing the real interference spectrum of the stack to it. The calculated spectrum is obtained from the product of a matrix M, composed of the individual layers, which each have their own characteristic matrix M_i:

$$M = \prod_{i}^{N} M_i \tag{A.1}$$

With

$$\begin{bmatrix} \cos(q) & -\frac{i}{p}\sin(q) \\ -ip\sin(q) & \cos(q) \end{bmatrix} \tag{A.2}$$

Where q is defined as:

$$q = \frac{2\pi\tilde{n}z}{\lambda}\cos(\theta)$$

And p is:

$$p = \sqrt{\frac{\varepsilon}{\mu}}\cos(\theta)$$

In the above equations, $\tilde{n}$ is the complex refractive index, z is the thickness of the layer, λ is wavelength, θ is the angle between the beam entering the stack and the surface normal, ε is the dielectric constant and μ is the magnetic permeability. For crossed cylinders where $D << R$, $\theta = 0°$, and for non-magnetic materials, $p \approx \tilde{n}$. The transmission T through a stack with n layers is expressed as:

$$T = \frac{p_0}{p_{n+1}}\left|\frac{2p_0}{(m_{11}+m_{12}p_{n+1})p_0 + (m_{21}+m_{22}p_{n+1})}\right|^2 \tag{A.3}$$

In this, m_{jk} refers to the element of matrix M with the index j, k; p_0 and p_{n+1} are the values for the adjacent layers, which are semi-infinite. Thus the outer

bounds of the interferometric stack are considered semi-infinite such that $semi - infinite\ layer \mid layer\ 1 \mid layer\ 2 \mid layer\ n \mid ... \mid semi - infinite\ layer$.

Primary fringes ($S1$) arise from the distance-dependent interference between the mirrors, whereas secondary ($S2$) and tertiary ($S3$) fringes arise from the reflections between the mirrors and the interface of the medium and the spacer. In a symmetric setup like Au3 SFB, there is only one set of $S2$ as there is only one spacer. Tertiary fringes depend on the spacer thickness and are also distance dependent. Estimations for spacer thicknesses $Z1$ and $Z2$ can be obtained by analysing the secondary fringes, which increases the speed of the calculations.

Snell's law gives the fringe order based on relative intensity. The reflectivity of the spacer/medium interface is much lower than the mirror, so the fringe order is $I_P >> I_S > I_T$. Due to distance dependence, separation affects the division of the intensity of the interference pattern over the three types of reflection. When separation is small, the primaries dominate the FECO; when separation is large, the secondaries dominate and can be measured to estimate the thickness of the spacer(s). The multi-matrix method was used to analyse the output from Au3 SFB, as contact calibration could not be used.

A.1.2 Analysis

The analysis of Au3 SFB data is different to the one used for mica/mica or gold/mica SFB data. The analysis code was written in Python by Dr. Marco Balabajew and Dr. James Hallett, now both former post-doctoral researchers in the Oxford group, and small additional modifications were made by myself.

In practice, the method used to calibrate the FECO pattern and measure separation of the surfaces once the SFB is fully set up is as follows:

1. Mercury emission lines are recorded to obtain calibration images for the

exact wavelength per pixel position.

2. Secondary fringes are recorded at large separation ($>$1 μm) by moving the surfaces apart and capturing a long exposure image, which blurs the primary fringes (as they are distance dependent), but doesn't affect the position of the secondaries.

3. This image of the secondary fringes is fitted to equivalent calculated spectra. This gives estimated values for spacer thickness.

4. Primary fringes are recorded at moderate distance ($\sim$ 1 μm), and the values obtained in the fit of the secondary fringes are used to run a brute-force search to obtain a best-fit between the experimental P(D) and calculated spectra.

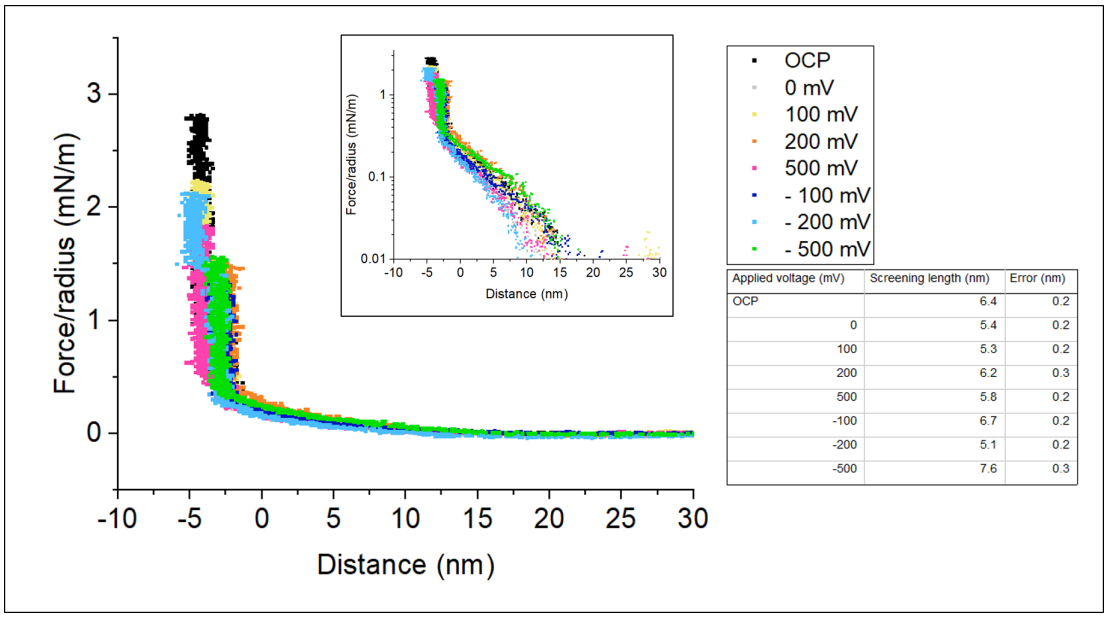
5. Data collected during this experiment can be analysed as D is calculated based on the calibration.

The exact thicknesses of the gold layers are crucially important important parameters, which have to be measured by AFM. The thickness of Au1 is measured by attaching a silicon chip with some Kapton tape covering part of its surface inside the chamber when coating the lenses in chromium and gold by PVD. Removing the tape creates a step edge, the height of which can be measured by AFM. Au2 and Au3 are measured by preserving the mica pieces templating the gold on the surfaces of each lens used in an experiment. As the mica piece is larger than the lens, when stripping it off a step edge is created at the boundary where the gold is glued to the surface of the lens. This step edge is then measured by AFM.

It should also be noted that the thickness of the EPON layer $Z1$ is extremely important as well. The fitting of the secondary fringes to calculated spectra only works if there are two secondaries in view. Interference patterns where

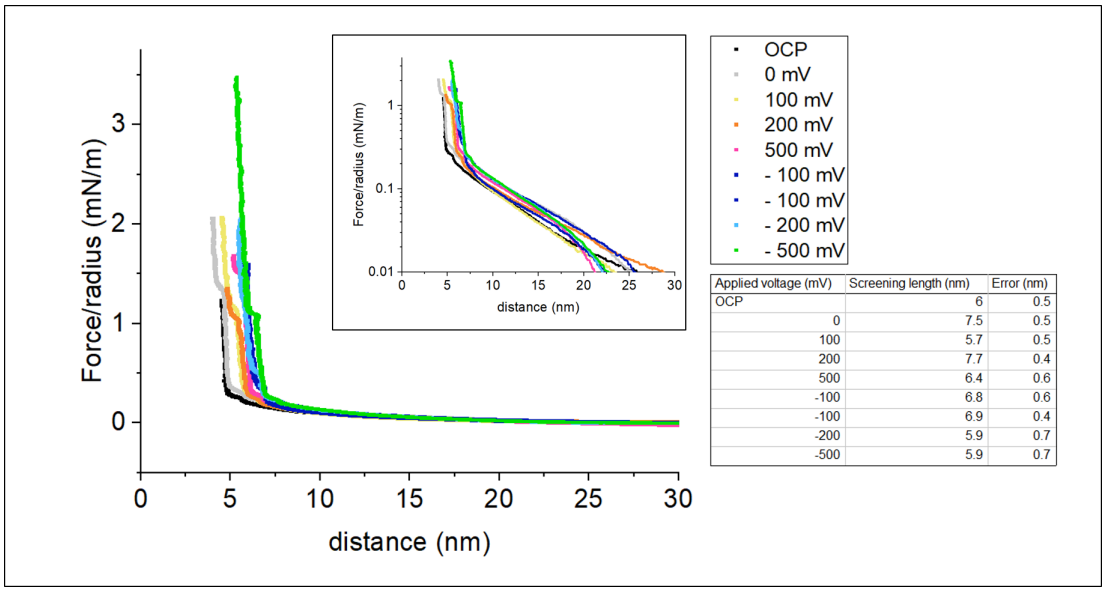
there are three secondaries (thicker glue) have proven to be impossible to fit using the multi-matrix method, so it is necessary for $Z1$ to be as thin as possible. This means that there is little room for error in the fabrication process.

A.2 Chapter 4: results from the Gold/Mica SFB Setup: Underscreening



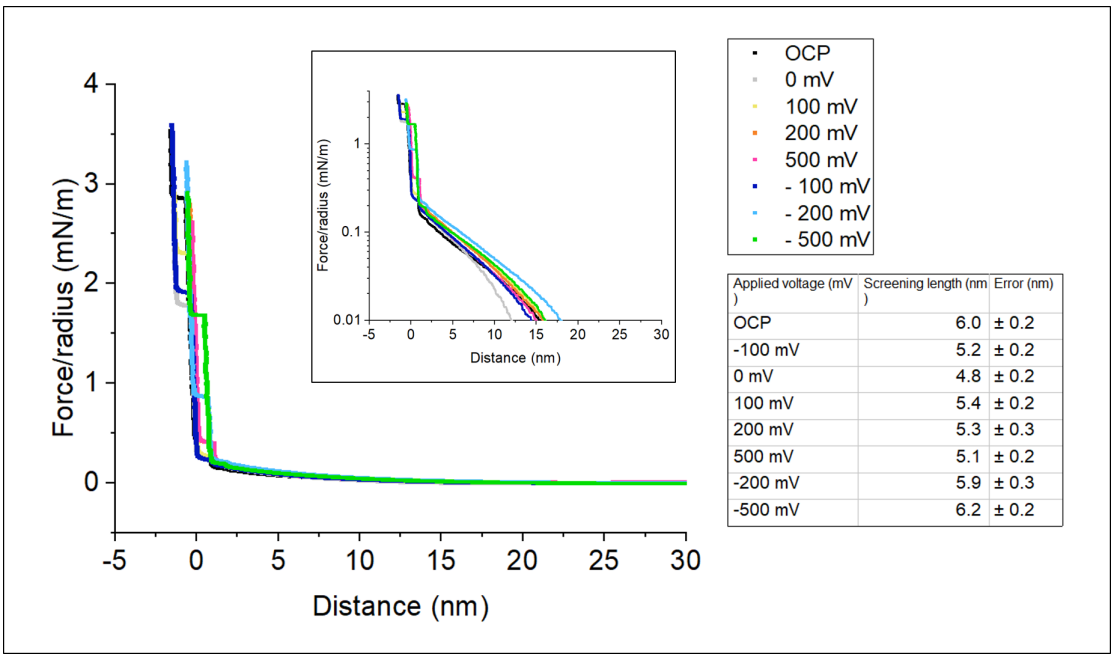
Applied voltage (mV)	Screening length (nm)	Error (nm)
OCP	6.4	0.2
0	5.4	0.2
100	5.3	0.2
200	6.2	0.3
500	5.8	0.2
-100	6.7	0.2
-200	5.1	0.2
-500	7.6	0.3

Figure A.1: *Force profiles in C_4C_1pyrr TFSI at a range of applied potentials.Distance values are not absolute. Layers are observed. Date of experiment 28/01/2021.*



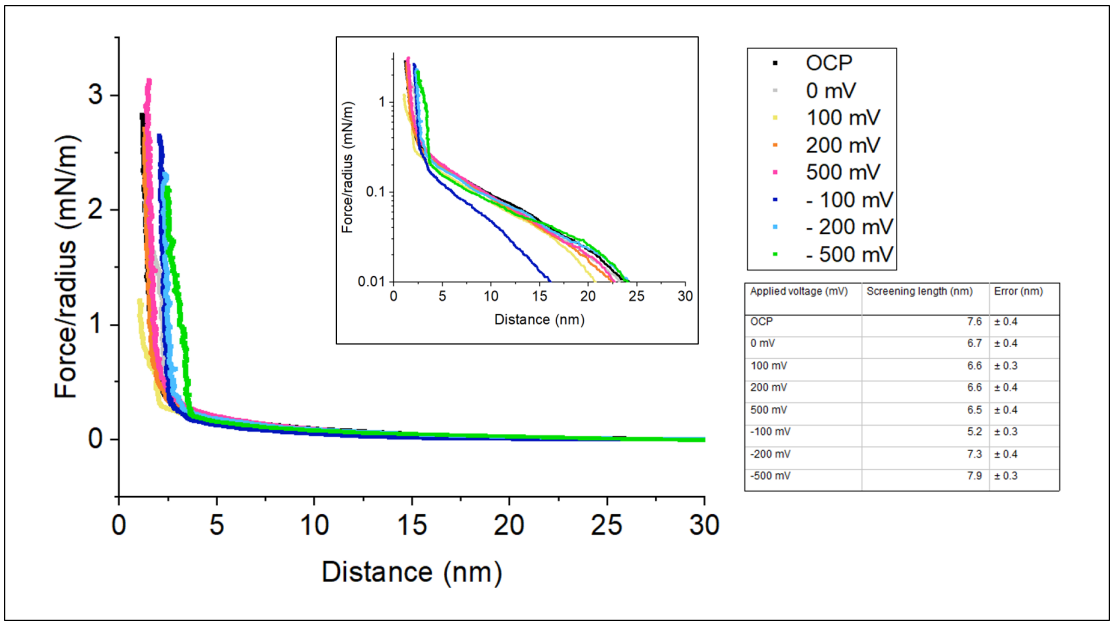
Applied voltage (mV)	Screening length (nm)	Error (nm)
OCP	6	0.5
0	7.5	0.5
100	5.7	0.5
200	7.7	0.4
500	6.4	0.6
-100	6.8	0.6
-100	6.9	0.4
-200	5.9	0.7
-500	5.9	0.7

Figure A.2: *Force profiles in C_4C_1pyrr TFSI at a range of applied potentials. Layers are observed. Date of experiment 03/02/2021.*



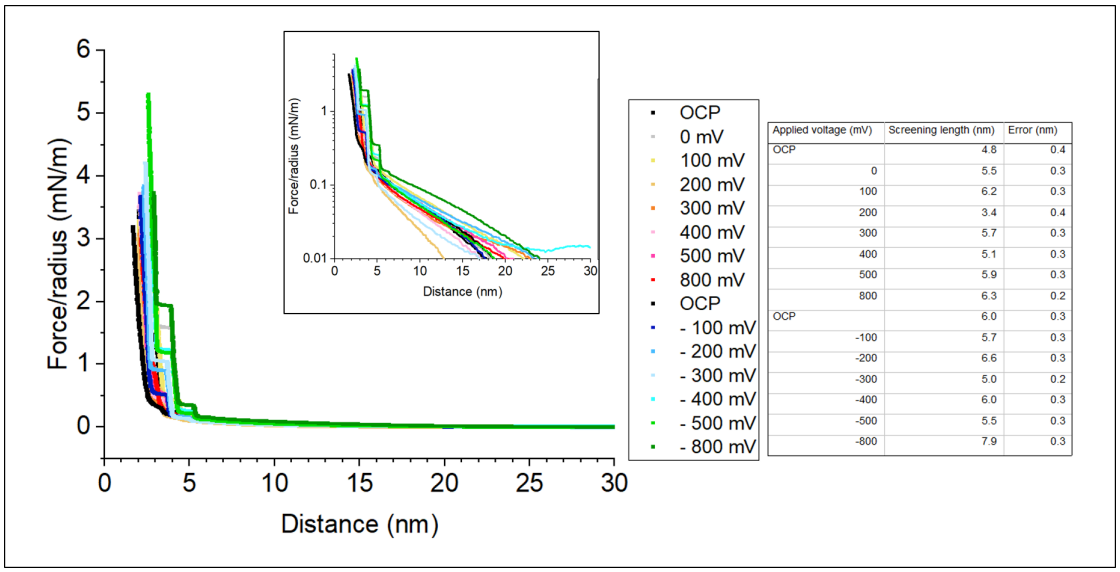
Applied voltage (mV)	Screening length (nm)	Error (nm)
OCP	6.0	± 0.2
-100 mV	5.2	± 0.2
0 mV	4.8	± 0.2
100 mV	5.4	± 0.2
200 mV	5.3	± 0.3
500 mV	5.1	± 0.2
-200 mV	5.9	± 0.3
-500 mV	6.2	± 0.2

Figure A.3: *Force profiles in C_4C_1pyrr TFSI at a range of applied potentials. Distances are not absolute. Layers are observed. Date of experiment 16/02/2021.*



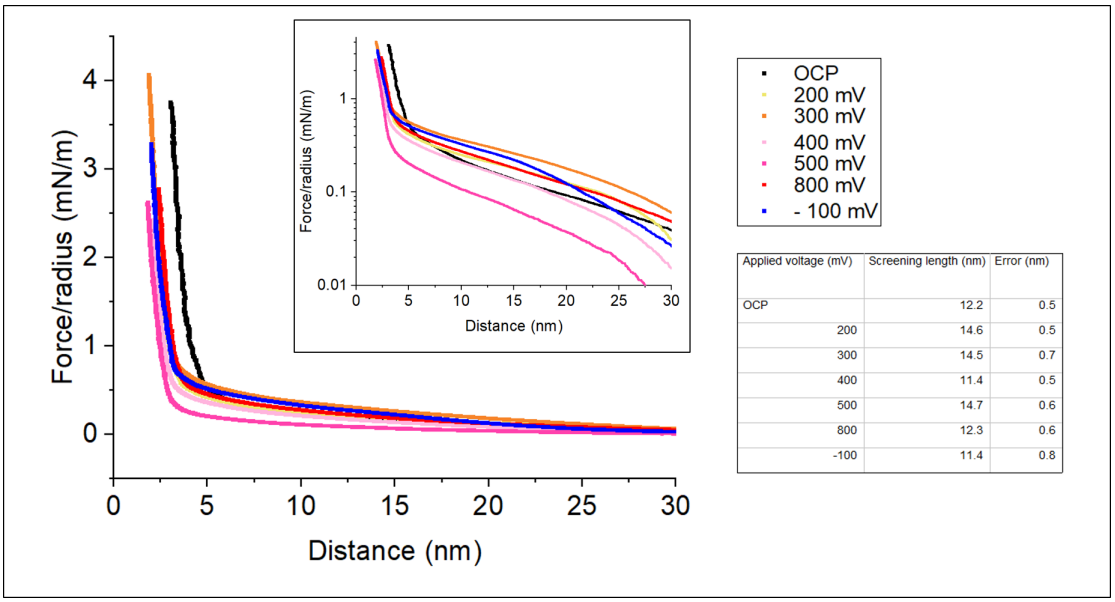
Applied voltage (mV)	Screening length (nm)	Error (nm)
OCP	7.6	± 0.4
0 mV	6.7	± 0.4
100 mV	6.6	± 0.3
200 mV	6.6	± 0.4
500 mV	6.5	± 0.4
-100 mV	5.2	± 0.3
-200 mV	7.3	± 0.4
-500 mV	7.9	± 0.3

Figure A.4: *Force profiles in C_4C_1pyrr TFSI at a range of applied potentials. No layers are observed. Date of experiment 24/03/2021.*



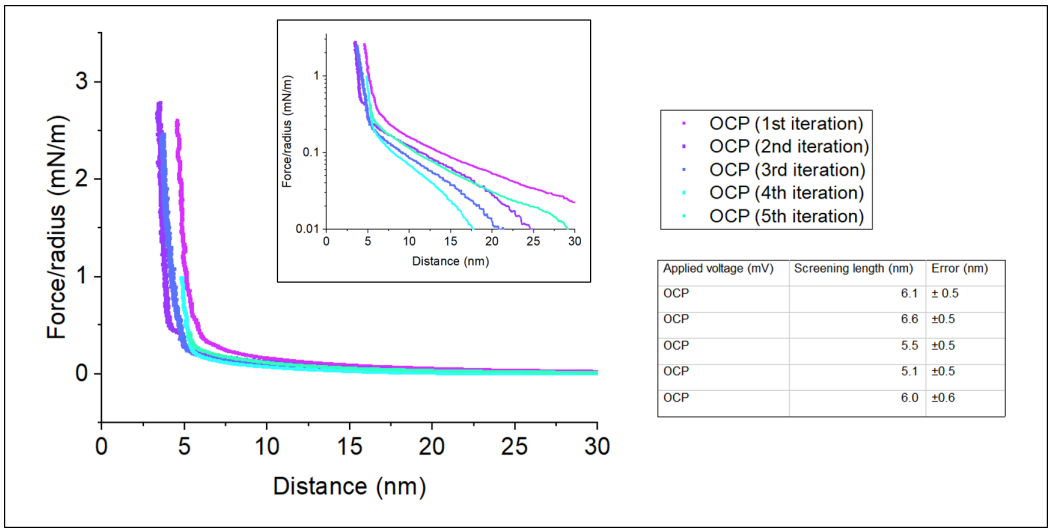
Applied voltage (mV)	Screening length (nm)	Error (nm)
OCP	4.8	0.4
0	5.5	0.3
100	6.2	0.3
200	3.4	0.4
300	5.7	0.3
400	5.1	0.3
500	5.9	0.3
800	6.3	0.2
OCP	6.0	0.3
-100	5.7	0.3
-200	6.6	0.3
-300	5.0	0.2
-400	6.0	0.3
-500	5.5	0.3
-800	7.9	0.3

Figure A.5: *Force profiles in C_4C_1pyrr TFSI at a range of applied potentials. Layers are observed. Date of experiment 23/06/2021.*



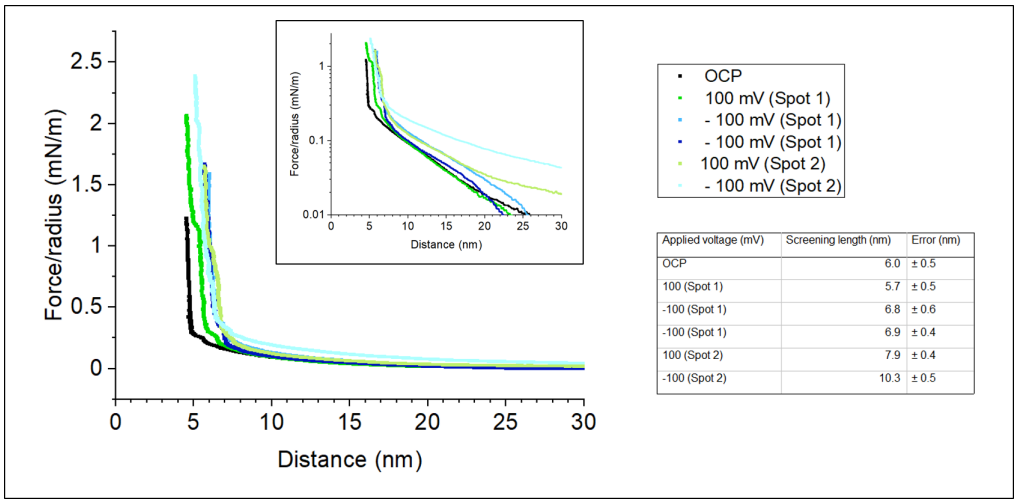
Applied voltage (mV)	Screening length (nm)	Error (nm)
OCP	12.2	0.5
200	14.6	0.5
300	14.5	0.7
400	11.4	0.5
500	14.7	0.6
800	12.3	0.6
-100	11.4	0.8

Figure A.6: *Force profiles in C_4C_1pyrr TFSI at a range of applied potentials. Layers are not observed. Date of experiment 30/08/2021.*



Applied voltage (mV)	Screening length (nm)	Error (nm)
OCP	6.1	± 0.5
OCP	6.6	±0.5
OCP	5.5	±0.5
OCP	5.1	±0.5
OCP	6.0	±0.6

Figure A.7: *Force profiles in C_4C_1pyrr TFSI at OCP, with multiple repeats. Layers are not observed. Date of experiment 27/10/2021.*



Applied voltage (mV)	Screening length (nm)	Error (nm)
OCP	6.0	± 0.5
100 (Spot 1)	5.7	± 0.5
-100 (Spot 1)	6.8	± 0.6
-100 (Spot 1)	6.9	± 0.4
100 (Spot 2)	7.9	± 0.4
-100 (Spot 2)	10.3	± 0.5

Figure A.8: *Force profiles in C_4C_1pyrr TFSI at 100 mV and -100 mV, with repeats. Layers are observed. Date of experiment 03/02/2021.*

Bibliography

[1] S. Perkin. “Ionic liquids in confined geometries”. *Physical Chemistry Chemical Physics* 14.15 (2012), 5052.

[2] Robert Hayes, Gregory G. Warr, and Rob Atkin. “At the interface: solvation and designing ionic liquids”. *Physical Chemistry Chemical Physics* 12.8 (2010), 1648.

[3] Jeannette Lindner et al. “Entropy Changes upon Double Layer Charging at a (111)-Textured Au Film in Pure 1-Butyl-1-Methylpyrrolidinium Bis[(trifluoromethyl)sulfonyl]ir Ionic Liquid”. *The Journal of Physical Chemistry C* 124.1 (Jan. 2020), 693–700.

[4] M. Armand et al. “Ionic-liquid materials for the electrochemical challenges of the future”. *Nature Materials* 8.8 (Aug. 2009), 621–629.

[5] C. Ye et al. “Room-temperature ionic liquids: A novel versatile lubricant”. *Chemical Communications* 21 (2001), 2244–2245.

[6] F. Zhou, Y. Liang, and W. Liu. “Ionic liquid lubricants: designed chemistry for engineering applications”. *Chemical Society Reviews* 38.9 (2009), 2590.

[7] Anthony Somers et al. “A Review of Ionic Liquid Lubricants”. *Lubricants* 1.1 (Jan. 2013), 3–21.

[8] Y. Bai et al. “High-performance dye-sensitized solar cells based on solvent-free electrolytes produced from eutectic melts”. *Nature materials* 7 (July 2008), 626–30.

[9] S. Perkin, T. Albrecht, and J. Klein. “Layering and shear properties of an ionic liquid, 1-ethyl-3-methylimidazolium ethylsulfate, confined to nano-films between mica surfaces”. *Phys. Chem. Chem. Phys.* 12.6 (2010), 1243–1247.

[10] J. N. Israelachvili. *Intermolecular and Surface Forces*. Elsevier, 2011.

[11] R. M Pashley. “DLVO and hydration forces between mica surfaces in Li+, Na+, K+, and Cs+ electrolyte solutions: A correlation of double-layer and hydration forces with surface cation exchange properties”. *Journal of Colloid and Interface Science* 83.2 (Oct. 1981), 531–546.

[12] J. N. Israelachvili and R. M. Pashley. “Measurement of the hydrophobic interaction between two hydrophobic surfaces in aqueous electrolyte solutions”. *Journal of Colloid and Interface Science* 98.2 (Apr. 1984), 500–514.

[13] T. Welton. “Room-Temperature Ionic Liquids. Solvents for Synthesis and Catalysis”. *Chemical Reviews* 99.8 (Aug. 1999), 2071–2084.

[14] C. S. Perez-Martinez and S. Perkin. “Interfacial Structure and Boundary Lubrication of a Dicationic Ionic Liquid”. *Langmuir* 35.48 (Dec. 2019), 15444–15450.

[15] R. Kjellander. “Decay behavior of screened electrostatic surface forces in ionic liquids: the vital role of non-local electrostatics”. *Phys. Chem. Chem. Phys* 18 (2016), 18985.

[16] F. Franks. *Water in Disperse Systems*. Springer New York, NY, 1975.

[17] C. Merlet et al. “Computer simulations of ionic liquids at electrochemical interfaces”. *Physical Chemistry Chemical Physics* 15.38 (Sept. 2013), 15781.

[18] C. Merlet et al. “The Electric Double Layer Has a Life of Its Own”. *The Journal of Physical Chemistry C* 118.32 (Aug. 2014), 18291–18298.

[19] S. W. Coles et al. “Correlation Length in Concentrated Electrolytes: Insights from All-Atom Molecular Dynamics Simulations”. *The Journal of Physical Chemistry B* 2020 (Feb. 2020), acs.jpcb.9b10542.

[20] A. Schlaich et al. “Electronic screening using a virtual Thomas-Fermi fluid for predicting wetting and phase transitions of ionic liquids at metal surfaces”. *Nature Materials* 21.2 (Feb. 2022), 237–245.

[21] Z. A. H. Goodwin and A. A. Kornyshev. “Underscreening, overscreening and double-layer capacitance”. *Electrochemistry Communications* 82.June (2017), 129–133.

[22] A. A. Lee et al. “Underscreening in concentrated electrolytes”. *Faraday Discussions* 199 (2017), 239–259.

[23] M. A. Gebbie et al. “Ionic liquids behave as dilute electrolyte solutions.” *Proceedings of the National Academy of Sciences of the United States of America* 110.24 (June 2013), 9674–9.

[24] M. A. Gebbie et al. “Long range electrostatic forces in ionic liquids”. *Chem. Commun.* 53.7 (2017), 1214–1224.

[25] A. M. Smith, A. A. Lee, and S. Perkin. “The Electrostatic Screening Length in Concentrated Electrolytes Increases with Concentration”. *The Journal of Physical Chemistry Letters* 7.12 (June 2016), 2157–2163.

[26] A. M. Smith, K. R. J. Lovelock, and S. Perkin. “Monolayer and bilayer structures in ionic liquids and their mixtures confined to nano-films”. *Faraday Discussions* 167 (2013), 279.

[27] S. W. Coles et al. “Interfacial structure and structural forces in mixtures of ionic liquid with a polar solvent”. *Faraday Discussions* 206 (2018), 427–442.

[28] M. J. Earle et al. “The distillation and volatility of ionic liquids”. *Nature* 439.7078 (Feb. 2006), 831–834.

[29] V. L. Martins and R. M. Torresi. “Ionic liquids in electrochemical energy storage”. *Current Opinion in Electrochemistry* 9 (June 2018), 26–32.

[30] A. Jarosik et al. “Conductivity of ionic liquids in mixtures”. *Journal of Molecular Liquids* 123.1 (Jan. 2006), 43–50.

[31] R. Newell et al. “A new high performance ionic liquid mixture electrolyte for large temperature range supercapacitor applications (–70 ° C to 80 ° C) operating at 3.5V cell voltage”. *Electrochimica Acta* 267 (Mar. 2018), 15–19.

[32] A. Eftekhari. “Supercapacitors utilising ionic liquids”. *Energy Storage Materials* 9 (Oct. 2017), 47–69.

[33] J. O. Valderrama and R. E. Rojas. “Critical properties of ionic liquids. Revisited”. *Industrial and Engineering Chemistry Research* 48.14 (July 2009), 6890–6900.

[34] V. Bhatt, K. Gohil, and A. Mishra. “Thermal Energy Storage Capacity of some Phase changing Materials and Ionic Liquids”. *International Journal of ChemTech Research* 2 (July 2010), 1771–1779.

[35] M. K. A. Ali et al. “A review of recent advances of ionic liquids as lubricants for tribological and thermal applications”. *Proceedings of the Institution of Mechanical Engineers, Part J: Journal of Engineering Tribology* (June 2022), 1–24.

[36] W. Liu et al. “Tribological Performance of Room-Temperature Ionic Liquids as Lubricant”. *Tribology Letters* 13.2 (Aug. 2002), 81–85.

[37] M. Palacio and B. Bhushan. “A Review of Ionic Liquids for Green Molecular Lubrication in Nanotechnology”. *Tribology Letters* 40 (Nov. 2010), 247–268.

[38] M. Mezger et al. “Molecular Layering of Fluorinated Ionic Liquids at a Charged Sapphire (0001) Surface”. *Science* 322.5900 (Oct. 2008), 424–428.

[39] D. Tabor and R. H. S. Winterton. “Surface forces: Direct measurement of normal and retarded van der waals forces”. *Nature* 219.5159 (1968), 1120–1121.

[40] J. N. Israelachvili. “Thin film studies using multiple-beam interferometry”. *Journal of Colloid And Interface Science* 44.2 (1973), 259–272.

[41] J. N. Israelachvili and G. E. Adams. “Measurement of Forces between Two Mica Surfaces in Aqueous Electrolyte Soutions in the Range 0-100 nm.” *J.Chem.Soc., Faraday Trans.I* 74 (1978), 975.

[42] J. N. Israelachvili et al. “Recent advances in the surface forces apparatus (SFA) technique”. *Reports on Progress in Physics* 73.3 (Mar. 2010), 036601.

[43] E. Kumacheva and J. Klein. “Simple liquids confined to molecularly thin layers. II. Shear and frictional behavior of solidified films”. *Journal of Chemical Physics* 108.16 (Apr. 1998), 7010–7022.

[44] R. G. Horn, D. F. Evans, and B. W. Ninham. “Double-layer and solvation forces measured in a molten salt and its mixtures with water”. *Journal of Physical Chemistry* 92.2 (1988), 3531–3537.

[45] C. D. van Engers et al. “A 3-mirror surface force balance for the investigation of fluids confined to nanoscale films between two ultra-smooth polarizable electrodes”. *Review of Scientific Instruments* 89.12 (Dec. 2018).

[46] H. Kawai et al. “New surface forces apparatus using two-beam interferometry”. *Review of Scientific Instruments* 79.4 (Apr. 2008), 043701.

[47] M. Kasuya and K. Kurihara. “Novel Surface Forces Apparatus for Characterizing Solid-Liquid Interfaces”. *Electrochemistry* 82.5 (2014), 317–321.

[48] J. N. Connor and R. G. Horn. “Measurement of Aqueous Film Thickness between Charged Mercury and Mica Surfaces: A Direct Experimental Probe of the Poisson-Boltzmann Distribution”. *Langmuir* 17.23 (Nov. 2001), 7194–7197.

[49] S. Fujii, M. Kasuya, and K. Kurihara. “Characterization of Platinum Electrode Surfaces by Electrochemical Surface Forces Measurement”. *The Journal of Physical Chemistry C* 121.47 (Nov. 2017), 26406–26413.

[50] J. M. Levins and T. K. Vanderlick. “Characterization of the Interface between a Rough Metal and Smooth Mica in Contact”. *Journal of Colloid and Iinterface Science* 185 (1997), 449–458.

[51] R. F. Knarr, R. A. Quon, and T. K. Vanderlick. “Direct Force Measurements at the Smooth Gold/Mica Interface”. *Langmuir* 14.22 (Oct. 1998), 6414–6418.

[52] M. Valtiner et al. “The electrochemical surface forces apparatus: The effect of surface roughness, electrostatic surface potentials, and anodic oxide growth on interaction forces, and friction between dissimilar surfaces in aqueous solutions”. *Langmuir* 28.36 (Sept. 2012), 13080–13093.

[53] B. Moeremans et al. “Lithium-ion battery electrolyte mobility at nano-confined graphene interfaces”. *Nature Communications* 7.1 (Nov. 2016), 12693.

[54] R. Tivony et al. “Direct Observation of Confinement-Induced Charge Inversion at a Metal Surface”. *Langmuir* 31.47 (Dec. 2015), 12845–12849.

[55] H. K. Christenson and N. H. Thomson. “The nature of the air-cleaved mica surface”. *Surface Science Reports* 71.2 (June 2016), 367–390.

[56] N. Kampf et al. “Direct Measurement of Sub-Debye-Length Attraction between Oppositely Charged Surfaces”. *Physical Review Letters* 103.11 (Sept. 2009), 118304.

[57] C. S. Perez-Martinez and S. Perkin. “Surface forces generated by the action of electric fields across liquid films”. *Soft Matter* 15.21 (2019), 4255–4265.

[58] R. Tivony and J. Klein. “Modifying surface forces through control of surface potentials”. *Faraday Discussions* 199 (2017), 261–277.

[59] P. Simon and Y. Gogotsi. “Materials for electrochemical capacitors”. *Nature Material* 7 (Nov. 2008), 845.

[60] L. Chai and J. Klein. “Large Area, Molecularly Smooth (0.2 nm rms) Gold Films for Surface Forces and Other Studies”. *Langmuir* 23.14 (July 2007), 7777–7783.

[61] M. Ruths et al. “Confinement-Induced Film Thickness Transitions in Liquid Crystals between Two Alkanethiol Monolayers on Gold”. *Langmuir* 17.20 (Oct. 2001), 6213–6219.

[62] J. M. Levins and T. K. Vanderlick. “Extended Spectral Analysis of Multiple Beam Interferometry: A Technique To Study Metallic Films in the Surface Forces Apparatus”. *Langmuir* 10.10 (1994), 2389–2394.

[63] Z. Zhang, S. Witham, and E. Alexov. “On the role of electrostatics in protein–protein interactions”. *Physical Biology* 8.3 (June 2011), 035001.

[64] B. Honig and A. Nicholls. “Classical Electrostatics in Biology and Chemistry”. *Science* 268.5214 (May 1995), 1144–1149.

[65] J. A. McCammon. “Darwinian biophysics: Electrostatics and evolution in the kinetics of molecular binding”. *Proceedings of the National Academy of Sciences* 106.19 (May 2009), 7683–7684.

[66] D. Guimarães, A. Cavaco-Paulo, and E. Nogueira. “Design of liposomes as drug delivery system for therapeutic applications”. *International Journal of Pharmaceutics* 601 (May 2021).

[67] de Jong. “Drug delivery and nanoparticles: Applications and hazards”. *International Journal of Nanomedicine* 3.2 (June 2008), 133.

[68] B. E. Conway. *Electrochemical Supercapacitors: scientific Fundamentals and Technological Applications*. Springer New York, NY, 1999.

[69] Z. Li et al. “Electrostatic layer-by-layer self-assembly multilayer films based on graphene and manganese dioxide sheets as novel electrode materials for supercapacitors”. *Journal of Materials Chemistry* 21.10 (2011), 3397.

[70] X. Li and C. Wang. “Engineering nanostructured anodes via electrostatic spray deposition for high performance lithium ion battery application”. *J. Mater. Chem. A* 1.2 (2013), 165–182.

[71] R. Tivony and J. Klein. “Probing the Surface Properties of Gold at Low Electrolyte Concentration”. *Langmuir* 32.29 (July 2016), 7346–7355.

[72] R. Tivony et al. “Charging dynamics of an individual nanopore”. *Nature Communications* 9.1 (Dec. 2018), 4203.

[73] S. Tsuzuki et al. “Magnitude and Directionality of Interaction in Ion Pairs of Ionic Liquids: Relationship with Ionic Conductivity”. *The Journal of Physical Chemistry B* 109.34 (Sept. 2005), 16474–16481.

[74] L. G. Gomella and S. A. Haist. *Clinician’s Pocket Reference: The Scut Monkey, 11e.* McGraw Hill, 2007.

[75] J. Jameson et al. *Harrison’s Manual of Medicine, 20e.* McGraw Hill, 2020.

[76] F. J. Millero. “Sea Water as an Electrolyte”. *Chemistry of Marine Water and Sediments*. Ed. by Antonio Gianguzza, Ezio Pelizzetti, and Silvio Sammartano. Berlin, Heidelberg: Springer Berlin Heidelberg, 2002, pp. 3–34.

[77] A. A. Kornyshev. “Double-Layer in Ionic Liquids: Paradigm Change?” *The Journal of Physical Chemistry B* 111.20 (May 2007), 5545–5557.

[78] Drew McCormack, Steven L. Carnie, and Derek Y.C. Chan. “Calculations of Electric Double–Layer Force and Interaction Free Energy between Dissimilar Surfaces”. *Journal of Colloid and Interface Science* 169.1 (Jan. 1995), 177–196.

[79] Barry W. Ninham and V.Adrian Parsegian. “Electrostatic potential between surfaces bearing ionizable groups in ionic equilibrium with physiologic saline solution”. *Journal of Theoretical Biology* 31.3 (June 1971), 405–428.

[80] Gregor Trefalt, Sven Holger Behrens, and Michal Borkovec. “Charge Regulation in the Electrical Double Layer: Ion Adsorption and Surface Interactions”. *Langmuir* 32.2 (Jan. 2016), 380–400.

[81] Alexis Grabbe. “Double layer interactions between silylated silica surfaces”. *Langmuir* 9.3 (Mar. 1993), 797–801.

[82] Cunlu Zhao et al. “Extracting local surface charges and charge regulation behavior from atomic force microscopy measurements at heterogeneous solid-electrolyte interfaces”. *Nanoscale* 7.39 (2015), 16298–16311.

[83] T Gisler et al. “Understanding colloidal charge renormalization from surface chemistry: Experiment and theory”. *The Journal of Chemical Physics* 101.11 (Dec. 1994), 9924–9936.

[84] Mark E. Fleharty, Frank van Swol, and Dimiter N. Petsev. “The effect of surface charge regulation on conductivity in fluidic nanochannels”. *Journal of Colloid and Interface Science* 416 (Feb. 2014), 105–111.

[85] Steven L. Carnie and Derek Y.C. Chan. “Interaction Free Energy between Plates with Charge Regulation: A Linearized Model”. *Journal of Colloid and Interface Science* 161.1 (Nov. 1993), 260–264.

[86] M. Z. Bazant, B. D. Storey, and A. A. Kornyshev. “Double Layer in Ionic Liquids: Overscreening versus Crowding”. *Physical Review Letters* 106.4 (Jan. 2011), 046102.

[87] M. V. Fedorov, N. Georgi, and A. A. Kornyshev. “Double layer in ionic liquids: The nature of the camel shape of capacitance”. *Electrochemistry Communications* 12.2 (Feb. 2010), 296–299.

[88] J. Fréchette and T. K. Vanderlick. “Double Layer Forces over Large Potential Ranges as Measured in an Electrochemical Surface Forces Apparatus”. *Langmuir* 17.24 (Nov. 2001), 7620–7627.

[89] J. N. Israelachvili. “Adhesion forces between surfaces in liquids and condensable vapours”. *Surface Science Reports* 14.3 (Feb. 1992), 109–159.

[90] Matthew A. Gebbie et al. “Long-range electrostatic screening in ionic liquids”. *Proceedings of the National Academy of Sciences* 112.24 (June 2015), 7432–7437.

[91] Hsiu-Wei Cheng et al. “Characterizing the Influence of Water on Charging and Layering at Electrified Ionic-Liquid/Solid Interfaces”. *Advanced Materials Interfaces* 2.12 (Aug. 2015), 1500159.

[92] R. M. Espinosa-Marzal et al. “Microslips to “Avalanches” in Confined, Molecular Layers of Ionic Liquids”. *The Journal of Physical Chemistry Letters* 5.1 (Jan. 2014), 179–184.

[93] C. N. Patra. “Structure of electric double layers: A simple weighted density functional approach”. *The Journal of Chemical Physics* 111.21 (Dec. 1999), 9832–9838.

[94] R. Kjellander. “The intimate relationship between the dielectric response and the decay of intermolecular correlations and surface forces in electrolytes”. *Soft Matter* 15 (2019), 5866.

[95] R. M. Lynden-Bell, A. I. Frolov, and M. V. Fedorov. “Electrode screening by ionic liquids”. *Physical Chemistry Chemical Physics* 14.8 (2012), 2693.

[96] R. Hayes et al. “Double Layer Structure of Ionic Liquids at the Au(111) Electrode Interface: An Atomic Force Microscopy Investigation”. *The Journal of Physical Chemistry C* 115.14 (Apr. 2011), 6855–6863.

[97] J. E. Hallett, H. J. Hayler, and S. Perkin. “Nanolubrication in deep eutectic solvents”. *Physical Chemistry Chemical Physics* 22.36 (2020), 20253–20264.

[98] R. Atkin et al. “An in situ STM/AFM and impedance spectroscopy study of the extremely pure 1-butyl-1-methylpyrrolidinium tris(pentafluoroethyl)trifluorophosphate/A interface: potential dependent solvation layers and the herringbone reconstruction”. *Physical Chemistry Chemical Physics* 13.15 (2011), 6849.

[99] A. A. Lee et al. “Casimir force in dense confined electrolytes”. *Molecular Physics* 116.21-22 (Nov. 2018), 3147–3153.

[100] M. V. Fedorov and A. A. Kornyshev. “Ionic Liquids at Electrified Interfaces”. *Chemical Reviews* 114.5 (Mar. 2014), 2978–3036.

[101] Benjamin Rotenberg, Olivier Bernard, and Jean-Pierre Hansen. “Underscreening in ionic liquids: a first principles analysis”. *Journal of Physics: Condensed Matter* 30.5 (Feb. 2018), 054005.

[102] Theodoros Baimpos et al. “Effect of Interfacial Ion Structuring on Range and Magnitude of Electric Double Layer, Hydration, and Adhesive Interactions between Mica Surfaces in 0.05–3 M Li + and Cs + Electrolyte Solutions”. 30.15 (Apr. 2014), 4322–4332.

[103] S. Perkin et al. “Is a Stern and diffuse layer model appropriate to ionic liquids at surfaces?” *Proceedings of the National Academy of Sciences* 110.44 (Oct. 2013).

[104] M. A. Gebbie et al. “Reply to Perkin et al.: Experimental observations demonstrate that ionic liquids form both bound (Stern) and diffuse electric double layers”. *Proceedings of the National Academy of Sciences* 110.44 (Oct. 2013).

[105] Markus Mezger et al. “Solid-liquid interfaces of ionic liquid solutions—Interfacial layering and bulk correlations”. *The Journal of Chemical Physics* 142.16 (Apr. 2015), 164707.

[106] W. Van Megen and I. Snook. “Solvent structure and solvation forces between solid bodies”. *Journal of the Chemical Society, Faraday Transactions 2: Molecular and Chemical Physics* 75 (1979), 1095–1102.

[107] R. G. Horn and J. N. Israelachvili. “Direct measurement of forces due to solvent structure”. *Chemical Physics Letters* 71.2 (Apr. 1980), 192–194.

[108] I. Bou-Malham and L. Bureau. “Nanoconfined ionic liquids: effect of surface charges on flow and molecular layering”. *Soft Matter* 6.17 (2010), 4062.

[109] R.J.F. Leote de Carvalho and R. Evans. “The decay of correlations in ionic fluids”. *Molecular Physics* 83.4 (Nov. 1994), 619–654.

[110] S. Tolansky. *Multiple-Beam Interferometry of Surfaces and Films*. Oxford University Press (Clarendon), 1949.

[111] S. Tolansky. *An Introduction to Interferometry*. Longmans Green & Co, 1955.

[112] M. T. Clarkson. “Multiple-beam interferometry with thin metal films and unsymmetrical systems”. *Journal of Physics D: Applied Physics* 22.4 (Apr. 1989), 475–482.

[113] S. C. Hunter and F. R. N. Nabarro. “XLVIII. The origin of Glauert’s superposition fringes”. *The London, Edinburgh, and Dublin Philosophical Magazine and Journal of Science* 43.340 (May 1952), 538–546.

[114] D. Y. C. Chan and R. G. Horn. “The drainage of thin liquid films between solid surfaces”. *The Journal of Chemical Physics* 83.10 (Nov. 1985), 5311–5324.

[115] Romain Lhermerout and Susan Perkin. “Nanoconfined ionic liquids: Disentangling electrostatic and viscous forces”. *Physical Review Fluids* 3.1 (Jan. 2018), 014201.

[116] R. Tivony, Y. Zhang, and J. Klein. “Modulating Interfacial Energy Dissipation via Potential-Controlled Ion Trapping”. *The Journal of Physical Chemistry C* (Feb. 2021), acs.jpcc.0c11264.

[117] N. Elgrishi et al. “A Practical Beginner’s Guide to Cyclic Voltammetry”. *Journal of Chemical Education* 95.2 (Feb. 2018), 197–206.

[118] A. J. Bard and L. R. Faulkner. *Electrochemical Methods: Fundamentals and Applications*. John Wiley & Sons, 2001.

[119] Y. Levin. “Electrostatic correlations: from Plasma to Biology”. *Reports on Progress in Physics* 64 (2002), 1577–1632.

[120] J. Britton et al. “A Graphene Surface Force Balance”. *Langmuir* 30.38 (Sept. 2014), 11485–11492.

[121] A. K. Mahapatro et al. “Gold surface with sub-nm roughness realized by evaporation on a molecular adhesion monolayer”. 88.15 (Apr. 2006), 151917.

[122] V. Wieser et al. “Novel in situ sensing surface forces apparatus for measuring gold versus gold, hydrophobic, and biophysical interactions”. *Journal of Vacuum Science & Technology A* 39.2 (Mar. 2021), 023201.

[123] E. Abbe. *Archiv Für Mikroskopische Anatomie. Vol. 9*. Berlin Heidelberg: Springer, 1873.

[124] P. Gaddam and W. Ducker. “Electrostatic Screening Length in Concentrated Salt Solutions”. *Langmuir* 35.17 (Apr. 2019), 5719–5727.

[125] A. Ciach and O. Patsahan. “Correct scaling of the correlation length from a theory for concentrated electrolytes”. *Journal of Physics: Condensed Matter* 33.37 (Sept. 2021), 37LT01.

[126] J. Zeman, S. Kondrat, and C. Holm. “Bulk ionic screening lengths from extremely large-scale molecular dynamics simulations”. *Chemical Communications* 56.100 (2020), 15635–15638.

[127] L. B. da Silva. “Structural and dynamical properties of water confined in carbon nanotubes”. *Journal of Nanostructure in Chemistry* 4.2 (June 2014), 104.

[128] Y. Huang et al. “Size, separation, structural order and mass density of molecules packing in water and ice”. *Scientific Reports* 3.1 (Dec. 2013), 3005.

[129] S. Perkin et al. “Self-assembly in the electrical double layer of ionic liquids”. *Chemical Communications* 47.23 (2011), 6572.

[130] Hans M. et al. “Effective pore size and radius of capture for K+ ions in K-channels”. *Scientific Reports* 6.1 (Apr. 2016), 19893.

[131] L. Degrève, S. M. Vechi, and C. Q. Junior. “The hydration structure of the Na+ and K+ ions and the selectivity of their ionic channels”. *Biochimica et Biophysica Acta (BBA) - Bioenergetics* 1274.3 (June 1996), 149–156.

[132] R. M. Espinosa-Marzal et al. “Hydrated-ion ordering in electrical double layers”. *Physical Chemistry Chemical Physics* 14.17 (2012), 6085.

[133] E. Clementi and R. Barsotti. “Study of the structure of molecular complexes. Coordination numbers for Li+, Na+, K+, F- and Cl- in water”. *Chemical Physics Letters* 59.1 (Nov. 1978), 21–25.

[134] K.-L. Yang, S. Yiacoumi, and C. Tsouris. “Monte Carlo simulations of electrical double-layer formation in nanopores”. *The Journal of Chemical Physics* 117.18 (Nov. 2002), 8499–8507.

[135] A. R. Neale et al. “Physical-Chemical Characterization of Binary Mixtures of 1-butyl-1-methylpyrrolidinium bis(trifluoromethyl)sulfonylimide and Aliphatic Nitrile Solvents as Potential Electrolytes for Electrochemical Energy Storage Applications”. *Journal of Chemical & Engineering Data* 62.1 (Jan. 2017), 376–390.

[136] J. Comtet et al. “Nanoscale capillary freezing of ionic liquids confined between metallic interfaces and the role of electronic screening”. *Nature Materials* 16.6 (June 2017), 634–639.

[137] P. J. Carvalho, C. M. S. S. Neves, and J. A. P. Coutinho. “Surface Tensions of Bis(trifluoromethylsulfonyl)imide Anion-Based Ionic Liquids”. *Journal of Chemical & Engineering Data* 55.9 (Sept. 2010), 3807–3812.

[138] Manuel Meusel et al. “Growth of Multilayers of Ionic Liquids on Au(111) Investigated by Atomic Force Microscopy in Ultrahigh Vacuum”. *Langmuir* 36.45 (Nov. 2020), 13670–13681.

[139] J. N. Gaur and G. M. Schmid. “Electrochemical behavior of gold in acidic chloride solutions”. *Journal of Electroanalytical Chemistry and Interfacial Electrochemistry* 24.2-3 (Feb. 1970), 279–286.

[140] A. C. Hillier, S. Kim, and A. J. Bard. “Measurement of Double-Layer Forces at the Electrode/Electrolyte Interface Using the Atomic Force Microscope: Potential and Anion Dependent Interactions”. *The Journal of Physical Chemistry* 100.48 (Jan. 1996), 18808–18817.

[141] H. S. Frank and P. T. Thompson. “Fluctuations and the Limit of Validity of the Debye-Hückel Theory”. *The Journal of Chemical Physics* 31.4 (Oct. 1959), 1086–1095.

[142] A. Paul, S. Muthukumar, and S. Prasad. “Electrochemical Visualization of Room Temperature Ionic Liquid for the Detection of Functionalized 1-phenylpyridine Analogue in Mixed Sample”. *Journal of The Electrochemical Society* 167.13 (Oct. 2020), 137507.

[143] V. E. Shubin and P. Kékicheff. “Electrical Double Layer Structure Revisited via a Surface Force Apparatus: Mica Interfaces in Lithium Nitrate Solutions”. *Journal of Colloid and Interface Science* 155.1 (Jan. 1993), 108–123.

[144] U. Raviv et al. “Fluidity of Water Confined Down to Subnanometer Films”. *Langmuir* 20.13 (June 2004), 5322–5332.

[145] Marek Kosmulski. “The pH dependent surface charging and points of zero charge. VIII. Update”. *Advances in Colloid and Interface Science* 275 (Jan. 2020), 102064.

[146] Rahul Prasanna Misra, Siddhartha Das, and Sushanta K Mitra. “Electric double layer force between charged surfaces: Effect of solvent polarization”. *The Journal of Chemical Physics* 138.11 (Mar. 2013), 114703.

[147] A. Hamelin. “Study of the (210) face of gold in aqueous solutions”. *Journal of Electroanalytical Chemistry and Interfacial Electrochemistry* 138.2 (Sept. 1982), 395–400.

[148] Z. Shi and J. Lipkowski. “Chloride adsorption at the Au(111) electrode surface”. *Journal of Electroanalytical Chemistry* 403.1-2 (Feb. 1996), 225–239.

[149] O. M. Magnussen et al. “X-ray diffraction studies of ordered chloride and bromide monolayers at the Au(111)-solution interface”. *Physical Review B* 51.8 (Feb. 1995), 5510–5513.

[150] D.A. Scherson and D.M. Kolb. “Voltammetric curves for Au(111) in acid media: A comparison with Pt(111) surfaces”. *Journal of Electroanalytical Chemistry and Interfacial Electrochemistry* 176.1-2 (Sept. 1984), 353–357.

[151] J. E. Hallett, K. J. Agg, and S. Perkin. “Zwitterionic osmolytes facilitate fine-tuning of interactions between charged surfaces” (). in preparation.

[152] V. Lockett et al. “Differential capacitance of the double layer at the electrode/ionic liquids interface”. *Physical Chemistry Chemical Physics* 12.39 (Sept. 2010), 12499.

[153] M. V. Fedorov and A. A. Kornyshev. “Towards understanding the structure and capacitance of electrical double layer in ionic liquids”. *Electrochimica Acta* 53.23 (Oct. 2008), 6835–6840.

[154] Y. Lauw et al. “Room-Temperature Ionic Liquids: Excluded Volume and Ion Polarizability Effects in the Electrical Double-Layer Structure and Capacitance”. *Physical Review Letters* 103.11 (Sept. 2009), 117801.

[155] S. Rivera-Rubero and S. Baldelli. “Surface Spectroscopy of Room-temperature Ionic Liquids on a Platinum Electrode: A Sum Frequency Generation Study”. *The Journal of Physical Chemistry B* 108.39 (Sept. 2004), 15133–15140.

[156] E. W. Castner and J. F. Wishart. “Spotlight on ionic liquids”. *The Journal of Chemical Physics* 132.12 (Mar. 2010), 120901.

[157] B. Roling, M. Drüschler, and B. Huber. “Slow and fast capacitive process taking place at the ionic liquid/electrode interface”. *Faraday Discuss.* 154 (2012), 303–311.

[158] Anna Rybinska-Fryca, Anita Sosnowska, and Tomasz Puzyn. “Prediction of dielectric constant of ionic liquids”. *Journal of Molecular Liquids* 260 (June 2018), 57–64.

[159] J. Klein and E. Kumacheva. “Simple liquids confined to molecularly thin layers. I. Confinement-induced liquid-to-solid phase transitions”. *The Journal of Chemical Physics* 108.16 (Apr. 1998), 6996–7009.

[160] J. J. Segura et al. “Adsorbed and near surface structure of ionic liquids at a solid interface”. *Physical Chemistry Chemical Physics* 15.9 (2013), 3320.

[161] M. Balabajew, C. D. van Engers, and S. Perkin. “Contact-free calibration of an asymmetric multi-layer interferometer for the surface force balance”. *Review of Scientific Instruments* 88.12 (Dec. 2017), 123903.